ADVANCEMENTS IN HIGH-Q DEVELOPMENT FOR NOVEL MEDIUM-VELOCITY 644 MHZ 5-CELL ELLIPTICAL SUPERCONDUCTING RF CAVITIES FOR CONTINUOUS-WAVE OPERATION IN HEAVY-ION LINACS

By

Kellen E. McGee

A DISSERTATION

Submitted to
Michigan State University
in partial fulfillment of the requirements
for the degree of

Physics—Doctor of Philosophy

2023

ABSTRACT

The Facility for Rare Isotope Beams is a world-leading center for experimental nuclear physics research, and relies on a first-in-kind superconducting RF driver linac to supply 400 kW beams of a uniquely large range of particles, from protons through the heaviest uranium ions. The FRIB400 project proposes to double the end energy of the current superconducting FRIB linac for the heaviest uranium ions from 200 MeV per nucleon (MeV/u) to 400 MeV/u, which equates to approximately 1 GeV for protons. The increased rare isotope production from higher-energy drive beams would deliver new and exciting capabilities to FRIB users, which include extending the facility's reach along the neutron drip-line, greatly increasing the facility's rare isotope yield, and significantly improving the precision of parameter measurements for the nuclear matter equation of state, which is a particularly timely complement to the recent advent of multi-messenger astronomy, and the study of neutron star mergers.

The unique set of design parameters defined by the 400 MeV/u (uranium) energy goal, the physical size, continuous-wave operation, and cryogenic capacity of the extant facilities at FRIB, requires development of a first-in-kind $\beta = v/c = 0.65$, 644 MHz 5-cell elliptical superconducting RF (SRF) cavity, with field-leading efficiency, measured by the cavity's intrinsic quality factor, Q_0. The field of SRF has recently experienced a very active period of development, which demonstrated the potential to raise the Q_0 of 1.3 GHz cavities by factors of two to three or more. In addition to uncovering fascinating new properties of the fundamental physics of superconducting RF phenomena, these improvements suggest substantial improvements could be made over the minimum Q_0 of the proposed FRIB400 upgrade SRF cavities, if these new techniques can be adapted to the $\beta = 0.65$, 644 MHz regime.

This work presents the first validation of the the novel $\beta = 0.65$, 644 MHz 5-cell elliptical superconducting RF cavity design, and the first results of both conventional and advanced RF surface preparation techniques. In particular, this work focuses on two recently-developed high-Q_0 recipes: N-doping, and furnace baking, setting the current world-record Q_0 for this type of resonant cavity at 3.8×10^{10} at the FRIB400 operating gradient of 17.5 MV/m. We also find evidence that these results may be further improved upon, and make the case for further RF surface preparation recipe optimization.

We then pair these high-power RF investigations with techniques borrowed from material science to try to better understand the ways in which specific properties of the niobium material, such as grain structure and superconducting flux pinning force, can be related to its superconducting RF performance. These experiments better elucidate the effects of high-temperature annealing on niobium samples, which suggest methods of further optimizing cavity flux expulsion and thus SRF performance.

This work is dedicated to the memory of Bryan W. Lynn, Ph.D.
May some small part one day aid those who plumb the depths of the Standard Model.

ACKNOWLEDGMENTS

Foremost, I owe a great debt of thanks to my primary advisor, Prof. Peter N. Ostroumov. No student could have asked for more in terms of programmatic support, the result of which has been success in one of the hardest avenues for either student or advisor to manage: a strong research topic and continuing support that enabled the work to progress rapidly and smoothly for the duration of the degree. Peter's deep technical knowledge of all components of accelerator systems, and sound project management style, set a standard I shall spend the rest of my career attempting to achieve.

Superconducting RF requires an intense degree of practical knowledge. I must thank Dr. Sang-hoon Kim for his infinite patience and dedication in teaching both the practical and theoretical aspects of being an SRF scientist. He is always on-hand to remind me there is a better, more scientific way to approach a question, as a physicist might, and I am much the better researcher for it. As I move forward, I strive to always be asking myself the sort of questions Sang-hoon would.

I must also thank my Fermilab advisors, Dr. Martina Martinello and Dr. Grigory Eremeev. While both had the challenge of working with a new student joining FNAL during the Covid years, both provided critical guidance and added new dimensions to the work described herein, which would not have existed otherwise. Martina and Grigory made the opportunity to conduct research across two different SRF laboratories an especially enriching experience, for which I am very grateful.

Superconducting RF is also an incredibly resource-intense discipline, relying on a veritable army of specialists to take a SRF cavity design from paper to the test dewar, and thence to the beamline. The RF cavity studied in this thesis is literally the work of dozens of people, from the original designers to the manufacturers, to everyone else who handled it between original

fabrication and testing. I am especially fortunate to have been supported by not one but two exemplary SRF departments throughout my studies: one at Michigan State University, and one at Fermi National Accelerator Laboratory in Batavia. In an attempt, doomed to failure, to name everyone who deserves it, I would like to acknowledge, from Michigan State University, Walter Hartung, for always insightful discussions, Andrei Ganshyn, for expert handling of the MSU/FRIB SRF Highbay's 9kW liquid helium plant, which we (possibly to his frustration) relentlessly depleted for dunk testing in search of Q, and Alex Taylor, for the unfailing engineering design and support. The rest of the MSU SRF group, including Ting Xu, Laura Popielarski, Kyle Elliott, Brian Barker, Ethan Metzgar, and many others, are no less deserving of recognition.

In memoriam: John Popielarski was an inescapable and buoyant presence in and around the MSU SRF department, and highbay. I always enjoyed working with him and deeply appreciated his genuinely skilled, yet down-to-earth, and pragmatic approach to leadership. Even in the difficult stages of testing FRIB baseline production cavities and cryomodules, I never once saw him lose his ability to approach problems with empathy and humor. I could have asked for nothing more in a supervising colleague, and he will be sorely missed. We are fortunate his spirit lives on through the may components of the FRIB linac he aided in the development of.

From the superconducting science and technology division at Fermilab National Laboratory, I would like to acknowledge Olexsander Melnychuk, and Alex Netepenko for their help and insight on the Fermilab vertical test stand, and Zuhawn Sung for extensive assistance preparing niobium samples for EBSD and PPMS studies. Again, the list of supporting scientists, engineers, and technicians enabling SRF research at FNAL grows large, but must at minimum include the master coordinator Damon Bice, as well as Fumio Furuta, Abe Diaz,

and Dave Burke, among others.

From Argonne National Laboratory, I would like to thank Mike Kelly, Tom Reid, and Ben Guilfoye for their collaboration electropolishing and high-pressure water-rinsing prototype cavities from both FNAL and MSU/FRIB.

On a personal note, I would like to thank the friends and peers whose camaraderie were integral to finishing this degree, and my parents, who have been perpetually supportive of my long educational career. I am not the sort of person to thank their cats in their acknowledgments, but if I were, I would be sure to mention Vera ("Kat"), and Pucko for their useful diversions. In addition, no acknowledgements section would be complete without mentioning the two individuals most responsible for starting me down the path towards a PhD in Physics, a path I spent a non-negligible fraction of my life swearing I would never travel: Dr. Bryan W. Lynn, and Prof. Glenn D. Starkman, of Case Western Reserve University.

A final note of thanks goes to Prof. Christopher Kennedy, of the University of Chicago's department of Linguistics, for an enlightening discussion regarding subjectivity in adjective ordering constraints in the noun phrase, "Medium-velocity 644 MHz 5-cell elliptical superconducting niobium RF cavity," which was essential to devising a proper title for this work.

TABLE OF CONTENTS

LIST OF SYMBOLS

T_c	Critical temperature (threshold of superconductivity)
Q_0	Intrinsic quality factor (generally, specific to the resonator)
β	Particle velocity as a fraction of the speed of light (v/c).
q	electric charge
$p/\bar{p}$	protons/antiprotons
e	electron
μ	muon
H^-	hydrogen anion
∇^2	laplacian operator
$\mathbf{H}/\mathbf{B}$	vector representation of the magnetic field in media/in vacuum
k	wave vector
ω	Angular frequency
$\psi(x, y)$	wave equation, cartesian coordinates
$\psi(\rho, \phi)$	wave equation, polar coordinates
J_m	m-th order Bessel function
E_{acc}	Accelerating gradient (MV/m)
$\mu_{(0)}$	Magnetic permeability (of free space)
$\epsilon_{(0)}$	Electric permittivity (of free space)
P_f	Forward RF power
P_r	Reflected RF power
P_t	Transmitted RF power
P_L	RF power deposited/absorbed on cavity walls
U	Stored energy
G	Geometry factor
R_s	Superconducting RF surface resistance
R_{sh}	Shunt resistance

Q_L	Loaded quality factor
Q_{e1}	Cavity input quality factor ('coupling')
Q_{e2}	Cavity pickup quality factor ('coupling')
$\beta_{1,2}$	Coupling constants
H_c	Superconducting critical magnetic field (type-I superconductors)
H_{c1}	Lower superconducting critical magnetic fields (type-II superconductors)
H_{c2}	Upper superconducting critical magnetic fields (type-II superconductors)
Φ_0	Unit of superconducting flux quantum
j_s	Superconducting current, supercurrent
n_n/n_s	Number density of normal/superconducting electrons
λ_L	London penetration depth
k_B	Boltzmann's constant
$\hbar$	Plank's constant
v_F	Fermi velocity
ξ_0	Superconducting coherence length
l	Electron mean free path
κ	Landau-Ginzburg parameter
β_G	Geometrical β
B_{pk}	Peak magnetic field value reached on the cavity surface
E_{pk}	Peak electric field value on the cavity surface
R_{BCS}	Temperature-dependent Matthis-Bardeen RF surface resistance, "BCS resistance"
R_0	Temperature-independent RF surface resistance, "residual resistance"
S	Cavity flux sensitivity

LIST OF ABBREVIATIONS

BCS	Bardeen, Cooper, and Schrieffer
FRIB	(the) Facility for Rare Isotope Beams, with the proposed 400 MeV/u of Uranium upgrade, FRIB400.
MSU	Michigan State University
NSCL	National Superconducting Cyclotron Laboratory
RF	Radio Frequency
SRF	Superconducting RF
CW	Continuous Wave
MeV/u	megaelectron volt per nucleon
GeV	gigaelectron volt
SM	Standard Model
TeV	teraelectron volt
LHC	Large hadron collider
CERN	Conseil européen pour la recherche nucléaire
BNL	Brookhaven National Laboratory
SLAC	Stanford Linear Accelerator Complex
RFQ	Radiofrequency quadrupole
FCC	Future Circular Collider
BSM	Beyond the Standard Model
MV/m	gradient, megavolts per meter
TESLA	TeV Energy Superconducting Linear Accelerator
CEBAF	Continuous Electron Beam Accelerator Facility
ILC	International Linear Accelerator
EFT	Effective Field Theories
CCF	Coupled Cyclotron Facility
EDM	Electric dipole moment

CP	charge-parity (violation)
DUNE	Deep underground neutrino experiment
PIP-II	Proton Improvement Plan-II (two)
LCLS	Linear coherent light source, where its upgrade is (LCLS-II) (two)
SNS	Spallation Neutron Source
ESS	European Spallation Source
linac	Lin(ear) ac(celerator)
VHEE	Very High Energy Electron (therapy)
PET	Positron Emission Tomography
ADS	Accelerator Driven System (of energy generation)
CAFe	Front-end demo linac (Chinese Academy of Sciences)
IMP	Institute of Modern Physics (China)
EM	Electromagnetic wave
PLL	Phase-locked loop
TFM	Two-fluid model
TTF	Transit-time factor
BCP	Buffered chemical polish
EP	Electropolishing
HFQS	High-field Q-slope
VTS	Vertical Test Stand
SIMS	Secondary-Ion Mass Spectrometry
EBSD	Electron Backscatter diffraction
PPMS	Physical property measurement system
HPR	High-pressure water rinsing
FE	Field-emission
MP	Multipacting

Chapter 1

Introduction

The subject of this thesis, the design and optimization of certain superconducting RF cavities, forces an unjustly myopic approach to the broad and diverse field of particle acceleration. Superconducting RF cavities are the primary accelerating structures of many machines–their 'engines,' if you will–but focusing so exclusively on them is tantamount to writing about the Pratt & Whitney F119 engine whilst failing to mention the airplane it is attached to. This introduction begins by attempting to offset this inevitable slant by spending some time on the current and future roles of accelerators in technology and society today, and then transitions to the specific accelerator applications that motivate the development of high-efficiency (i.e., high-Q_0) superconducting RF cavities optimized for particle speeds of $\beta = v/c = 0.6$, which this thesis takes as its primary focus.

1.1 Particle accelerators

At their most basic level, particle accelerators are machines that transform electrical energy, stored in electromagnetic fields, into the kinetic energy of the particles pushed along by these fields. These particles range in size from electrons and positrons, weighing only 0.51 MeV, to protons (938 MeV) to the heaviest uranium ions ($\tilde{2}$22,000 MeV). Though these are somewhat unintuitive units of mass, (via $E = mc^2$), it is hopefully apparent that the range from 0.51

of *anything* to 222,000 of *anything* is remarkably large. Each of these types of accelerated particles have different uses in research, or applied technology, at differing energy levels. The mode of generation of the electromagnetic accelerating fields, and thus the amount of energy that can be put into them, and the efficiency with which this energy can be transferred to the charged particles passing through the accelerator, has been a primary focus of accelerators' technological development for nearly a century [1].

Particle accelerators' main role, both historically and the public view, has been at the forefront of physics discoveries. This trajectory began the moment Ernst Rutherford realized the need for energetic particles to probe the nature of the atom in the early 1920s, and carried onwards to the present, when the great-great-great grandchildren of those first electrostatic accelerators (which operated at just 300-600 keV) became the superconducting behemoths they are today, the largest being capable of colliding particles at center-of-mass energies that enable production of the entire family of Standard Model (SM) elementary particles (1-13 TeV).

This progression famously culminated in 2012 with the observation of the Higgs boson at 126 GeV at CERN, the remaining *predicted* piece of the SM, making it the most complete and accurate theory of nature known to mankind (augmented with neutrino mixing). While the circular machines such as the Tevatron at Fermilab (accelerating protons to $\tilde{9}00$ GeV for a collision energy of $\tilde{1}.8$ TeV) and the Large Hadron Collider (LHC) at CERN (accelerating protons to $\tilde{6}.8$ TeV for a collision energy of $\tilde{1}3$ TeV) are the reigning queens of the energy scale, smaller circular accelerators such as the one at Brookhaven National Laboratory (BNL), as well as linear accelerators, such as the Stanford Linear Accelerator (SLAC), had their part to play as well, notably in the co-discovery of the J/Ψ meson, the top and bottom quarks (SLAC) and the K meson (BNL) among others.

However, this focus on the triumph of the last few decades begs the question of what's next for accelerator technology. Accelerators, and particle detectors, are arguably the most sophisticated and complex technological achievements of mankind to date, spinning off many useful technologies in the course of their development. However, as the energy thresholds of discovery move further and further out of reach of current technology, funding, while not necessarily being reduced, also becomes unequal to the hundred-km-scale circular colliders needed to get us a *fraction* of the way closer to the energy threshold that could promise 'new' physics.

In some views, the best hope for realizing these new frontiers on Earth lies in making dramatic advancements in the accelerating technologies, which would enable the accelerating structures of these machines to generate much stronger electromagnetic fields much more efficiently. In parallel, the development of more powerful, more efficient accelerator components is also key to transferring accelerator technology to much smaller scales, where smaller versions of these big machines have a wide range of medical and industrial uses in society today.

The earliest particle accelerators generated their EM fields in the simplest possible way: a voltage was applied between two surfaces, creating an electrostatic field (E) that would enable a force (F) to act on a particle of charge q via the vector product $\mathbf{F} = \mathbf{q} \times \mathbf{E}$. As techniques of beam acceleration matured, advances in high-power RF engineering emerging from WWII allowed for a fundamental shift in method of accelerating field generation, from electrostatic to microwave resonant cavities. Thus, for the most significant fraction of their later development, the primary accelerating components of particle accelerators have been resonant RF cavities.

While the operative details of resonating RF cavities will be discussed later, the key

concepts needed to understand the rest of this chapter are simple enough: resonating RF cavities can achieve very high EM field strengths without the need to support such field strengths continuously. The maximum strength of these fields is measured in terms of linear gradient (Megavolts of electric potential per meter of distance, MV/m). These RF fields are supported with a certain efficiency: a highly efficient resonant cavity wastes very little of the input RF power in the form of cavity surface heating the strength of field it is able to produce. Thus, in the language of resonant RF cavities, the aforementioned need for "strong field" and "high-efficiency" structures for the next generation of particle accelerators translates directly to the pursuit of "high-gradient'' and "high-Q_0" RF cavity development. Superconductivity provides a way for these structures to dramatically increase their Q_0 at higher gradients by many orders of magnitude, but does not change their key function as described.

1.2 "What's next?"

The answer to "What's next?" on the frontier of pure physics research is a little less straightforward now than it was in the years leading up to the completion of the Standard Model, which makes motivating the next generation of billion-dollar accelerators tricky, to say the least. Previously, particle accelerator development had been driven by the desire to find particles whose existence and properties were incidentally predicted within an otherwise well-proven theoretical framework, namely, Weinberg's Model of Leptons [2]. With the Higgs, the last piece of the Model of Leptons, in place, the research foci driving the primary thread of particle accelerator development must reorientate to some of the following:

1. Producing more Higgs particles (a so-called 'Higgs factory'), to further understand Higgs properties beyond merely its mass.

2. Continuing up the energy scale, looking for exotic particles and phenomena *not* predicted by the Standard Model.

3. Moving to the nuclear physics frontier, to understand more about how Standard Model particles assemble themselves into atomic nuclei.

4. Moving to the neutrino physics frontier, to better understand the properties of the three flavors of neutrino, and their mixing angles.

Each of these directions define new goals for new (or upgraded) accelerators. Since the first two of these are the direct continuation of particle accelerator physics heritage in high energy physics, we will touch on these machines briefly, before turning to the latter two, which serve as the primary motivation for the development of the sub-GHz high-Q_0 superconducting RF cavity that is the focus of this thesis.

1.2.1 Accelerators for High Energy Physics

The immediate next step for CERN's famed Large Hadron Collider (LHC) is the high-luminosity upgrade, which will greatly increase the data generation rate of the current LHC. From the prospective of Higgs physics, the high-luminosity LHC (HL-LHC) will increase the Higgs production rate nearly five fold, from 3 million to 15 million Higgs bosons per year. This development, which aims for completion in 2029, relies on a number of upgrades to the CERN accelerator complex, beginning with an upgrade to the linear accelerator injector, Linac4. This machine employs several types of resonating RF structures including a radio-frequency quadrupole (RFQ), a drift-tube linac, and so-called π-mode structures (PiMS) to accelerate H^- ions to the desired injection energy of 160 MeV for the rest of the CERN accelerating complex [3].

The high-luminosity machine is expected to fulfill its primary mission by approximately 2040. Beyond that, preliminary design studies have begun for the Future Circular Collider (FCC), to be hosted at CERN, which aims to increase collision energies from the current 13 TeV to 50-100 TeV [4]. The technologies proposed to achieve this aim are as yet varied, however all require superconducting RF accelerating structures to support proton-proton, electron-positron and lepton-hadron modes of the collider operation for future rings of 80-100 km in circumference (the current LHC being 27 km in circumference) [5]. Key aims of such a machine would be higher-precision understanding of the electroweak sector, the Higgs boson and its properties, and to expand the search for beyond-the-Standard-Model physics, including clues to the nature of dark matter, to higher energy thresholds [4]. As with all circular machines, their difficult scale (up to 100 km!) is dictated by the limitations of charged particles, which bleed energy via synchrotron radiation the more they are forced to bend on their trajectories, and the achievable strength of the magnetic field in the bending magnets used to steer the beams around their circular trajectories. For perspective, 8 T magnets are currently in use at LHC, the world-record is currently set at around 14 T, and the 100 km FCC calls for magnets operating in the 16 T range. While superconducting RF cavities (likely thin-film niobium-on-copper) are a critical technology for the upgrade, the coupled challenge facing the magnet technology means that while advancements in SRF can make strides in cutting FCC operational and cooling costs, better cavities will not necessarily deliver a higher-energy, or more compact, machine until the magnets exist that can control the beam [5].

One of the challenging aspects of the LHC is that it is a *hadron* collider: collisions between protons (p) and antiprotons ($\bar{p}$) are difficult to interpret because protons are not fundamental particles, and $p - \bar{p}$ collisions are in reality six-quark collisions, with a plethora of possible

secondary and tertiary interactions and byproducts for detector data-collection algorithms to sift through. It would be of enormous scientific and computational advantage were we able to collide fundamental particles. Two such particles, the electron (e^-) and the muon (μ^-) have attracted interest for this application, however the charge carried by both, and thus the limitations of synchrotron radiation when these particles' trajectories are bent in any way, drive focus back to linear acceleration methods.

Unlike circular machines, in which particles can be repeatedly kicked by cycling them through the same accelerating structure every turn around the ring, particles in linear accelerators are accelerated in a straight line, which allows them to evade synchrotron radiation losses, but, these particles only get one pass through the machine. Thus, where the majority of a circular machine is usually given over to the bending magnets, with just a few accelerating structures, the majority of linear machines consist of accelerating structures, which aim for the highest accelerating gradient in the shortest possible linear space. As a result, the accelerating structures are the main cost driver of linacs: the stronger electromagnetic fields they can generate, the shorter the machine can be. Additionally, the more efficient these resonators are–i.e, the higher their quality factor, Q_0 can be made to be–the less heat they dump into the cryogenic system, and thus the less it costs to maintain these structures at cryogenic temperatures, in the case of superconducting resonators.

Development for various types of muon colliders is a fascinating topic, particularly given that these machines must fight against the muon's finite lifetime of about two microseconds (μs). This is all the time available for the muon to be generated, accelerated, and collided. Fortunately, due to relativistic effects, those two μs pass more and more slowly in the stationary 'laboratory' frame of reference, but the challenge remains daunting. While there are excellent arguments to be made for the muon-collider as the next 'discovery' machine

in particle physics, taking the mantle from the LHC [6], it is the development work for a linear electron collider has mostly advanced the field of SRF in recent times, and thus, for the purposes of this thesis, we will leave the subject of muon colliders here, and focus instead on the subject of linear electron colliders.

1.2.2 The International Linear Collider

The International Linear Collider, (ILC) is a proposed design for two opposing linacs which accelerate electrons (e^-) and positrons (e^+), towards a central collision point, with a baseline center-of-mass collision energy of 500 GeV over a total length of 31 *kilometers*. This machine would complement the work of the LHC, and be much more sensitive to properties of the Higgs boson, such as spin or parity, that currently elude the LHC. The usual suite of beyond-the-Standard-Model (BSM) physics possibilities to either find, or rule out, are available to this machine as well, enabled by the higher-precision measurements of the ILC, and higher production rates of particles sensitive to potential BSM physics [7].

The scale of the proposed ILC is staggering. As a linac, the majority of the 31-km length of the machine would consist of the accelerating structures. Superconducting RF (SRF) resonators are the obvious choice for maximizing gradient and quality factor, but manufacturing, cooling, and operating dozens of kilometers of these resonators–approximately 16,000 of them in total–to meet the proposed energy scale of the ILC in anything even *resembling* an economically feasible manner places immense demands on the limits of SRF technology.

At the start of development for the ILC proposal in the early 1990s, the then state-of-the-art superconducting RF resonators could only routinely achieve gradients of around 5 MV/m, whereas the more feasible realizations of the ILC would need gradients closer to 25 MV/m. With an eye towards the SRF needs of ILC-like machines, the TESLA (TeV Energy

Superconducting Linear Accelerator) technology collaboration (TTC) was founded in 1990 with the aim of significantly developing superconducting RF technology to meet the needs of the ILC and other applications throughout accelerator science.

Over the thirty years of consistent multinational development in SRF inspired by the ILC, TTC members working on the 1.3 GHz TESLA-shaped resonators designed to accelerate high-velocity particles ($\beta = v/c = 1$) for the ILC have increased the resonators' average gradients dramatically from 5 MV/m to the original ILC specification of 25 MV/m, resulting in a nearly 20-fold reduction in cost per MeV compared to the Continuous Electron Beam Accelerator Facility (CEBAF) cavities of the early 90s [7]. More recent innovations have made even 35 MV/m an operational possibility, and records have been set as high as 50 MV/m in single-cell versions of TESLA resonators. TESLA-lead high-Q_0 efforts have also seen dramatic improvement over the years with significant cost implications. The highest-Q TESLA resonators even admit the possibility that cryogenic cooling capacity needs, the leading cost-driver of a resonator-cost-driven machine, could be cut in half for some machines [8].

Thus, for a machine that has yet to exist, or even find a government backer, (Japan was seen as the remaining contender to host the$8-15 Bn USD machine, but the Japanese Ministry of Education, Culture, Sports, Science and Technology recently recommended 'shelving' the question of what country should host the ILC and instead encourage further SRF technological development [9]), the mere prospect of the ILC has already profoundly influenced the field of SRF. The 1.3 GHz TESLA resonator shape has become the de facto testbed for high-gradient and high-Q_0 research and development, and such unity behind a single cavity shape and frequency has enabled broad study across laboratories of the fundamentals of superconducting RF phenomena, and how they relate to high-gradient and high-Q_0

resonator properties. Discoveries stemming from these investigations have advanced many other planned or recently-built machines relying on SRF technology, and, of particular relevance, resulted in the resonator processing and treatment methods that are employed this thesis.

As a result of the long shadow cast in the research literature by the ILC's 1.3 GHz TESLA cavity, a significant fraction of the work of this thesis will be to understand how resonator fabrication and processing techniques optimized for the benefit of 1.3 GHz TESLA resonators can be translated, with equal benefit, to different resonators operating at different frequencies. Research conducted with 1.3 GHz cavities will be referenced and used as guidance throughout the experimental design stages of this thesis, and in the interpretation of experimental results. The influence of the ILC thus pervades the field of SRF development for linear accelerators, and, even if the machine, at least as originally proposed, is never built, its design must still be acknowledged for the role it plays in the advancement state-of-the-art superconducting RF resonators.

1.2.3 Accelerators for Nuclear Physics

Accepting the Standard Model as the complete and accurate theory of particles and fundamental forces at the energy scales relevant to normal existence and matter, the next interesting question is how do these well-understood fundamental building blocks assemble themselves into nuclei. This is the purview of nuclear physics, where the aim of theorists is to employ effective field theories (EFTs) of hadrons in attempts to describe all experimental observations of nuclear physics, from the rules governing the number of protons and neutrons in stable nuclei, up to the dynamics of neutron star formation and merger. Compelling arguments have even been recently made that stable "liquid" drops of nuclear-dense matter

arising from a realization of $SU(2)_L \times SU(2)_R$ chiral perturbation theory [10] may function as Standard-Model derivable dark matter candidates [11] [10].

Since the majority of the actual nuclear physics in the universe happens in the hearts of stars or at the boundaries of colliding celestial bodies, direct experimental probes of the types of theories described above have been historically difficult. The only way to begin journeying down that path is to find ways to recreate the conditions that exist at the center of exploding stars in the laboratory setting. Michigan State University (MSU) took the lead in experimental nuclear physics in the early 1980s with the design, construction, and operation of the world's first superconducting cyclotron, establishing the National Superconducting Cyclotron Laboratory (NSCL) at the forefront of experimental nuclear physics research. That first cyclotron (the K-500) was later joined by the second (the K-1200), which were then later combined, all providing various types of particle beams used to generate dozens of never-before-measured rare isotopes. These unstable nuclei test the limits of the nuclear equation of state, and serve aims ranging from understanding the physical structure of various atomic nuclei up to understanding element formation in stars.

The next upgrade to the NSCL replaced their coupled cyclotron facility (CCF) with the field-leading Facility for Rare Isotope Beams' (FRIBs') driver linac. Awarded in 2008 and co-funded by the US Department of Energy ($750M) and Michigan State University ($212M), construction for the facility began in 2014 and first beam commissioning began in 2018. Operational status was achieved April 2022, with the first user experiments beginning May-June 2022. The new range of experiments enabled by this linac at MSU/FRIB ensure the facility will remain at the forefront of experimental nuclear physics for decades to come.

1.2.3.1 The Facility for Rare Isotope Beams

The FRIB linac is a high-power machine, with a baseline specification of providing a field-leading 400 kW of beam power on target. Where most linacs are specialized for a single species of particle, FRIB accelerates a range of ions from protons (at 600 MeV) all the way up to the heaviest uranium ions (200 MeV per nucleon (MeV/u)). This places high value on flexibility in the design of the machine's components, which is both unique and challenging, with interesting design ramifications. Due to the high-power requirement, FRIB is a first-in-kind continuous-wave (CW) machine, meaning the RF power sent to the accelerating resonators is always 'on.' Turning off the RF for portions the RF cycle helps reduce the heat deposition on the resonator walls, but this 'pulsed' mode also reduces overall achievable beam power. CW operation necessitates the use of very high-efficiency (high Q_0) resonators for the accelerating elements of the linac, making superconducting RF the only feasible option: the current linac consists of 324 superconducting RF half-wave and quarter-wave resonators housed in 46 cryomodules, divided among the three linear accelerating segments of the machine.

The FRIB400 Energy Upgrade (FRIB400) project proposes to double the energy of the current superconducting driver linac from 200 MeV per nucleon (MeV/u) to 400 MeV/u for the heaviest uranium ions, which equates to approximately 1 GeV for protons [12]. The scientific motivations for this upgrade are broad and particularly timely: notably, detection of the first gravitational waves, which ushered in the new era of multi-messenger astrophysics, defined a need for a much more refined understanding of the nuclear matter equation of state in order to more fully interpret this new data. Only the upgraded FRIB400 facility would be able to provide enough neutron-rich isotopes to begin to characterize these properties,

as well as further elucidate critical processes of nucleosynthesis that remain mysterious [13]. Rare heavy-ion collisions enabled by FRIB400 also provide the opportunity to improve understanding of nuclear forces, and will double the number of elements for which the FRIB facility can reach the neutron drip line (from 30 elements to 60) [13]. The upgraded facility will also be able to increase production of rare isotopes useful in designing and characterizing electric dipole moment (EDM) searches, which use isotopes with irregularly shaped nuclei such as Radium-225, to enhance their sensitivity to charge-parity (CP) or Time-reversal symmetry-violating processes. This is noteworthy for the rare opportunity it provides nuclear physics to contribute to pure fundamental physics research testing the Standard Model, which could, among other things, better illuminate the origin of the matter-antimatter asymmetry in the universe [14].

The FRIB400 upgrade, and the scientific possibilities it entails, serves as the primary motivation for the work in this thesis. The aims of the upgrade, and the limitations of the existing facilities at MSU, define unique and challenging parameters for designing a superconducting RF resonator to meet the FRIB400 upgrade target energy. As a CW machine operating in the sub-GHz range on particles traveling at speeds of $\beta = v/c = 0.65$, a new type of SRF resonator needs to be designed and processed to record Q_0. This thesis lays the groundwork for the proposed upgrade SRF resonators, exploring their high-Q_0 potential by applying novel RF surface treatments, and identifying ways in which these treatments can be further optimized in these resonators for high-Q_0 operation. The ultimate goal of this research focus is to validate the new cavity design and provide a proven, repeatable, cavity processing method that can achieve unprecedented Q_0 performance for the eventual FRIB400 project proposal.

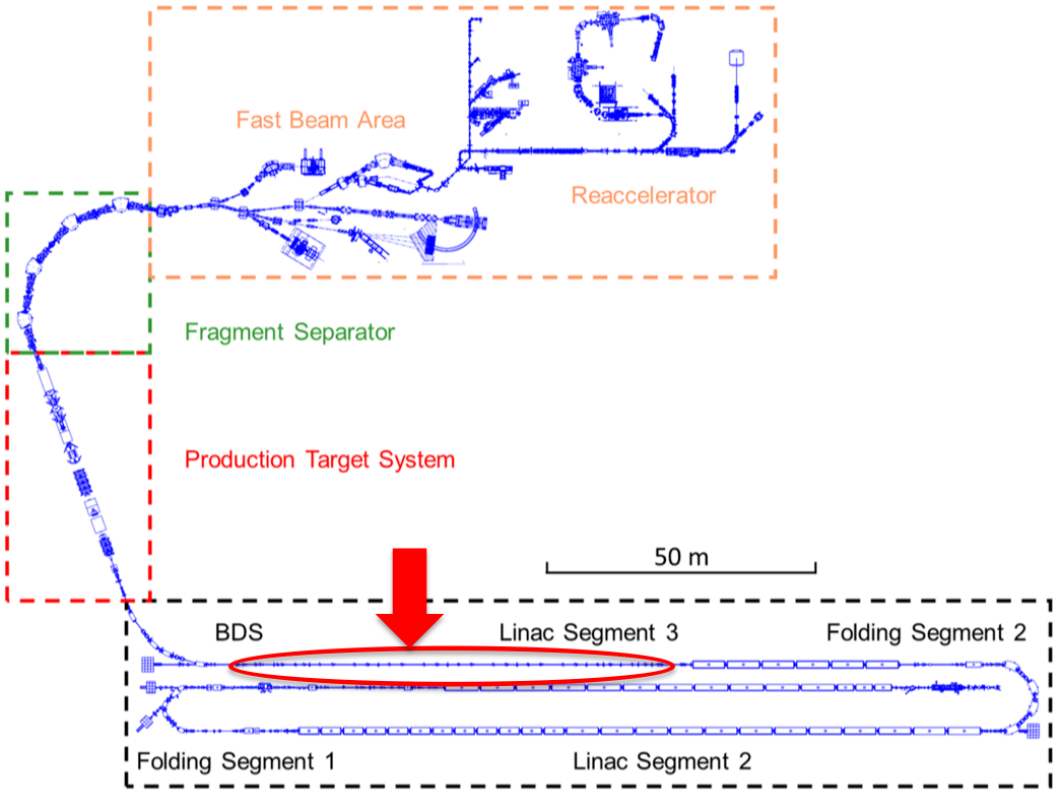

Figure 1.1: Drawing of the FRIB driver linac (black box), target halls (red box), fragment separator (green box), and experimental halls (orange box) FRIB400 5-cell cavity. The space available for the FRIB400 upgrade is indicated with the red oval and arrow.

1.2.4 Accelerators for Neutrino Physics

Since Fermilab's (FNAL's) Tevatron ceased operations in 2012, the laboratory has been undergoing a programmatic shift from the pursuit of high-energy physics towards fundamental neutrino physics. This is epitomized by the laboratory's investment in the Deep Underground Neutrino Experiment (DUNE), a long-baseline neutrino facility in which a high-intensity neutrino beam generated at the FNAL accelerator complex is shot over 13,000 km (800mi) to an array of underground liquid argon detectors (consisting of 40 kT of liquid argon in total) housed underground at Sanford Lab, in a former mine in Lead, South Dakota. This experiment aims to study fundamental questions in neutrino physics, such as resolving

the properties of neutrino oscillations, which could reveal reasons for the matter-antimatter asymmetery in the universe, or look for other hints to beyond the Standard Model Physics, via direct neutrino detection.

The DUNE project requires substantial upgrades to the FNAL accelerator complex. In particular, the linear injector accelerating the hydrogen anion (H^-) beam needed for this experiment must be upgraded. This new CW-compatible linac, dubbed the Proton-improvement-Plan II (PIP-II), which will accelerate H^- ions to 800 MeV [15], employs a sub-GHz high-Q_0 SRF resonator design that is highly similar to that needed by the FRIB400 project, and thus substantial synergy exists between the R&D efforts for both projects. As a result, a substantial amount of the work of this thesis was conducted in collaboration with FNAL and scientists working on developing the SRF resonators to be used in PIP-II.

1.3 Other accelerator uses in fundamental science

Besides their role in leading fundamental physics research and discovery, particle accelerators have found applications outside of physics as a utility enabling fundamental advances in biophysical and material sciences. A range of machines have been built or modified to provide reliable and high-intensity sources of x-rays and neutrons, which call for somewhat different optimizations of the accelerating elements than those required for high energy physics. Even so, the exchange of ideas in SRF development between the physics discovery machines and the applied technology and industry machines has contributed significantly to the advancement of the field.

1.3.1 Light sources and Spallation sources

While the synchrotron radiation emitted by charged particles as they accelerate, or travel curved trajectories, can be frustrating to physics machines, the generated x-rays are actually quite useful in other applications. Light–in the form of x-rays–is an important probe of the atomic scale, and the higher-energy those x-rays are, the smaller-scale the features that can be seen with them. Synchrotron light sources are fundamentally electron accelerators that force these particles around rings and through undulators, causing the electrons to emit as many photons as possible, which are then directed towards users' experiments.

Physicists and material scientists use the high-resolution synchrotron light to study topics such as the structure of matter, the evolution of surface phenomena (such as wear on airplane turbine blades [1], or even (somewhat recursively!) the evolution of surface structure on niobium cutouts from superconducting RF resonators for other machines [16]), or devise ways to optimize catalysts for industrial chemical applications. In biology, synchrotron sources enable crystallographers to produce atomic-scale resolution pictures of proteins and ligands, which has delivered nothing less than a revolution in structure-function study of proteins and enabled an entire new approach to drug design: protein function (or dysfunction) is intrinsically linked to the shape it assumes *in situ*, and crystallographic structures provided by synchrotron data has drastically improved our ability to understand proteins' shapes and their specific functions and interactions with each other, and engineer molecules (drugs) that can interact with these shapes in particular ways to either disrupt biological processes, or aid them [17]. Other uses for synchrotron light have been as broad as studying art and archaeological samples, and even in paleoanthropology, imaging the cranial features of a new species of 13-million year old hominoid, *Nyanzapithecus* [18].

The most advanced of these light sources, and the most closely related in SRF technology to the subject of this thesis, is the Linear Coherent Light Source (LCLS) at the Stanford Linear Accelerator Complex (SLAC). The LCLS is a billion times brighter, and, with a pulse repetition rate as fast as 1 MHz, allows for a 100,000-fold improvement over the current time resolution of storage ring-based light sources, allowing the machine to capture high-resolution images of the actual time evolution of fast processes such as chemical reactions, of either industrial or biological relevance.

The new upgrade to this machine, the Linear Coherent Light Source II (LCLS-II), adds a superconducting electron linac which uses 1.3 GHz SRF resonators, a direct offshoot of ILC development. These 1.3 GHz resonators for LCLS-II are the first instance of an industrial application of an advanced SRF surface treatment technique, nitrogen-doping (N-doping), delivering paradigm-shifting high-Q_0 performance (exceeding previous Q_0 records by two- to three-fold) [19]. As such, they serve as a strong proof-of-principle for the application of the technique to the SRF resonators studied in this thesis for the FRIB400 project.

In a similar vein, neutron spallation sources make use of a process by which high-intensity proton beams are accelerated to energies of only about 1 GeV at a heavy-metal target in order to produce showers of neutrons. These neutrons are then used, based on the particles' wave-like properties, to image molecules in a manner similar to the x-rays described above, except where x-rays scatter off of electron clouds, neutrons scatter off of the nuclei themselves, giving a better picture of, in particular, the distribution of light nuclei around the molecule under study [1]. Neutron images thus function as an important complement to x-ray images. The Spallation Neutron Source (SNS) at Oakridge National Laboratory (ONL), operating since 2007, and the European Spallation Source (ESS), under construction in Lund, Sweden, are significant to the work of this thesis because they both employ SRF resonators of a

similar size and frequency (sub-GHz) to those proposed for the FRIB400 project upgrade, though they are pulsed machines, and as such, have lower Q_0 requirements.

1.4 Other Linac Applications

Accelerators' relentless march through the years towards higher and higher energies searching for heavier and heavier particles somewhat diverted popular attention from the enduring uses found for these machines along the way. However, despite their esoteric beginnings, particle accelerators, particularly linear particle accelerators (linacs), now fulfill many critical roles in society today, in radiotherapy, nuclear medicine, and various industrial applications. While less directly related to the work of the thesis, these types of machines are briefly mentioned here as applications that could broadly stand to benefit from continued improvement of SRF resonator technology.

1.4.1 Medical linacs

The majority of the particle accelerators used in medical fields are linear accelerators (linacs), which accelerate electrons in a single pass through the accelerating elements of the machine. These electrons are either themselves used to bombard target cancerous tumors in patients, or are used to generate high-energy x-rays which are then directed at the treatment site, both aiming to induce double-strand breaks in the malignant DNA of the cancerous growth. Medical usage of linacs began in 1953 with the first patient irradiated at the London Hammersmith hospital (UK) with an 8 MeV purpose-built machine [20]. Advances in high-power RF engineering emerging from WWII allowed for a fundamental shift in methods of accelerating field generation, from electrostatic to microwave resonant cavities. This switch in

electromagnetic field generation technique allowed these machines to shrink from several stories tall to a few meters long, becoming much more practically handled in a hospital context [20].

Today, the medical linac is the most common method of delivering beam radiation treatments to cancer patients. Advances continue to be made in patient and beam manipulation to minimize radiation damage to healthy tissue and focus energy on the treatment area, in particular leading to the extremely effective 'gamma knife radiosurgery,' in which the high-intensity electron-generated x-ray beam is rotated around the patient, often eliminating the need for open surgery. The immediate future of linac development in radiotherapy treatment focuses on enabling use of the "Flash" effect, in which extremely high radiation doses are delivered in 0.5 sec or less [21]. The effects of Flash therapy on the tumor are similar to conventional therapies, but spare a much higher fraction of the healthy tissue around the treatment site. The technological challenge of FLASH and other proposed high-energy techniques such as Very High Energy Electron (VHEE) therapy to medical linac technology how to deliver a high enough dose rate at high enough energies to make treatment of anything other than shallow tumors feasible [22]. The energy and intensity requirements needed to fully realize these techniques begin to enter the purview of actual physics research-grade electron accelerators, which are realistic in cortexes on the magnitude of CERN (i.e., the CLEAR electron linac, which can deliver up to 220 MeV but takes 20 m to do it), but are not practical to transfer to the medical context with current acceleration technology.

The second critical medical application for linacs is in medical isotope generation. Historically, nuclear reactors were the main source of isotopes for use in diagnostic methods (e.g., positron emission tomography, or PET) or radiopharmaceuticals. Compact medical cyclotrons, which operate at a fixed energy, can produce a more limited range of isotopes and

are employed at many hospitals. However, with the decreasing population of operating nuclear reactors in North America, supply of even the most medically relevant of these, such as molybdenum-90 and xenon-133, has become increasingly limited. To circumvent legal issues with nuclear isotope importation, a number of US companies have begun exploring means by which these can be produced in sub-critical contexts domestically, some of which employ small linear accelerators. Niowave, for example, is a company spun off of Michigan State University's Facility for Rare Isotope Beams (FRIB) in 2005, who uses a compact 1 m long superconducting electron linac to bombard uranium with an electron beam, prompting it to undergo fission and produce a wide range of valuable isotopes [23]. These are then shipped to hospitals nationwide as either radiophamacuticals or other isotopes used for cancer therapy.

1.4.2 Energy generation

Highly-efficient linear accelerators may one day play a role in meeting energy needs of tomorrow's world. Nuclear fission remains the highest energy yield processes applied to steam generation, however concerns about the safety and security of nuclear reactor power plants, and concerns about long-term spent fuel handling, have long dogged this otherwise attractive energy source. Linear accelerators have been proposed as a method for ameliorating both of these issues: if a particle beam from a linac is used drive nuclear fission in a self-unsustaining reactor core, turning off the machine stops the reaction. The linac can also be used to deactivate nuclear waste, accelerating the decay of long-lived isotopes that reduces waste storage needs from hundreds of thousands of years to a few hundred.

A few groups worldwide are pursuing the possibility of an accelerator driven system (ADS) a 'closed' nuclear fuel cycle, which combines a fission-driving linac with a waste recycling system such that spent fuel can be reformed into new fuel which is then reused in the

accelerator-driven reactor. A 25 MeV superconducting RF proton linac (CAFe) has been completed at the Institute of Modern Physics (IMP) in China, with the intent of demonstrating the 'front end' of such an accelerator-driven system, and studies of the proposed nuclear fuel recycling methods are ongoing, with promising early results [24]. A concurrent ADS project, the Multi-purpose hYbrid Research Reactor for High-tech Applications (MYRRHA) is underway in Europe [25]. Ultimately, should any of these ideas be realized as components of future low-carbon energy generation for the future, advanced superconducting RF resonators will have had a central role in making it possible.

1.4.3 Industrial applications

Superconductiing RF resonators are still generally too costly and energy-intense devices to be practically used in industry. Small, normal-conducting electron linacs meet current needs for applications in cargo scanning, food or water sterilization, and other uses. Direct applications of accelerators in the manufacturing industry are generally related to using electron beams to drive polymer cross-linking reactions faster (or more thoroughly). When applied to materials such as industrial plastics, electron beam-driven cross-linking can change the physical properties of the material to make it (for example) less temperature-sensitive, more impact resistant, or less chemically reactive. Many ubiquitous materials such as polyethylene, EVA, and PVC respond well to electron-beam treatment and have been broadly used by parts manufacturers for decades.

1.5 Goals of thesis

The overarching goal of this thesis is to further our understanding of the advantages and limitations of high-Q_0 RF treatments developed in 1.3 GHz TESLA cavities for sub-GHz cavities intended for continuous-wave applications. This effort is driven by the need to provide a solid experimental foundation for the novel $\beta = 0.6$ 644-650 MHz 5-cell elliptical superconducting RF cavities designed for continuous-wave use in Michigan State University's FRIB400 upgrade linac segment, and in the penultimate stage of Fermilab's PIP-II linac. The MSU/FRIB project stands at the forefront of nuclear physics, and the PIP-II project is the next major advance in direct-detection neutrino physics: the novel SRF technology investigated by this thesis therefore stand to advance both fundamental nuclear physics and neutrino physics.

Unlike more mature superconducting RF cavity designs such as the $\beta = 1$ 1.3 GHz TESLA used in many high-energy applications, whose primary interest after decades of development is exploring cavity preparation methods whereby gradient and quality-factor can be pushed to new limits, these $\beta = 0.6$ sub-GHz cavities have to first establish basic aspects of their functionality. The specific goals of this thesis are thus as follows:

1. To demonstrate the mechanical viability of the novel medium-β 644 MHz 5-cell elliptical superconducting cavity design.

2. To demonstrate the RF viability by achieving reasonable gradient and quality factor results with standard RF surface treatments.

3. To motivate a high-Q_0 development program in sub-GHz cavities.

4. To initiate a high-Q_0 development program with the first applications of advanced techniques to medium-β 644 MHz 5-cell elliptical cavities.

5. To investigate the frequency-dependent effects of these advanced techniques (N-doping and furnace baking).

6. To identify parameters in the cavity treatment process with good potential to improve Q_0 after further optimization and systematic study

For clarity: Fermilab calls their $\beta = 0.6$ 650 MHz cavities 'low'-β, based on implicit comparison to their *other* 650 MHz cavities, which operate at $\beta = 1$, and FRIB calls their $\beta = 0.6$ 650 MHz cavities 'medium'-β, based on implicit comparison to the other cavities in the FRIB facility, which operate with 'low'-βs ranging from 0.41 to 0.53. The speed of light c provides a helpful witness example, making 'high' unquestionably $\beta = 1$, (the practical difference between e.g., the Tevatron's $\beta = 0.99999954$ cavities and CERN's $\beta = 0.999999991$ cavities being negligible), but 'medium' and 'low' both wind up used for $\beta = 0.6$. This linguistic dilemma serves as an example of the way vagueness can arise in meaning when using gradable adjectives to make implicit vs comparisons, as discussed in [26], to which the reader is directed for a fuller analysis. In an effort to dispel such vagueness for the purposes of this thesis, 'high,' shall henceforth refer to cavities operating at $\beta = v/c = 0.9$ and upwards, 'medium' shall refer to the $\beta = 0.6$ range, and 'low' will refer βs of 0.2 or less.

1.6 Organization of thesis

While the prospect of the FRIB400 upgrade and current PIP-II project necessitates technical interest in medium-velocity 644-650 MHz cavities, this thesis applies that technical interest

as the organizing principle of a broader exploration of the physics of superconducting RF cavities. Chapter 2 begins by introducing the physics of electrically resonant structures, and their usage in particle accelerators to transfer energy to charged particle beams. Once resonant RF cavities found their home as the primary accelerating components of particle accelerators, the next evolution of the technology was to explore ways to make the resonant cavities less electrically lossy. 'Just make it superconducting' is, of course, the aspirationally perfect low-loss solution, but, as Chapter 3 addresses, the application of strong, quickly oscillating RF fields to superconducting materials evokes new and interesting physical effects that one must contend with while designing and optimizing superconducting RF cavities. While a fully descriptive theory of all observed properties of superconducting RF cavities relevant to this work remains elusive, Chapter 3 begins with basic mathematical descriptions of superconductivity, with the aim of building some intuition for the superconducting properties these RF cavities aim to exploit. From there, Chapter 3 moves to a more detailed treatment of superconductivity in the presence of applied RF fields, with particular attention paid to the mechanisms leading to temperature-dependent and temperature-independent RF surface resistance. Chapter 3 then concludes with the principles of superconducting RF cavity fabrication and testing, with significant focus on the 'vertical' testing methods upon which the majority of the experimental work of this thesis relies.

The experimental portion of this work begins with Chapter 4, which comprises the preliminary design and validation of the prototype FRIB400 medium-velocity 644 MHz superconducting RF cavity, including the first-ever trials of standard RF surface preparation techniques in this novel velocity and frequency range. Chapter 5 builds on these results by applying the recently-developed, advanced RF surface processing techniques, nitrogen-doping and furnace baking, to the FRIB400 prototype cavities, and finds significant potential

for these treatments to enhance these cavities' performance by upwards of a factor of two. Chapter 6 changes course significantly to more fundamental superconducting RF studies enabled by single-cell versions of the 5-cell FRIB400 prototype cavities. These include direct measurements of flux sensitivity, as well as measurements of the change in the cavity's frequency as a function of temperature. Chapter 6 pairs these cavity-based measurements with bulk niobium material studies and concludes that some intrinsic measurable properties of the niobium material can be correlated with the RF performance of cavities fabricated from that material. Chapter 7 concludes this work with an overview of findings and provides an outlook for future work.

Chapter 2

Resonant structures for particle acceleration

Electrostatic accelerators use various methods to build up negative and positive electrical charge on different surfaces, and are generally limited by their size and the amount of charge that can be stored on a given surface before electrical breakdown occurs. Early on in the development of accelerators resonant cavities were thought of as possible means of generating very high fields, however the idea had to wait for developments in high-power RF engineering spurred in part by WWII to be realized. Unlike electrostatic fields, which always point in one direction, the RF fields used in accelerators' resonant structures cycle direction constantly, at rates on the order of MHz to GHz. Thus the particle bunches traveling through the accelerator must be precisely timed to hit the accelerating field during the new nanoseconds in which it is pointing forwards. While this is a mundane fact of accelerator operation today, getting machines the size of buildings to handle particles moving at significant fractions of the speed of light with precision on the order of less than a nanosecond is a technical feat well worth acknowledging. The fields of beam physics, accelerator design, beam instrumentation, and more are fascinating, and are filled with many other such technical accomplishments, but lay beyond the scope of this thesis.

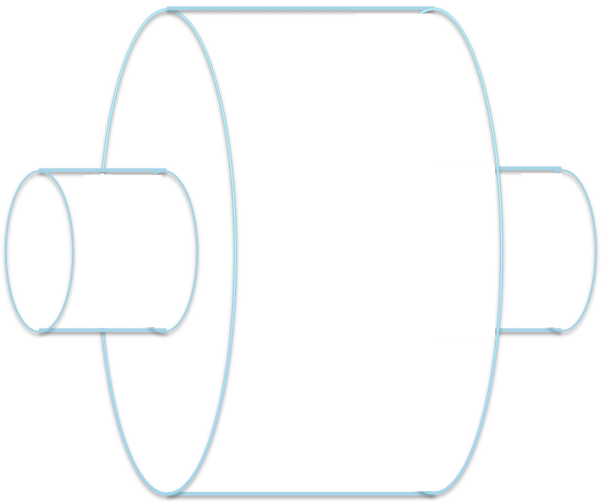

Figure 2.1: Diagram of the classic 'pillbox' cavity.

2.1 Resonant cavity fundamentals and measurement techniques

An electromagnetic resonator, also called a resonant cavity, or colloquially just a 'cavity,' is a hollow metal object that supports a driven three-dimensional standing electromagnetic (EM) wave in its interior. The following introduction is based on a classic toy-model of a resonant cavity, which is used for the purposes of building intuition while greatly simplifying the math with the chosen 'pillbox' geometry (seen in Figure 2.1).

The following derivation of the underlying physical concepts of electromagnetic resonators follows the approach outlined in [27].

2.1.1 Resonant modes

An example of a more familiar driven 3D standing wave is that which is supported by an pipe organ pipe: the air forced over the reed drives a pressure wave in the pipe, the resonant frequency of which is determined by the pipe's length, which we hear as pipe's pitch. The resonant pressure wave propagating in the air molecules in the pipe must meet certain boundary criteria, namely that a stationary point in the standing wave (a 'node') must exist at the closed end of the organ pipe and a region maximum oscillation (an 'antinode) must exist at the open end of the pipe. This selects the family of frequencies, or 'harmonics,' all multiples of each other, that will sound on a given pipe as a function of its length.

An EM wave is somewhat more complicated than a pressure wave. Rather than blowing air across a reed, a resonant cavity is driven by input RF power from an input antenna installed in the cavity. Instead of a single longitudinal pressure wave propagating in air molecules, EM waves consist of two orthogonal components, the oscillating electric field **E** and the oscillating magnetic field, **H**. Still, to establish a resonant mode inside a cavity, both the **E** field and **H** field must meet the boundary conditions defined by the walls of the cavity. While an infinite variety of cavities exist, the useful ones, at least in terms of the particle acceleration addressed in this thesis, have the **E** field orientated along the longitudinal axis, along the direction of particle travel. Since **E** and **H** are orthogonal to each other, the the longitudinal **E** field implies transverse **H** field. This variety of mode is referred to as a transverse magnetic or 'TM' mode. Generally, **H** refers to the magnetic field in media, and **B** refers to it in vacuum. In most applied contexts we switch to **H** as is customary, but **B** is sometimes used to reference general formulae, as seen below.

The fundamental laws of electrodynamics, the Maxwell equations, which give rise to the

orthogonally oscillating EM wave, provide another set of conditions the resonant mode must satisfy in terms of the electric **E** and magnetic **B** fields:

$$\nabla \times \mathbf{E} = i\omega\mathbf{B} \tag{2.1}$$

$$\nabla \times \mathbf{B} = -i\mu\epsilon\omega\mathbf{E} \tag{2.2}$$

$$\nabla \cdot \mathbf{E} = 0 \tag{2.3}$$

$$\nabla \cdot \mathbf{B} = 0 \tag{2.4}$$

which collectively imply,

$$(\nabla^2 + \mu\epsilon\omega^2)(\mathbf{E}) = 0 \tag{2.5}$$

$$(\nabla^2 + \mu\epsilon\omega^2)(\mathbf{B}) = 0 \tag{2.6}$$

In which the Laplacian ∇^2 operator appears. The **E** field is reflected at the cavity ends, thus nodes in the electric wave must exist at each end of the cavity. For the standing wave with components

$$A \sin kz + B \cos kz \tag{2.7}$$

In the longitudinal direction, z, this requires that the wave vector k, be

$$k = p\frac{\pi}{l} \tag{2.8}$$

where l is the length of the pillbox cavity, and $p = 0, 1, 2, \ldots$. Thus, in the language of

wave equations, $\psi(x, y)$, the z-component of $\mathbf{E}$ is

$$E_z = \psi(x, y) \cos\left(\frac{p\pi z}{l}\right) \tag{2.9}$$

In Jackson's general terms, the full solutions for the $\mathbf{E}$ and $\mathbf{H}$ in the TM mode are then given:

$$\mathbf{E} = -\frac{p\pi}{d\gamma^2} \sin\left(\frac{p\pi z}{z}\right) \nabla_t \psi \tag{2.10}$$

$$\mathbf{B} = -\frac{i\epsilon\omega}{\gamma^2} \cos\left(\frac{p\pi z}{z}\right) \hat{z} \times \nabla_t \psi \tag{2.11}$$

where ∇_t^2 is the transverse portion of the Laplacian, $\nabla^2 - \frac{\partial^2}{\partial z^2}$. Further, $\gamma^2 = \mu\epsilon\omega^2 - (\frac{p\pi}{l})^2$,

Returning to the pillbox cavity, another boundary condition imposed on $\mathbf{E}$ is that it must be zero at the cavity walls, or where the radial coordinate of the cylinder, $\rho = R$. In cylindrical coordinates then, the solution to the wave equation for E_z then becomes,

$$\Psi(\rho, \phi) = E_0 J_m(\gamma_{mn}\rho) e^{\pm im\phi} \tag{2.12}$$

Where J_m is the m-th order Bessel function, which are the family of solutions to Laplace's equation in cylindrical coordinates. γ_{mn} is defined as X_{mn}/R, where X_{mn} is the n-th root of the m-th order Bessel function, $J_m(x) = 0$. The resonant modes, ω_{mnp}, are in general:

$$\omega_{mnp} = \frac{1}{\sqrt{\mu\epsilon}} \sqrt{\frac{x_{mn}^2}{R^2} + \frac{p^2\pi^2}{d^2}} \tag{2.13}$$

The most common accelerating mode for TM cavities is the TM_{010} mode, which for a

pillbox cavity has the resonant frequency,

$$\omega_{010} = \frac{2.405}{\sqrt{\mu\epsilon}R} \tag{2.14}$$

and thus the fully solved explicit functions for the only existent components of **E** and **H** in the TM_{010} resonant mode of a pillbox cavity are:

$$E_z = E_0 J_0 \left(\frac{2.405\rho}{R}\right) e^{-i\omega t} \tag{2.15}$$

$$H_\phi = -i\sqrt{\epsilon\mu} E_0 J_1 \left(\frac{2.405\rho}{R}\right) e^{-i\omega t} \tag{2.16}$$

In graphic terms, these describe a fully azimuthal magnetic field, H_ϕ circulating around the cavity axis, increasing in strength towards the cylindrical cavity's circular walls, and a fully longitudinal electric field, E_z, which is strongest at the center of the cavity and weakens towards the outer walls. Thees components are drawn separately in Figure 2.2, and shown combined in Figure 2.3

The primary utility of the pillbox cavity is that its cylindrical shape renders the resonant modes (somewhat) hand-calculable, which is helpful for a conceptual introduction. In practice, however, it was quickly determined that this cavity shape was unsuitable for the high-fields desired for particle accelerators, given its tendency to sustain RF power-sapping resonant modes of electrons propagating in its interior in a phenomenon known as 'multipacting,' (MP), among other issues. Ultimately, in real-world cavities, the resonant EM fields are much more complex, and must be solved for numerically, with the aid of EM simulation software products, such as CST Microwave Studio, or COMSOL.

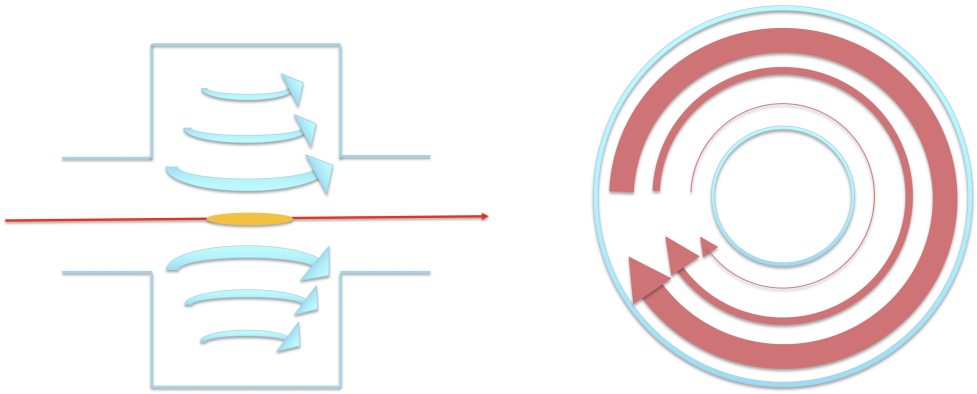

(a) (b)

Figure 2.2: (a) Sideview of the pillbox cavity depicting the electric field (blue) during the half-period of the RF cycle in which it is pointing forwards. A particle bunch (yellow) is shown traversing the accelerating gap. (b) Longitudinal view of the pillbox cavity depicting the axial magnetic field. Note, in the TM_{010} mode, the magnetic component of the electromagnetic field is strongest along the cavity walls (at the equator).

2.2 Vertical testing methods

In order to measure resonators' quality-factors (Q_0) and accelerating gradients (E_{acc}) without having to stick them in an operating accelerator, SRF scientists conduct 'vertical' tests. Superconducting RF resonators operate at cryogenic temperatures, under vacuum, and generate strong electromagnetic fields, which, in certain conditions, can generate up to 2 R/h x-rays, or higher. Vertical testing superconducting RF resonators is thus a complex and resource-intensive operation, requiring a liquid helium plant, large underground test dewars, concrete shielding, low-power and high-power RF electronics and more. Though there is some inevitable variation on vertical testing methods from laboratory to laboratory, the core concepts behind the Michigan State University vertical testing procedures, described in brief below, are representative of the technique as used throughout the community. Full descriptions of these standard methods, including more detailed derivations of the relevant

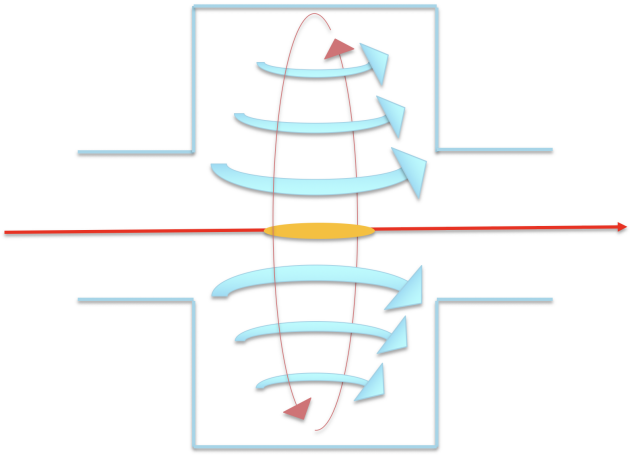

Figure 2.3: Full diagram depicting the longitudinal E field (blue) and the transverse magnetic field (red circulating) in the half phase in which a particle bunch (yellow) traverses the accelerating gap in the cavity.

equations, can be found in references such as [28] and [29], both of which are closely followed by this overview. For details relevant to the MSU/FRIB system in particular, the reader is directed to [30].

2.2.1 Figures of Merit and measurement techniques

Vertical testing an RF resonator is an exercise in getting the figures of merit one wants, (Q_0 vs E_{acc}), from what one can measure. Though single-antenna methods exist, all cavities measured for this thesis use two RF antennas or 'couplers,' shown installed in the pillbox cavity in Figure 2.4. The job of the first of these, the 'input coupler,' is to supply RF power to the cavity, which excites the resonant mode. The second antenna, the 'pickup coupler,' is used to monitor the resonant fields that the input coupler creates.

Thus, the only quantities directly measurable by researchers are the input RF power, (forward power, or P_f), the reflected RF power, which bounces back along the input trans-

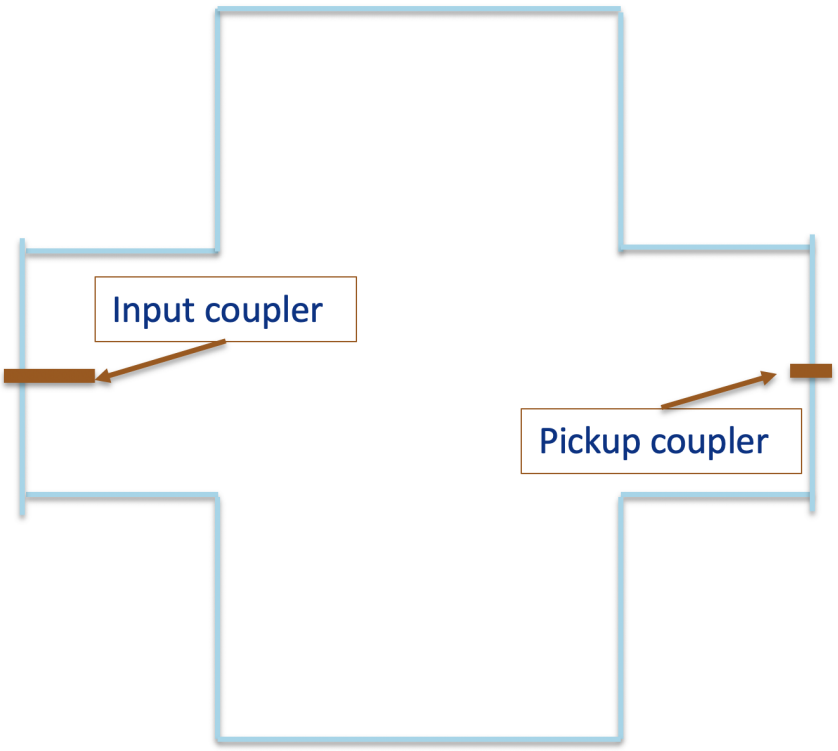

Figure 2.4: Drawing of a pillbox cavity with input and pickup couplers installed.

mission line from the input coupler (P_r), and transmitted RF power (P_t), which is measured by the pickup probe. All experimental results thus derive from these quantities.

The first most obvious calculation one can perform is to subtract the reflected and transmitted power measurements from the input power measurement, which gives the amount of power lost on the cavity walls, P_L:

$$P_L = P_f - P_r - P_t \tag{2.17}$$

It is intuitive that a highly efficient cavity would have very low P_L, and thus that P_L is directly related to the quality factor of the resonator in some way. The next step thus is to define this relation.

2.2.2 Q_0

As multiply alluded to, one of the two main figures of merit for any resonator is the intrinsic quality factor, Q_0. Intuitively, Q_0 is related to how long a resonant object such as a bell, or guitar string, 'rings' after one strikes it. The longer a resonator rings, the higher its Q_0 is. The process of 'ringing' is that of losing some portion of stored energy, dU per unit time, dt, thus Q_0 is expressed as a ratio of the total stored energy of the resonator and the energy lost per resonant cycle [27]:

$$Q_0 = -\frac{\omega_0 U}{(\frac{dU}{dt})} \tag{2.18}$$

which is easily rearranged in the more recognizable form of a differential equation,

$$\frac{dU}{dt} = -\frac{\omega_0 U}{Q_0} \tag{2.19}$$

which has the solution,

$$U(t) = U_0 e^{-\omega t/Q_0} \tag{2.20}$$

In terms more directly related to the RF resonator, this is phrased in terms of the number of oscillations at its resonant frequency, ω_0, it takes to dissipate the total energy in the resonator, U, and is defined,

$$Q_0 = \frac{\omega_0 U}{P_{Lcav}} \tag{2.21}$$

U is the total stored energy in the system, which is equivalent to the volume integral

of the energy density of the maximum electric field magnitude **E** (or, equivalently, over the maximum magnetic field magnitude, **H**):

$$U = \frac{1}{2}\mu_0 \int_V |\mathbf{E}|^2 dv = \frac{1}{2}\mu_0 \int_V |\mathbf{H}|^2 dv \tag{2.22}$$

P_{Lcav}, as stated, is the power lost on the inner surface of the cavity due to the effect of the applied RF field interacting with the momentarily unshielded normal-conducting electrons while the superconducting Cooper pairs of electrons take their time to stop and reverse direction. The losses arising here are thus the mundane resistive losses due to Joule heating, as seen in normal conducting metals, and expressed in terms of electrical resistance. Since this is often called the 'surface' resistance, ocuring within the penetration depth of the RF λ (about 40 nm) into the cavity surface, it is designated as R_S.

The loss, P_L, is thus a function of the cavity surface area exposed to the oscillating magnetic field, which has a maximum magnitude of **H**. We can thus define the Joule heating as the loss per unit surface area ds,

$$\frac{dP_L}{ds} = \frac{1}{2}R_S|\mathbf{H}|^2 \tag{2.23}$$

and thus, integrated over the total inner surface of the cavity, S,

$$P_L = \frac{1}{2}\int_S R_S|\mathbf{H}|^2 dS \tag{2.24}$$

We thus have the pieces to rewrite Q_0 from the definition, 2.21, as:

$$Q_0 = \frac{\omega_0\mu_0 \int_V |H|^2 dv}{\int_S R_S|H|^2 ds} \tag{2.25}$$

Fortunately, **H** is a calculable quantity in a resonating cavity, as shown in the exercise involving the pillbox cavity in the previous sections. For the much more complicated shapes of real-world cavities, we rely on electromagnetic simulation tools such as CST Microwave Studio, which solve for **H** numerically. The volume and surface integrals are thus usually combined as the 'geometry' factor G, which is a constant value on the order of a few hundred Ohms, defined by the cavity shape, and Q_0 becomes,

$$Q_0 = \frac{G}{R_s} \tag{2.26}$$

'intrinsic' designates this Q, Q_0, as the quality factor of the resonator itself, which is defined by power loss directly on the wall of the cavity itself, P_{Lcav}. While 2.26 is helpful intuitively since it relates Q_0 to the actual cavity surface resistance R_s, these quantities still are not directly measurable. The P_L, which includes resistive loss on the antennas, can be calculated from P_f, P_r, and P_t (Equation 2.17). The antenna-cavity system losses are captured by additional Qs related to the power losses in the input coupler (Q_{e1}) and the pickup coupler, (Q_{e2}). As a result, the Q directly calculable from power readings is really that of the entire system, which is called the 'loaded' Q, or Q_L, and is defined,

$$\frac{1}{Q_L} = \frac{1}{Q_0} + \frac{1}{Q_{e1}} + \frac{1}{Q_{e2}} \tag{2.27}$$

Thus, extracting the cavity's Q_0 depends on extracting the correct P_L, and accurately characterizing Q_{e1}, and Q_{e2}. At the beginning of a vertical test, when we still know nothing about the entire system, P_L can be estimated from the amount of time it takes for a certain amount of energy Δa to be lost over a given time, Δt. It is important to note that P_L, measured in this way, is different from the P_L defined in equation (2.17), since it includes

the two emitted powers through the couplers. In order to conduct this 'decay' measurement, the cavity is excited with RF energy and locked on resonance via a phase-locked loop (PLL). Once the system is stably resonant, power is cut, and $\Delta a/\Delta t$ is recorded with a spectrum analyzer, in dBm/s. With the conversion from dBm/s, Q_L is then, in directly measurable quantities,

$$Q_L = \frac{\omega_0 \cdot 10 \log_{10} e^1}{\frac{\Delta a}{\Delta t}} \tag{2.28}$$

After applying a little algebra to Equation 2.27, it may be rewritten as

$$Q_0 = Q_L \left(1 + \frac{Q_0}{Q_{e1}} + \frac{Q_0}{Q_{e2}}\right) \tag{2.29}$$

For the ease of subsequent calculation, it is customary to define the coupling constants, β_1,

$$\beta_1 = \frac{Q_0}{Q_{e1}} \approx 1 \tag{2.30}$$

and β_2,

$$\beta_2 = \frac{P_t}{P_L} = \frac{Q_0}{Q_{e2}} \tag{2.31}$$

and thus,

$$Q_0 = Q_L \left(1 + \beta_1 + \beta_2\right) \tag{2.32}$$

Q_L is already in-hand (2.28). The coupling of the input antenna, Q_{e1}, is customarily

designed such that it is as close as possible to being 'critically' coupled, i.e., $Q_{e1} \approx Q_0$. Q_0 can be estimated closely enough from either cavity simulation, or from prior experience, such that β_1 can be taken to be 1. The reader may have also noticed that β_2 is directly measurable: P_t/P_L. We thus finally have intrinsic cavity Q_0 completely in terms of measurable quantities!

It is worth pausing briefly to note the sources of error that can arise in this calculation (thus far). While some mismatch error can be introduced if β_1 winds up far from 1 for whatever reason, a more impactful source of error is if the power measurements, P_t and P_L have large measurement errors associated with them. At the MSU/FRIB vertical test stand, P_r and P_t are measured with a power meter that introduces approximately ± 0.1 dBm of uncertainty when measuring between about -16.0 dBm and -20 dBm, and ± 0.5 when measuring lower power levels, between -20 and -24 dBm. Since the accuracy of power meter measurements drops off precipitously at even lower power levels, effort is expended to deign pickup couplers to have a Q_{e2} such that P_t measurements higher than the accuracy floor of the power meter. Since Q_{e2} is the Q associated with the efficiency of the power transfer from the cavity field to the pickup probe, the lower Q_{e2} is, the more P_t is sent to the power meter attached to the pickup probe. Thus the balance to be struck is a Q_{e2} high enough to not affect cavity field but low enough to provide measurable P_t readings, given cable losses, etc., in the vertical test stand. This turns out to ideally be around an order of magnitude higher than the expected Q_0, but no higher.

2.2.3 Accelerating gradient, E_{acc}

The next figure of merit we seek is the cavity accelerating gradient, E_{acc} measured in megavolts (10^6 volts) per meter. This expresses how much electric potential is gained per meter of travel in the longitudinal (forward) direction in the accelerator. To get to E_{acc} from what

can be measured, the concept of shunt impedence, as applied to cavities, must be introduced. Shunt impedance is a concept borrowed from circuit theory, and applied to RF cavities via a method of analysis in which the resonant cavity is completely equivalent to a resonant RLC circuit [29]. The definition of a cavity's shunt resistance, R_{sh}, can differ by a factor of two from the more typical one used in circuit theory, so for the sake of this work, we state we shall be working with the definition for accelerator shunt impedance used by Wangler [29], which expresses the amount of voltage gained by a particle riding on the exact peak of the RF phase, V_0T, per power dissipated on the cavity wall per RF cycle:

$$R_{sh} = \frac{(V_0T)^2}{P_{Lcav}} \tag{2.33}$$

The object of cavity design is naturally to aim for high R_{sh}. Dividing this quantity by Q_0 renders it independent of cavity surface resistance, R_s.V_0T is once again calculable from EM simulation of the resonant mode of the cavity, and we arrive at another constant of the cavity design called "R over Q",

$$\frac{R_{sh}}{Q_0} = \frac{(V_0T)^2}{\omega_0 U} \tag{2.34}$$

which, like the geometry factor G, is typically on the order of a few hundred Ohms, when solved for numerically. Furthermore, since

$$\frac{R_{sh}}{Q_0} = \frac{(V_0T)^2}{Q_0 P_L cav} \tag{2.35}$$

and approximating P_{Lcav} as P_L in this instance, we can solve for the cavity voltage, V_{acc} at a given Q_0 and given P_L,

$$V_{acc}^2 = \frac{R}{Q} \cdot Q_0 P_L \tag{2.36}$$

Which merely needs to be multiplied by the effective length of the cavity, L_{eff} to be turned into a measure of the accelerating gradient, E_{acc}, which is usually reported in MV/m. One can easily see that measurement error in P_L propagates to this term as well.

Though we now have both Q_0 and E_{acc} in terms of measurable quantities, the first step of this, the 'decay' measurement, is cumbersome to conduct repeatedly, as is required to generate 15-30 data points that generally make up a Q_0 vs E_{acc} curve. One more step is thus taken to simplify the subsequent measurements: with the Q_0 calculated from the 'decay' measurement, the coupling of the pickup coupler, Q_{e2} becomes calculable, since,

$$Q_{e2} = \frac{Q_0}{\beta_2} = \frac{Q_0}{\frac{P_t}{P_L}} \tag{2.37}$$

Q_{e2} is taken as a constant of the system. Thus, once it is calculated, it may be used to find Q_0 much more easily:

$$Q_0 = Q_{e2} \cdot (\frac{P_t}{P_L}) \tag{2.38}$$

Figure 2.5 is a photograph of the user-facing parts of the RF system during a vertical test, with some of the key pieces of instrumentation labeled.

2.2.4 System error

A few sources of measurement uncertainty have already been mentioned regarding field-dependent accuracy in power meter reading and coupler mismatch error in β_1, but a bit

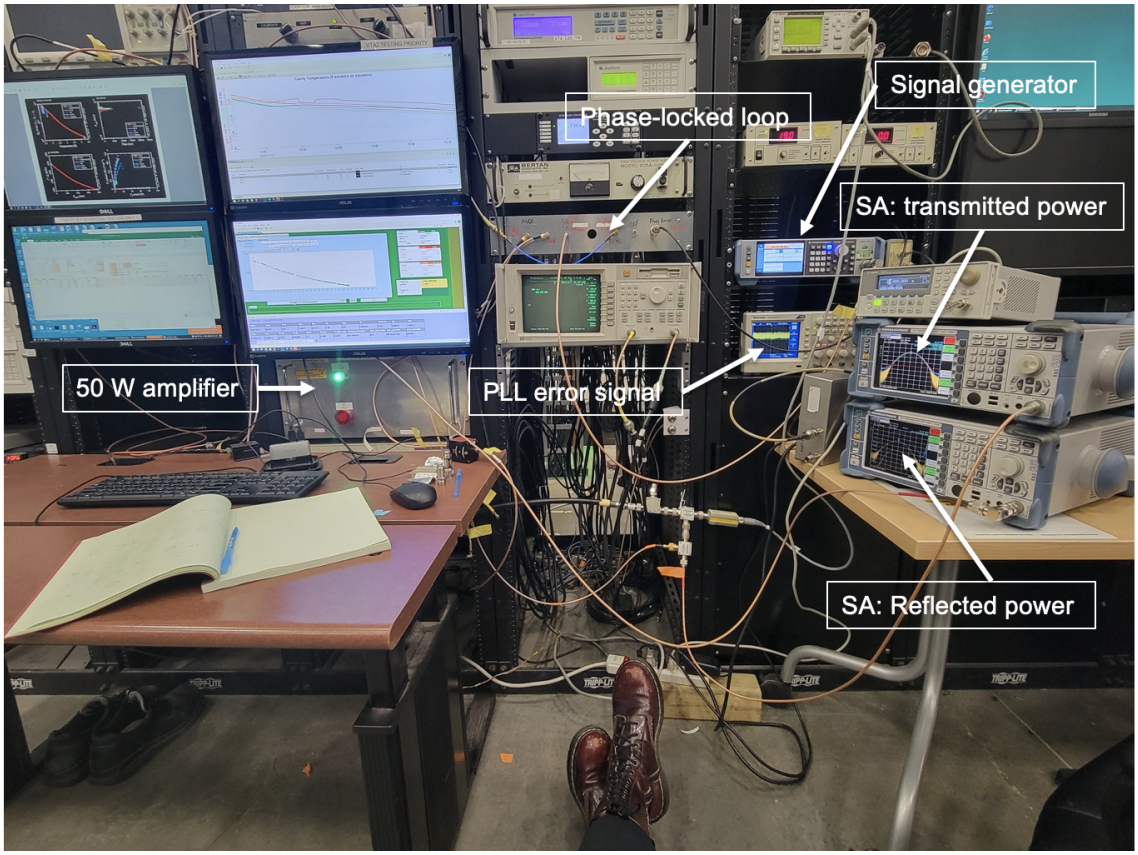

Figure 2.5: Vertical testing RF instrumentation at MSU/FRIB.

more discussion is warranted.

Careful cable calibrations are always undertaken prior to every vertical test, where the aim is the quantification losses and uncertainties in the RF transmission lines going to and from the cavity couplers. A challenge is that a cavity undergoing vertical testing changes resonance constantly due to helium bath pressure, temperature, and other variables, and the power-loses in the cables are frequency-dependent. This possible variation in the magnitude of the coupling due to frequency excursion is captured by taking the maximum and minimum of the coupling measured around the fundamental frequency.

Other components of the RF system also contribute to systematic errors: In order to protect the RF amplifier from damage from too much reflected power from the input coupling line, a circulator is installed, which contributes systematic error in coupling measurements

of the cavity-antenna system, since the circulator also becomes a part of the coupled system (with its own coupling). Ideally, for minimization of test error, care needs to be taken with every adaptor, feedthrough, splitter, coupler, in the particular configuration the vertical test RF system is in to avoid, or at least understand system loss (or mismatches) at every step. As mentioned, mismatches in P_t measurement are particularly concerning since the desired relatively weak coupling to the pickup coupler Q_{e2} can depress already low P_t, making the error propagating with it larger.

With a good understanding and characterization of these sources of error, in general practice, error in VTS measurements can be constrained to within approximately 10%. For much more detailed analyses of error in VTS, the reader is referred to [31] for the general case and [32] for a more detailed analysis of the FNAL VTS in particular.

Chapter 3

Superconductivity

The first observed property of superconductivity, in which a material cooled below a certain critical temperature, T_c, suddenly loses all electrical resistance, was initially encountered by H. Kamerleigh Onnes in 1911 [33]. This discovery was enabled by his success in pioneering the liquefaction of helium, which gave him access to temperatures on the order of 2 K, which happens to be below T_c for many materials, such as tin, lead, and mercury. (He then went on to receive the 1919 the Nobel prize in Physics "for his investigations on the properties of matter at low temperatures which led, inter alia, to the production of liquid helium" [34].).

The benefits of lossless electrical conductivity were immediately apparent, although it took a revolution in understanding brought by quantum mechanics to fully describe the essence of the phenomenon. Today, superconducting materials are found in many industrial applications, from high-current transmission lines to the high-field magnets used in MRI machines, and particle collider bending magnets.

The application of time-varying electromagnetic fields to a superconducting object elicited another rich family of physical phenomena, some of which is still awaiting a full physical explanation to this day. Superconducting RF cavity development for applications in both particle acceleration (high-field) and in novel applications for long-coherence time SRF technology such as in superconducting quantum q-bits (low-field) continues to expose gaps in our understanding of superconductivity in the presence of RF, leading to the compelling situa-

tion in which 'pure' physics research into the fundamental properties of superconductivity, a quantum-mechanical phenomenon, can directly advance an applied technology.

This chapter provides a brief overview of superconductivity, then shifts to focus on the aspects of the basic theory that provide preliminary insight into the behavior of a superconducting object in the presence of an oscillating RF field. A few classic models of the phenomena are outlined, and used to illustrate certain phenomena in superconducting cavities, which will be significant in understanding the experimental data presented in the subsequent chapters in this thesis.

3.1 Descriptions of Superconductivity

The two hallmarks of a superconducting material are 1. perfect electrical conductivity and 2. perfect diamagnetism. While Onnes' 1911 discovery of perfect conductivity first alerted physicists to the existence of superconductivity, 22 years passed before physicists Meissner and Ochsenfeld first noticed that a superconducting object *expelled* all applied magnetic field, rendering the interior magnetic field of the superconductor not just constant, as is the case in normal-conducting objects, but precisely zero [35]. This subtle yet profoundly weird 'Meissner' effect, shown in Figure 3.1, ultimately requires a quantum mechanical description, however it is possible to think of this magnetic field exclusion as the effect of some kind of magnetic pressure that could be exerted by the material against outside fields, up to the material's magnetic critical field, H_c, which is a function of temperature [36]. Empirically, $H_c(T)$ was found to be parabolic [36]:

$$H_c(T) \approx H_c(0)[1 - (T/T_c)^2] \tag{3.1}$$

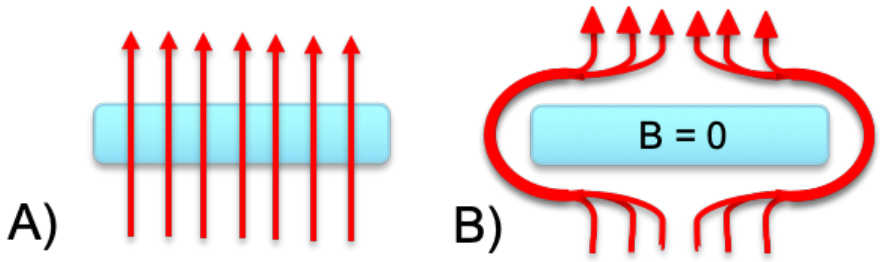

Figure 3.1: Drawing of the Meissner effect. An applied magnetic field (red) interacting with a superconducting material (blue) (A) at a temperature above T_c and (B) at a temperature below T_c.

The superconducting critical fields is central to describing the properties of a particular superconducting material, and we shall return to this idea repeatedly, with a few modifications, in discussions of the properties of superconducting niobium and potential superconducting RF cavity surface treatments.

Though the earlier models of superconductivity have long been supplanted with much more sophisticated theoretical frameworks, they still provide a useful system of introduction to the phenomenon since each manage to capture, relatively intuitively, one or more important features of the superconducting effect relevant to SRF.

The simplest of these arose from analogies with the phenomenon of superfluidity. The Two-Fluid model, first suggested by Groter and Casimir in 1934 [37], simply treats a superconductor as having two populations of electrons, one with normal-conducting properties n_n and another with superconducting properties, n_s. The relative population of these electrons is controlled by the temperature dependence,

$$n_s = n_n[1 - (T/T_c)^4] \tag{3.2}$$

Later, this will provide a useful basis for describing the conductivity of a superconductor under an RF field. Notably, however, this model leaves out any description of the Meissner

effect.

3.1.1 London Equations

In the early 1930s, F. and H. London sought to improve upon the Two-Fluid model by developing a mathematical description of superconductivity that covered both perfect conductivity and perfect diamagnetism, i.e., the Meissner effect. To address the first of these properties, they began with the standard Drude model of electrical conductivity, which treats conduction electrons classically, as having some velocity. In normal conducting materials, these experience scattering events on the time scale of τ in the material they are traveling in. Thus, by $F = ma$, [36]:

$$m\frac{d\mathbf{v}}{dt} = e\mathbf{E} - m\frac{\mathbf{v}}{\tau} \tag{3.3}$$

and Ohm's law for normal conducting materials, $J = (ne^2\tau/m)\mathbf{E} = \sigma\mathbf{E}$ emerges. In order to make an analogous law for superconductors, the Londons simply removed the scattering term, which allowed them to write,

$$\frac{d\mathbf{J_s}}{dt} = \left(\frac{n_s e^2}{m}\right)\mathbf{E} \tag{3.4}$$

and then, by introducing the parameter Λ,

$$\Lambda = \frac{m}{n_s e^2} = \frac{4\pi\lambda^2}{c^2} \tag{3.5}$$

they produced the First London Equation,

$$\mathbf{E} = \frac{\partial}{\partial t}(\Lambda \mathbf{J_s}) \tag{3.6}$$

Integrating with respect to time and invoking Faraday's law, this can be rewritten

$$\nabla \times J_s = \frac{n_s e^2}{m}\mathbf{H} \tag{3.7}$$

which contains the first mathematical expression of the Meissner effect. Further work with the Maxwell equations, specifically Ampere's law and Gauss' law, (and a vector identity) they arrived at the second London Equation

$$\nabla^2 \mathbf{H} = \frac{\mathbf{H}}{\lambda^2} \tag{3.8}$$

where

$$\lambda^2 = \frac{mc^2}{4\pi n_s e^2} \tag{3.9}$$

λ is the London penetration depth, and perhaps the most significant consequence of the London's purely phenomenological analysis is the implication that the interior of a superconducting material is screened from applied electromagnetic fields over the depth λ from the surface. Thus, the field attenuation over the surface depth of the (bulk) superconducting material ($H(z)$) is

$$H(z) = H(0)e^{-\frac{x}{\lambda}} \tag{3.10}$$

λ_L, has been found to have the temperature-dependence,

$$\lambda(T) \approx \lambda(0)[1 - (T/T_c)^4]^{-1/2} \tag{3.11}$$

Intriguingly, this is a recurrence of the (inverse) T^4 dependence first encountered in the Two-Fuid model. While the above treatment considers a static applied field, time derivatives of the Maxwell equations can be used to show that the same is true for a time-varying (RF) field.

λ describes a critical length scale for superconducting niobium cavities (about 39 nm). All of SRF innovation is aimed at reducing the resistive surface losses that occur from the incursion of the RF filed into those few nm. Moreover, all RF surface treatment effects are only relevant to RF performance within this length scale.

With the London equations in-hand, we briefly return the two-fluid model to derive a reasonable representation of the total conductivity of a superconductor, $\sigma = \sigma_n + \sigma_s$. The normal conducting electrons of the two-fluid model, n_n, can be used to define the normal-conducting current, j_n, which has normal conductivity σ_n given by [28],

$$\sigma_n = \frac{n_n e^2 \tau}{m} \tag{3.12}$$

to find σ_s in the presence of RF, the superconducting current j_s takes on the time-varying form, $j_s = j_{s0} e^{i\omega t}$. Applying the first London equation, we find that

$$j_s = \left(\frac{i\omega}{\mu_0 \lambda_L^2} \right) E \tag{3.13}$$

and thus we may identify the quantity in brackets as σ_s. Rewriting this in terms of λL, we find,

$$\sigma_s = \frac{n_s e^2}{m\omega} \tag{3.14}$$

Following the same procedure to find j_n in the presence of RF, we finally arrive at

$$\sigma = \frac{n_n e^2}{m\tau}\left(\frac{1}{1+i\omega\tau}\right) + i\frac{n_s e^2}{m\omega} \tag{3.15}$$

Which predicts a ω^2 frequency dependence of σ. Though later theories (namely, the BCS theory) will give rise to a more accurate model for the entire range of frequency dependence, for the frequencies SRF cavities typically operate at, the ω^2 dependence holds well. While this may seem to suggest that high-frequency cavities are to be avoided, it shall be shown in the focused discussion of SRF cavities that the temperature-dependence of the superconducting surface resistance offsets this.

3.1.2 Pippard model

Experimental measurements of λ in superconducting materials soon revealed the measured λ was always lager then predicted by the London equation for λ_L. A. B. Pippard (1953) rectified this discrepancy by modifying the Londons' work to include nonlocal effects, which he assumed had some characteristic length scale defined by the uncertainty principle ($\Delta x \Delta p \geq \hbar$) [**Pip**]. Assuming only electrons within about $k_B T_c$ of the Fermi surface could be promoted to the supercurret, a range of momenta, Δp can be defined for these as $k_B T_c / v_f$ where v_f is the Fermi velocity and thus:

$$\Delta x \geq \frac{\hbar}{p} \approx \frac{\hbar v_F}{k T_c} \tag{3.16}$$

This expression for Δx, which incorporates the first quantization of a theory of superconductivity with the introduction of $\hbar$, allowed the definition of the characteristic length scale Pippard was seeking, ξ_0,

$$\xi_0 = a\frac{\hbar v_F}{kT_c} \tag{3.17}$$

ξ_0 thus describes the physical size limit of the superconducting current carriers in a purely superconducting material. Pippard's full generalization of the London equations to include nonlocal effects provides for the presence of possible scattering centers, quantified as the electron mean free path l. These give the true ξ of the superconducting material, as

$$\frac{1}{\xi} = \frac{1}{\xi_0} + \frac{1}{l} \tag{3.18}$$

Pippard's work thus modified the London-predicted penetration depth λ_L, arriving at

$$\lambda = \lambda_L \left[1 + \frac{\xi_0}{l}\right] \tag{3.19}$$

which shows excellent agreement with experimental data [**Pip**]. Beyond demonstrating the success of the Pippard's incorporation of nonlocal effects into the London framework, this expression is an exceedingly useful formulation in the context of SRF surface preparation research. SRF surface treatments, particularly the advanced treatments N-doping and furnace baking, amount to controllable modifications of niobium l. These move the superconducting material along a continuum between the 'clean' limit (long l) of the superconducting regime to the 'dirty' limit (short l). The expression above makes it obvious that the purity of the niobium material not only affects the size of the superconducting carriers ξ, but also the RF

penetration depth into the material, which has all the implications discussed earlier [38] [36].

3.1.3 BCS Theory of Superconductivity

The field of superconducting research had to wait until 1957 to receive a microscopic description, ultimately provided by J. Bardeen, L. N. Cooper, and J. R. Schrieffer, and subsequently referred to as "BCS theory."

The core insight of Bardeen, Cooper, and Schrieffer's theory is that the supercurrent-carrying objects that the Two-Fluid model handled as n_s, σ_s, j_s, etc. are approximately analogous to a Bose-Einstein condensate of electron *pairs*, called Cooper pairs. This was prompted by experimental evidence collected by multiple investigators that demonstrated a minimum energy gap of a few times $k_B T$ existed between the normal and superconducting excitations, and that these excitations always occurred as (apparent) pairs of fermions. Bardeen, Cooper, and Schrieffer were able to show that interactions between electrons, and the vibrations of the metallic lattice in which they propagated, called phonons, could give rise to an energetically favorable state in which one spin-up electron and one spin-down electron propagated through the lattice together, as a pair. Simplistically, this is often explained in terms of one electron distorting the metallic lattice in such a way that it attracts a second electron, or, in other words, the leading electron exchanges a photon with the lattice phonon which then exchange a photon with a the trailing electron.

As a set of Fermions, Cooper pairs' collective spin is actually an integer, 1. They thus they obey Bose-Einstein statistics, and define a ground state energetically below that of the unpaired electrons' state. BCS theory develops a Hamiltonian for this system, from which follows an expression for the equilibrium ($T = 0$) size of the superconducting energy gap, $\Delta(0)$ [39] [40]:

$$\Delta(0) = 2\hbar\omega e^{-1/N_0 V_0} \tag{3.20}$$

where N_0 is the electron density of states in the normal conducting metal, and ω and V_0 are parameters from the system Hamiltonion, in which V_0 is roughly analogous to the electron coupling. The density of states of the superconducting material as a function of this superconducting gap is,

$$\frac{N}{N_0} = \frac{E}{\sqrt{E - \Delta^2}} \tag{3.21}$$

Once again, only the populations particles (and phonons) within about $k_B T_c$ ($\hbar\omega$) of the Fermi surface need to be considered. BCS theory also relates the electron pairing energy to T_c, leading to a re-write of the Pippard coherence length ξ_0 in terms of $\Delta(0)$ [28],

$$\xi_0 = \frac{\hbar v_F}{\Delta(0)} \tag{3.22}$$

As we move up in temperature from absolute zero ($T = 0$), Δ begins to deviate from $\Delta(0)$ as single-electrons slowly begin unpairing and acting like analogues of the normal-current population of n_n charge carriers from the two-fluid model. An approximation of this temperature-dependence of Δ is given by [28],

$$\frac{\Delta(T)}{\Delta(0)} = \left[\cos\left(\frac{\pi}{2}\frac{T}{T_c}\right)\right]^{1/2} \tag{3.23}$$

The primary significance of BCS theory to SRF is that it enabled a microscopic description of the effect of a time-varying magnetic field on a superconducting system. This theoretical treatment was undertaken by Matthis and Bardeen [41], who used a nonlocal

generalization of the BCS theory and perturbative methods to find the complex surface impedance [41],

$$\frac{Z_s}{Z_n} = \left(\frac{\sigma_1 - i\sigma_2}{\sigma_n}\right)^n \tag{3.24}$$

Where the exponent n can be found in the non-local Pippard limit to be $-1/3$ [42]. Tailoring this result to the case of the weak coupling V_0 of niobium and normal SRF cavity operation at 2K, it can be refactored as the BCS theory-derived prediction for the superconducting surface resistance, R_{BCS} [41][28][42],

$$R_{BCS} = \frac{A(l, \omega, T...)\omega^2}{T} e^{-\frac{\Delta 0}{k_B T}} \tag{3.25}$$

where the prefactor A is generally taken to be a material-dependent constant, loosely a function of mean free path (l), frequency, temperature, etc. Out of respect for the profundity of this derivation, and its relation to BCS theory, this result of Mattis and Bardeen has been discussed first. However, the derivation of the expected RF surface resistance of a superconductor is yet another instance in which, the Two-Fluid model actually provides an intuitive, albeit less rigorous, approach to the same solution. In brief, if we can use the band gap $\Delta(0)$ as described by BCS theory to describe n_n in a superconductor as a the following function of T, we have

$$n_n(T) \propto e^{-\frac{\Delta(0)}{k_B T}} \tag{3.26}$$

If we are to use this description to find R_{BCS}, we must describe the effect of the EM field, penetrating over the distance λ into the surface of the niobium material, on the normal-

conducting electrons, of number n_n. Since one can state in terms of the internal electric field, E_{int} [28],

$$E_{int} \propto \frac{dH}{dt} \propto \omega H \tag{3.27}$$

and since,

$$J_{int} \propto n_{norm} E_{int} \propto n_{norm} \omega H \tag{3.28}$$

we arrive at

$$P_{Lcav} \propto E_{int} J_{int} \propto n_{norm} \omega^2 H^2 \tag{3.29}$$

and since as discussed in Chapter 2, the RF losses are a function of the superconducting surface resistance R_s and the applied magnetic field $\mathbf{H}$ along the surface area of the cavity S, we acquire,

$$P_{Lcav} = \frac{R_s}{2} \int_S |H|^2 dS = \frac{R_s}{2} \mathbf{H}^2 \tag{3.30}$$

We can produce from the above,

$$R_{BCS} = \frac{A\omega^2}{T} e^{-\frac{\Delta 0}{k_B T}} \tag{3.31}$$

Which is the common expression cited throughout the SRF community, the ubiquity of which is what motivated the refactoring of the Matthis-Bardeen result, to emphasize the equivalence between the two despite disparate origins.

The expression for R_{BCS} has several important features: the frequency-squared relation is present, and the influence of factors affecting $\Delta(0)$ also clearly have some effect on R_{BCS}. A is commonly called a material parameter, and is related to the relative purity of the niobium material (a function of l). Furthermore, a strategic usage of the reduced temperature, T/T_c makes the exponential dependence of R_{BCS} on T_c/T explicit:

$$\ln(R_{BCS}) \propto -\frac{\Delta(0)}{k_B T}\left[\frac{T_c}{T}\right] \tag{3.32}$$

Given that temperature is a controllable parameter in SRF cavity testing, this relation proves extremely useful. Anticipating the subject of the next few sections slightly, one can observe here that decreasing T in the context of a test allows for T-independent components of R_s to become more obvious.

As a final note, in the clean limit of niobium, H. Padamsee generated a good numerical fit for R_{BCS} relevant to SRF cavities. This "Padamsee Formula" for niobium in the clean limit is [28]:

$$R_{BCS} = 2 \times 10^{-4} \frac{1}{T}\left(\frac{f}{1.5}\right)^2 e^{-17.67/T} \tag{3.33}$$

which is a useful benchmark to reference in the testing of SRF cavities.

3.2 Other contributions to R_s

As alluded to, R_{BCS} as previously formulated does not adequately explain experimental SRF results: if R_{BCS} is the only source of resistive losses under the influence of an RF field, the T dependence suggests that reducing T should reduce the total RF surface resistance,

R_s through the closest approach to absolute zero helium refrigeration technology can take us to today. Experimentally, this was quickly found to not be the case: in SRF cavities, R_s saturates at some T, and retains a constant value well after R_{BCS} becomes negligible, and thus it would seem,

$$R_s = R_{BCS}(T) + R_0 \tag{3.34}$$

Factors affecting the temperature-independent component of this expression, termed 'residual' resistance or R_0 are the subject of significant focus in SRF since, depending on the SRF cavity preparation and operation parameters, R_0 has the potential to dominate R_S. In the operating temperature range of most SRF cavities, i.e., from 4 K to 2 K, it is possible for a changeover to occur such that at higher T, R_{BCS} dominates and at lower T, R_0 dominates. As shall be demonstrated in the experimental portions of this thesis, the project of optimizing Q_0, which is equivalent to the project of minimizing R_s, is a tricky balance of using the methods available to modify the quantum surface structure of this system (l and dependent parameters ξ, λ, etc.), in such a way as to reduce *both* R_{BCS} and R_0. As is too often the case in SRF, it transpires that some process that significantly reduces R_{BCS} increases R_0 or vice versa. We thus close this chapter on superconductivity with formulations of superconductivity that provide some insight on the other contributions to R_0.

3.2.1 Landau-Ginzburg representation of Superconductivity

Quite some time has been dedicated to deriving the two fundamental length scales of a superconductor, ξ, the length scale of the superconducting Cooper pairs, and λ, the characteristic length over which the EM fields decay into the, bulk of the superconducting material.

No intrinsic relative relation between these two parameters exists, leading to the two-fold possibility that 1. ξ could be longer, or 2. λ could be longer, depending on the material properties.

The Landau-Ginzburg formulation of superconductivity [43], which notably *predates* the BCS theory, applies thermodynamic concepts to the problem of superconductivity, and thus describes the superconducting state as a realization of Landau's second-order phase transition, applied to a small slowly varying wavefunction [36],

$$n_s = |\psi(x)|^2 \tag{3.35}$$

writing the free energy density of the superconducting states, f_s, in terms of the typical expansion [43] around the normal conducting energy density f_n,

$$f_s = f_n + \alpha|\psi|^2 + \frac{\beta}{2}|\psi|^4 + \frac{1}{2m*}\left|\left(\frac{\hbar}{i}\nabla - \frac{e*}{c}\mathbf{A}\right)\right|^2 + \frac{h^2}{8\pi} \tag{3.36}$$

where $\mathbf{A}$ is the vector potential, m* and e* are the effective electron mass and charge, (and α and β are phenomenological constants). One then takes the derivative of the expression for f_s and minimizes it, which gives what are known as the 'Landau-Ginzburg' equations [36],

$$\alpha\psi + \beta|\psi|^2\psi + \frac{1}{2m*}\left(\frac{\hbar}{i}\nabla - \frac{e*}{c}\mathbf{A}\right)^2\psi = 0 \tag{3.37}$$

and

$$\mathbf{J} = \frac{e*}{m*}|\psi|^2\left(\hbar\nabla\phi - \frac{e*}{c}\mathbf{A}\right) = e*|\psi|^2\mathbf{v_s} \tag{3.38}$$

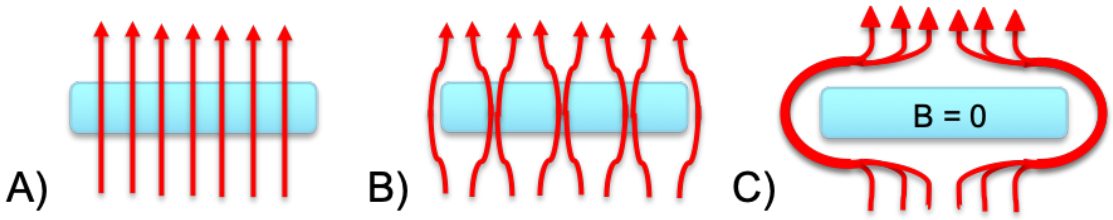

Figure 3.2: Cartoon depiction of magnetic field lines (red) interacting with A) normal conducting material, B) Type-II superconducting material, and C) Type-I superconducting material, the latter two being below their critical temperatures, T_c.

where the solution (root) of the first equation is $\psi = -\alpha/\beta$. The primary consequence of the Landau-Ginzburg equations is that they provide a means to define both ξ and λ, which can then be cast in terms of the Landau-Ginzburg parameter $\kappa = \lambda/\xi$. The form of these two expressions [43] gives rise to the expression for κ:

$$\kappa = \frac{\lambda_{GL}}{\xi_{GL}} = \frac{m * c}{\hbar e}\left(\frac{\beta}{2\pi}\right)^{1/2} \tag{3.39}$$

if κ is less than $1/\sqrt{2}$, the material is characterized as a "Type-I" superconductor. The defining characteristic of these Type-I superconductors is that the 'magnetic pressure' formulation for H_c from the beginning of this chapter holds, defining a simple division in the H vs T plane between the superconducting and non-superconducting regions. The applied magnetic field in this case is either entirely expelled, or totally overwhelms the sample, at which point it becomes normal conducting.

On the other hand, if κ is more than $1/\sqrt{2}$, an intermediate state of *some* flux penetration becomes energetically favorable, which is the hallmark of a 'Type-II' superconductor, drawn in Figure 3.2.

Niobium is a Type-II superconductor, and thus subject to complex additions to R_s due to the behavior of these magnetic fluxons trapped in the bulk niobium of the superconducting

RF cavity. A crude model of these fluxons imagines them as cylinders penetrating the bulk niobium with normal conducting cores. Electric current circulates around these fluxons penetrating the bulk material, the strength of which decays over λ into the bulk niobium, about 40 nm for clean niobium. The dimension of this normal conducting core is set by the coherence length, ξ which again is around 38 nm for niobium in the clean limit.

Quench, the phenomenon of the superconductor being driven out of the superconducting state and suddenly returning to the normal conducting state, is a key limiting factor for SRF cavities. In general, formulations of H_{c2} are important to understanding how to increase the EM field tolerated by the cavity before quench occurs. In the context of niobium SRF cavities, H_{c2} is around 500 mT for very clean Nb, and increases even more in the 'dirty' (short l) limit, however in practice cavities have so far been limited to around 200 mT.

These magnetic voticies, or fluxons, are quantizations of the magnetic field, Φ_0, in a superconducting object,

$$\Phi_0 = \frac{h}{2e} = 2.07 \times 10^{-15} \tag{3.40}$$

in Tm^2. H_{c2} is then given as,

$$H_{c2} = \frac{\Phi_0}{2\pi\mu_0\xi_0^2} \tag{3.41}$$

where

$$H_c = \frac{H_{c2}}{\sqrt{2}\kappa_{GL}} \tag{3.42}$$

A notional drawing of the phases of a Type-II supercondcutor is found in Figure 3.3

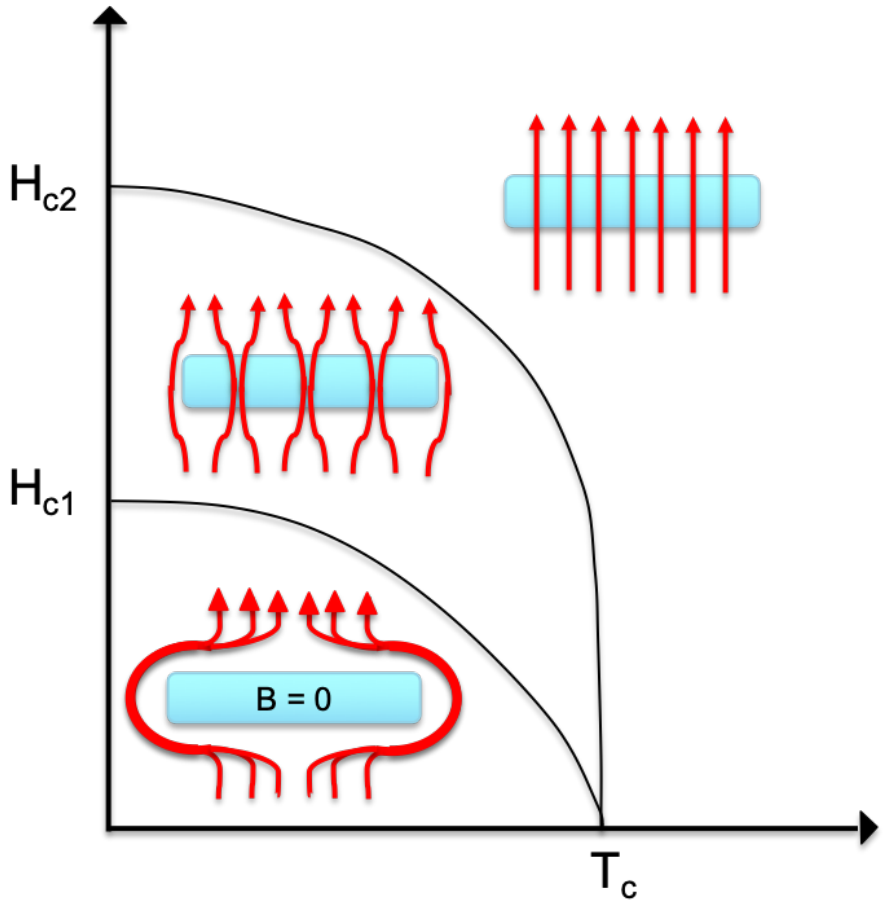

Figure 3.3: Schematic diagram of the three different regions of the Type-II superconducting phase diagram, defined by the lower and upper critical magnetic fields (H_{c1} and H_{c2}), and the critical temperature, T_c.

To summarize a somewhat mathematical chapter, the concept of losses in a superconducting material seems contradictory: normally, in the presence of steady-state (DC) electromagnetic fields, a superconducting material is *perfectly* conductive. The superconducting Cooper pairs, which constitute the supercurrent, are able to perfectly shield the population of normal conducting electrons from outside time-invariant fields.

In the presence of RF, however, the perfect conductivity that defined the superconducting phenomenon ($R_s = 0$), is no more. Since electrons have mass, and thus have inertia, they take a nonzero amount of time to slow, stop, and change direction under the influence of the

oscillating RF field. Since the oscillating RF field consists of photons, which are massless, it is impossible for the electrons forming the supercurrent to keep up with the speed of the RF transition.

Thus, there are periods in the RF cycle where the supercurrent is unable to completely shield the normal conducting electrons from the applied RF field, which penetrates a depth $\lambda \approx 40$ nm into the superconducting surface. In this layer, the RF field interacts with the population of unshielded, normal-conducting electrons present. These normal conducting electrons are subject to the surface resistance of the cavity, R_s, which has two major components: 1. the temperature-dependent component, which is well-described by the BCS theory of superconductivity, and 2. the temperature-independent component, which can generally be a function niobium material parameters, such as the electron mean free path l, and can be increased by flux trapping. Both R_{BCS} and R_0 have EM field dependencies, which shall be explored in the upcoming chapters.

We have thus set the stage for nearly the entire field of (high-Q_0) SRF research: We wish to increase Q_0, which is an inverse function of the RF surface resistance, R_s. Some properties of R_s are known, some have sound theoretical underpinnings, and some remain unknown. As SRF scientists driving towards high-Q_0 cavities, we must manipulate the properties of the Nb surface through cavity processing techniques to minimize both R_0 and R_{BCS}. The story that shall unfold over the remainder of this work is that techniques that improve one often harm the other, and the optimum Q_0 treatment becomes a balancing act of the various benefits and drawbacks of each treatment, and the specific context in which these cavities can be expected to operate in.

Chapter 4

FRIB400 prototype cavity design and validation

The materials appearing in this chapter form the basis of the published work, "Medium-velocity superconducting cavity for high accelerating gradient continuous-wave hadron linear accelerators," published in the Physical Review of Accelerators and Beams, November, 2021 [44].

4.1 The FRIB400 cavity

As outlined in the introduction, the goal of the FRIB400 energy upgrade project is to double the end-energy of the FRIB driver linac from 200 MeV/u to 400 MeV/u of the heaviest uranium ions, which equates to about 1 GeV for protons [12]. The design of an SRF cavity for this upgrade–or any project–amounts to a complex optimization process across many free parameters. Some of these are constrained by fundamental limitations of physics, such as the aforementioned superheating field, which is the maximum RF magnetic surface field that can be sustained by the cavity niobium, a type-II superconductor, and is around 200 mT [45]. Other parameter values are dictated by more mundane concerns, like the physical dimensions of the remaining space in the linac tunnel (80 m) into which the upgrade segment must fit,

and still achieve the targeted upgrade energy increase. Additional cost-driven considerations of design include the minimization of construction and operating costs, which, as is the case in nearly all SRF applications, primarily means minimizing heat load that the SRF cavities impose on the cryogenic system. To illustrate the point: 2 K, an expected wall-plug efficiency for a helium refrigerator can be between 750 (optimized) and 1,000 (general) W/W (watts of wall-plug power needed to remove 1 watt of heat at 2K) [46]! Aiming for the highest cavity quality factor possible is the most direct way to reduce the number of watts dumped into the cryogenic system from cavity RF losses, thus cavity design is tightly coupled to proposed strategies for achieving the highest possible Q_0. In the broad context of large linacs, raising the cavity Q_0 by even a factor of two can be the difference between needing one cryoplant or needing more [47]. High-Q is of particular concern for FRIB since, unlike preceding machines of a similar scale (e.g., the Spallation Neutron Source (SNS) or European Spallation Source (ESS)) it is a continuous-wave (CW) linac, which places high demands on cavity Q_0, since we cannot save the heating budget by simply having the cavity off for part of the duty cycle, as pulsed machines do.

In this chapter we review the principal design considerations that lead to the selection of the FRIB400 $\beta = 0.6$ 644 MHz 5-cell elliptical cavities, then move to the preliminary testing and analysis of the two prototype 5-cell cavities fabricated at Research Instruments (RI) (GmbH), and delivered to FRIB in the fall of 2018. Since these cavities are the first of their type, time will be taken to establish the feasibility of the design, in terms of both mechanical and RF stability, in a way that would be unnecessary if this had been a high-β application employing TESLA-type cavities, a design with a long and successful history. Finally, we apply and assess three "conventional" RF surface treatments, which have been used successfully in many SRF applications worldwide. These are 1. electropolishing (EP),

2. EP+120°C baking, and 3. buffered chemical polishing (BCP)+120°C baking. It is crucial to note that the intent at this stage is not to determine which of these, if any, should be used in the FRIB400 upgrade project proposal. The intent here is to demonstrate that reasonable RF performance can be attained in these novel cavities, which will provide the ultimate validation of their fundamental design, and justify subsequent focused high-Q_0 studies in these cavities. These focused high-Q studies, including the advanced techniques of nitrogen-doping and furnace baking, have the potential to reach much higher Q_0 than the conventional recipes studied in this chapter, provided they can be successfully adapted from 1.3 GHz TESLA cavities to the $\beta = 0.6$ 644 MHz 5-cell elliptical cavities. This subject will be treated at length in the following chapter on Advanced Techniques.

4.1.1 Design parameters

In the course of the FRIB400 cavity design study [48], multiple cavity types and operating frequencies were considered. Simply adding more of the FRIB linac baseline $\beta = 0.53$ half-wave resonators is the simplest idea, technologically speaking, but these cavities are not able to meet the upgrade energy requirement in the 80 m of space available [48].

While there are currently no continuous-wave (CW) SRF linacs operating in the 200 MeV/u to 400 MeV/u energy range using elliptical cavities, the elliptical cavity style is attractive in this application for several reasons. The shape has a strong history in research and development for high-energy physics applications, operating mainly in the high-velocity regime ($\beta \approx 1$) and multiple industrial partners have experience manufacturing this type of cavity at scale. Moreover, its history in high-gradient applications make elliptical cavities good candidates for delivering the highest energy gain per unit of linear distance, which is a key parameter to maximize given one of the strongest constraints on the problem is the

80 m of space left in the tunnel. Its relatively simple, axisymmetric shape with large beam ports also make the inner surface easily accessible for cleaning and processing treatments.

The number of elliptical cells per cavity was chosen such that the energy gain is maximized for particles at energies between 200 MeV/u to 400 MeV/u. Given the unique range of species FRIB aims to accelerate, from the heaviest uranium ions all the way down to protons, the energy gain needs to remain at least positive all the way up to 1 GeV (the upgrade energy when applied to protons) [48]. The energy gain per cavity, ΔW, is a function of the transit time factor, (TTF), which is a function of the number of cavity cells, N. To optimize the function for the FRIB400 cavity, the expression for TTF,

$$T(N,\beta,\beta_G) = \begin{cases} (\frac{\beta}{\beta_G})^2 \sin(\frac{N_\pi}{2\frac{\beta}{\beta_G}} + \frac{N_\pi}{2}) \frac{(-1)^{N-1}}{N((\frac{\beta}{\beta_G})^2-1)} & \\ \frac{\pi}{4} & \text{if } \beta = \beta_G \end{cases} \tag{4.1}$$

was used [48], which is independent of operating frequency. ΔW, the energy gain per nucleon per cavity, is proportional to this value, thus:

$$\Delta W = \frac{QeV_0^A T_{eff} \cos(\phi_s)}{A} \tag{4.2}$$

where T_{eff} is the transit time factor of a particle traveling at any β normalized to that of the optimal particle, β_{opt}, vis., $T_{eff} = \frac{T(N,\beta,\beta_G)}{T(N,\beta_{opt},\beta_G)}$[48]. ϕ_s is the synchronous phase. As the number of cells, N, increases, the range of particle energies, β, over which the TTF is maximized narrows considerably. At the high end, a 9-cell elliptical cavity TTF is only maximized between about 250-350 MeV/u, and becomes negative around 600 MeV/u. The need for the beam energy gain to remain high all the way up to 0.6 GeV/u strongly constrained the cavity cell number to six or fewer.

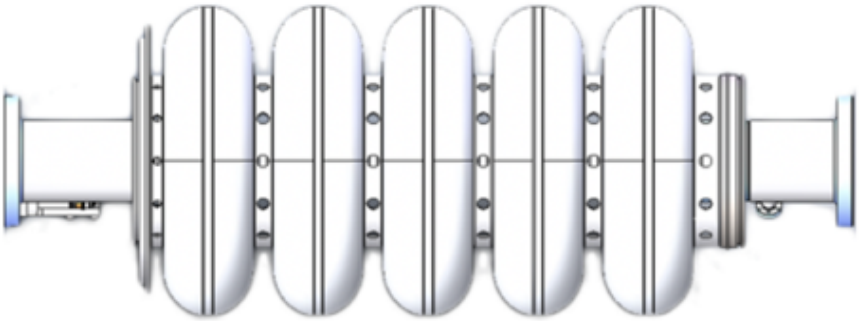

Figure 4.1: Drawing of the FRIB400 5-cell cavity.

Now, the question of operating frequency comes into play: the initial quarter-wave resonators of the FRIB driver linac operate at a frequency of 80.5 Hz, and the subsequent half-wave resonators operate at 322 MHz. Upgrade cavity frequencies of 644 MHz, 850 MHz, and 1288 MHz were thence studied in 5- and 6-cell formats, where the cavity geometry was scaled such that each cavity had a peak surface electrical gradient,E_{peak}, of 40 MV/m. Of all options considered, only the 5-cell, 644 MHz cavity (Figure **??**) proved able to achieve the needed gradient to accelerate uranium ions to 400 MeV/u within 80 m. This design minimizes the number of additional cryomodules and supporting systems that would have to be constructed, and minimizes the total additional dynamic heat load of the upgraded segment, estimated to be 938 W at 2 K, provided that the cavities can be processed to an intrinsic quality factor of 2×10^{10} at 17.5 MV/m or better.

This frequency choice thus dictates the length of the half-cell, $L = \beta_G \lambda/4$, with λ being the RF wavelength, $\lambda = c/(2\pi f)$. The 5-cell 644 MHz design for the FRIB400 has benefit of being similar to the 5-cell 650 MHz cavities under parallel development for Fermilab's Proton Improvement Plan II (PIP-II) linac. The PIP-II linac upgrade incorporates two segments consisting of 5-cell cavities operating at 650 MHz: the penultimate stage at velocity $\beta = 0.6$, and the final stage at $\beta = 0.9$ [15].

Though the cavity surface geometry is optimally designed to minimize the peak surface

electric fields (decreasing the likelihood of field emission) and magnetic fields (decreasing the liklihood of quench), while maximizing accelerating voltage, the cavity aperture diameter sizing also must optimize the TM_{010} accelerating mode. Decreasing the iris diameter has the benefit of decreasing the field enhancement factors, E_{peak}/E_{acc} and B_{peak}/E_{acc}, and decreases the shunt impedance, reducing heat losses [48]. However, narrow apertures also reduce the cell-to-cell coupling, negatively affecting the field-flatness. Narrower apertures also start to hinder cavity processing techniques, particularly ones that rely on fluid-flow through the cavity, and reduce the mechanical stability of the cavity. Through optimization of all of these parameters, an aperture diameter of 83 mm was ultimately settled on for the FRIB400 cavity [48].

A summary of these key cavity parameters are included in Table 5.1.

Table 4.1: FRIB400 Cavity Parameters

Frequency	644 MHz
Geometric β	0.61
Optimal β	0.65
Aperture diameter	83 mm
Effective length (L_{eff})	71.0 cm
Number of cells	5
Geometric shunt impedance, R/Q	368 Ω
Geometry factor, G	188 Ω
E_{peak}/E_{acc}	2.28
B_{peak}/E_{acc}	4.42 mT/(MV/m)
2 K operating goals	
Accelerating gradient, E_{acc}	17.5 MV/m
Peak surface electric field, E_{peak}	40 MV/m
Peak surface magnetic field, B_{peak}	77.5 mT
Minimum intrinsic quality factor Q_0	2×10^{10}

Through this exercise, we have arrived at a novel cavity design that bridges a hitherto unfilled gap between 'low'-β ($\beta < 0.2$) TEM-type cavities and 'high'-β ($\beta \approx 1$) elliptical-type cavities for continuous wave (CW) operation. Large, multi-cell sub-GHz elliptical cavities

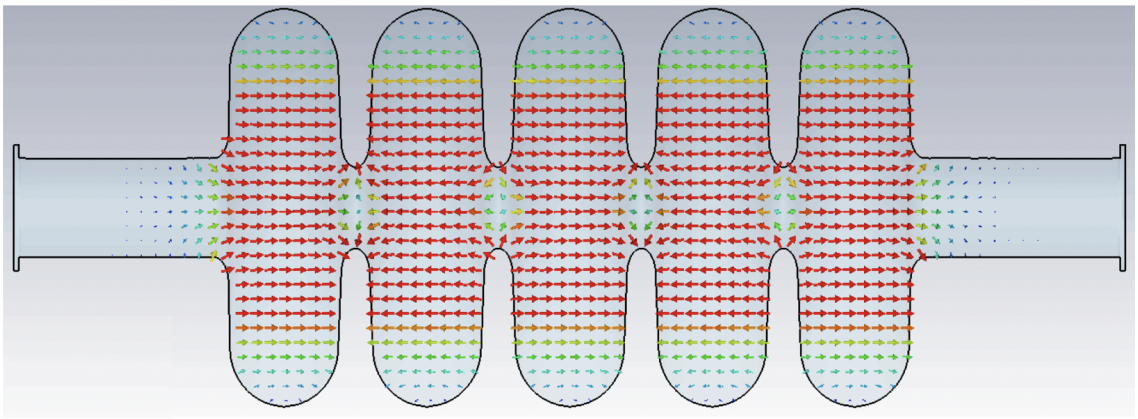

Figure 4.2: Schematic diagram of the electric (accelerating) field in the TM_{010} mode (π-mode) of the FRIB400 5-cell elliptical cavity.

have been used successfully in previous projects [49], yet FRIB's continuous-wave operation and velocity in the 'medium'-β ($\beta = 0.6$) range push this design into new territory, and set the stage for the challenges in development and processing that the rest of this work aims to address.

4.1.2 Cavity Tuning and Field Flatness Measurement

Each cell of the 5-cell cavity supports its own accelerating field along the longitudinal axis in the resonant TM_{010} mode (Figure 4.2). This mode is excited by the RF power emanating from the input coupler. It is critical for each of the five cells' frequencies, f_{0i} to be as close as possible to each other: when the TM_{010} is excited with the individual cells tuned thus, the accelerating field reaches equal magnitude from cell to cell. Achieving such "field-flatness" enables the cavity to support the maximum accelerating voltage in each accelerating gap for a minimum of the peak surface fields, which reduces RF losses and the likelihood of electrical breakdown and field emission [28]. Good field-flatness also decreases the liklihood of multi-modal excitation, in which nearby, undesirable "parasitic" modes, such as the $4\pi/5$ mode in the case of 5-cell elliptical cavities, can become excited along with the π mode.

Thus, upon receipt of the two prototype 644 MHz 5-cell elliptical cavities from Research Instruments (GmbH) at FRIB, the first order of business was to tune them. Tuning an RF cavity is an iterative process, in which the cells are mechanically squeezed or lengthened in a tuning fixture to bring their resonant frequency to pitch. A first-order perturbation theory can be applied to model the frequency excursions of out-of-tune cells, as described in [28].

In brief, it can be shown that the resonant frequency of a cavity and the stored energy of the electromagnetic fields in the cavity are related to each other by an invariant quantity (in other words, the *action* U/ω is constant). The stored energy of the cavity, U, is a volume integral over the electric (E) and magnetic (H) fields in the cavity,

$$U = \frac{1}{4}\int_V (\mu_0 H^2 + \epsilon_0 E^2) dV \tag{4.3}$$

and, it follows from the invariant relation that changes in U prompt a change in ω. In practical terms, changes the cavity volume effecting changes in the distribution of energy between the electric and magnetic fields will cause a shift in the cavity's resonant frequency:

$$\frac{\Delta\omega_0}{\omega_0} = \frac{\Delta U}{U} \tag{4.4}$$

This shift in resonant frequency restores the resonant condition of equal energy being stored in the electric and magnetic fields [29]. The eminently useful Slater perturbation theorem [29] relates this ΔV perturbation to the expected shift in resonant frequency, $\Delta\omega$:

$$\frac{\Delta\omega}{\omega_0} = \frac{\Delta U_{magnetic} - \Delta U_{electric}}{U} = \frac{\int_{\Delta V}(\mu_0 H^2 - \epsilon_0 E^2) dV}{\int_V (\mu_0 H^2 + \epsilon_0 E^2) dV} \tag{4.5}$$

In this formulation, we can see that squeezing the cavity in areas that affect regions

of high magnetic field, such as the equator, shift the resonant frequency upwards, whereas doing so in regions with high electric field, such as near the cavity iris, decreases the resonant frequency. In the case of the FRIB400 cavities, compressing the cells in the tuning fixture affects the high electric field region near the iris more than it affects the high magnetic field region near the equator, and the result is a *decrease* in resonant frequency.

Clearly the process of field-flatness tuning requires a method of measuring the cell-to-cell field strength of the cavity along the beam axis. The RF cavity community has devised a standard "bead-pull" method to accomplish this, which uses a small metallic or dielectric bead to perturb the cavity volume, and interprets the results using the Slater perturbation theorem, which, in the case of a spherical dielectric bead gives [29]

$$\frac{\Delta\omega}{\omega_0} = -\frac{3\Delta V}{4U}\frac{\epsilon_r - 1}{\epsilon_r + 2}\epsilon_0 E^2 \tag{4.6}$$

Recalling that $Q_0 \approx Q_L \approx \omega_0 U/P$, and that Q_L is measurable directly with a vector network analyzer (VNA), we thus find the stored energy, U. ΔV of the bead is easily calculable, leaving us with

$$\frac{\Delta\omega}{\omega_0} \propto E^2 \tag{4.7}$$

from which the electric field strength on-axis, E, can be determined.

Figure 4.3 shows the bead-pull test stand constructed for the FRIB400 644 MHz cavities. In this set-up, an 8mm brass bead is threaded onto nylon monofilament, and mounted on pulleys above and below the cavity in a vertical fixture, as shown in Figure 4.3A. The bottom end of the thread is attached to the stepper motor, and the top is weighted over a third pulley. Jigs attached to the beam ports ensure that the bead is drawn precisely along the center of

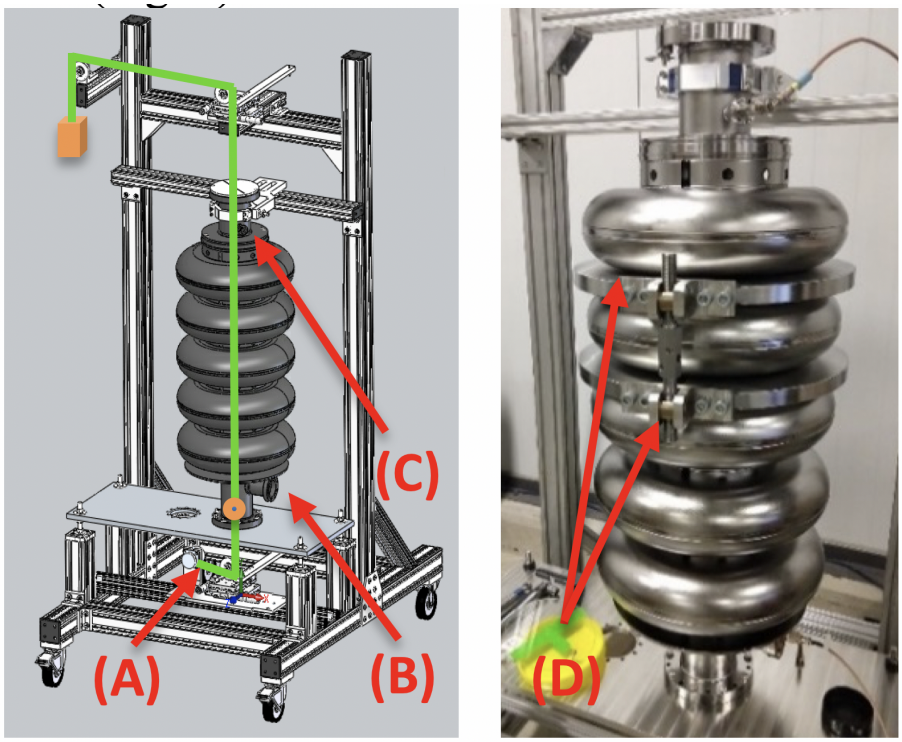

Figure 4.3: Bead-pull test stand used for the FRIB energy upgrade 644 MHz β= 0.65 elliptical cavities. The green line traces the nylon monofilament, and the orange sphere is the bead. (A) Stepper motor. (B) Input coupler. (C) Pickup coupler. (D) Cell tuning cuffs (SS304) and turnbuckle.

the beam axis. The VNA provides 10 dBm to the input coupler, and measures the change in the phase, ϕ, at the pickup port at the unperturbed π-mode frequency. Our method, adapted from [50], makes use of the relation,

$$\frac{\tan\phi}{2Q_L} = \frac{\Delta\omega}{\omega_0}, \implies \frac{\tan\phi}{2Q_L} \propto E^2 \tag{4.8}$$

which has the benefit of ϕ being an easily measurable quantity with the VNA. A Labview program was created to step the bead through the axis in small increments, and record the phase-shift data from the VNA. A MATLAB script then processed the data, calculating the relative field flatness and cell-by-cell tuning adjustments in kHz needed bring the five cell fields to 100% similarity in the π-mode [51].

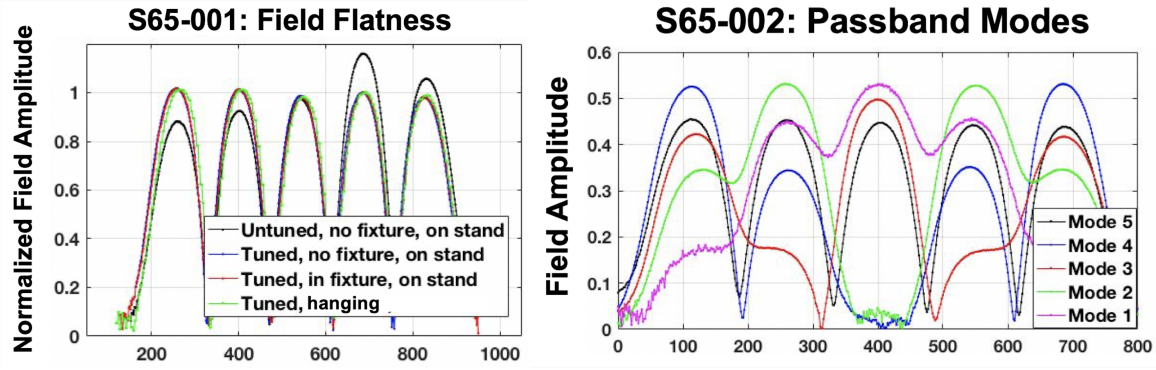

(a) (b)

Figure 4.4: (a) Comparison of untuned S65-001 without fixture (black) to the final tuning of S65-001 without fixture (blue), with fixture (red) and hanging (green) demonstrating that the vertical seating of the cavity on the bead-pull test stand does not affect the field flatness in the dunk-test (hanging) orientation. Bottom: pass-band mode field measurements. The vertical axis in both cases are in units of normalized field amplitude, the main purpose of which is to simplify the cell-to-cell comparison of cavity field.

The cell tuning apparatus consists of two stainless steel cuffs with two turnbuckles affixed 180 degrees apart (Figure 4.3 B). Results of the field-flatness tuning of S65-001 are shown in Figure 4.4, in which we achieved a final field-flatness of 97% starting from a value of 72% . S65-002 was tuned similarly and also achieved a final field-flatness of 97%, calculated from the cell fields, $1-(E_{max}-E_{min})/E_{average}$. Figure 4.4 further demonstrates that the vertical orientation of the cavity does not affect the final field flatness in the hanging orientation used in the test dewar. Furthermore, the change in resonant frequency as a function of deflection (squeezing) was measured with a dial indicator and found to be -238 +/- 16 kHz/mm, and the cavity could withstand up to 100 kHz of deflection without permanent deformation. The pass-band modes, $\pi/5$, $2\pi/5$, $3\pi/5$, and $4\pi/5$, of S65-002 were also measured and are shown in Figure 4.4.

4.1.3 Mechanical Mode Measurements

The steep sidewalls of the FRIB400 644 MHz cavity invite comparison to springy, flexible structures (such as accordion bellows), which is concerning for a couple of reasons. The first reason is intrinsic to the cavity: an operating RF cavity contains strong electromagnetic fields, which induce small electrical currents in the surface of the RF cavity, as discussed in Ch. 3. The interaction of the oscillating magnetic field with this surface current produces an interesting, though problematic, instance of the familiar Lorentz force F_L, i.e., $F_L = E \times B$, in which the cavity sidewalls near the irises are pushed inward and the equator is forced outward [28]. As discussed at length, changes in cavity volume ΔV affect change in cavity frequency, $\Delta\omega$, and in this case, it is proportional to the strength of the cavity field, near a few $Hz/(MV/m)^2$ [28],

$$\delta\omega \propto (\epsilon_0 E^2 - \mu_0 H^2)\Delta V. \tag{4.9}$$

Unfortunately, alterations to the cavity frequency affect how well-coupled the cavity is to the driving RF power, which in turn affects the strength of the cavity field. This coupling between cavity mechanical modes and RF modes can lead to ponderomotive oscillations and instabilities, which must be controlled for [52]. The beam-loading of the cavity can exacerbate this issue further [28].

The second concern is extrinsic to the cavity-RF power system. Cryomodules are notoriously noisy environments, beset with microphonics generally on the order of a few tens to hundreds of hertz, usually propagating from the cryogenic and other supporting systems. Microphonic resonances inconveniently coupling the cavity to its environment can also perturb the cavity's resonant frequency, in the worst case, outside the bandwidth of the cavity's

resonance control system (low-level rf) [52] [53]. Recall, the relatively high quality factor of the 644 MHz cavities means they have a narrower bandwidth.

The steep sidewalls of the FRIB upgrade cavity make it particularly susceptible to an 'accordion' or longitudinal mode compared to the TESLA cavity shape, whose sidewalls are much less steep, forming a more rigid cell. Mechanically stiffening the cavity is the first line of defense against these undesirable mechanical susceptibilities, and stiffening rings are an integral part of the FRIB400 644 MHz cavity design. Still, mechanical eigenmodes exist, and the purpose of this stage of the investigation was to find and characterize the strength of any concerning mechanical modes of the cavity that might be sensitive during operation at 644 MHz.

Mechanical simulations of the FRIB400 cavities predicted transverse cavity modes at 72 and 91 Hz, the cavity 'accordion' mode at 94 Hz, and the cavity twist mode at 123 Hz [48]. The accordion mode is expected to be the dominant mechanical mode, strongly coupled to the 644 MHz operating frequency. Usually, cavity mechanical modes are characterized in cold tests with helium-jacketed cavities equipped with tuners and with means by which to measure the Lorentz transfer function. However, the novelty of the 644 MHz cavity makes this an interesting exercise even at room-temperature in an undressed cavity bench-test, since this still allows us to determine the cavity's natural damping of the accordion mode at the earliest possible stage in the cavity's development [54].

The undressed cavity was fitted with two adjustable but rigid stainless steel bars clamped to the ends of the cavity, as shown in Figure 4.5, effectively pinning the ends as if a helium jacket were present, against cavity displacement in the longitudinal direction. Of note, this may cause the transverse and twist modes to have exaggerated amplitudes since the frame does not provide the same stiffness against bending or torsion as the real helium jacket,

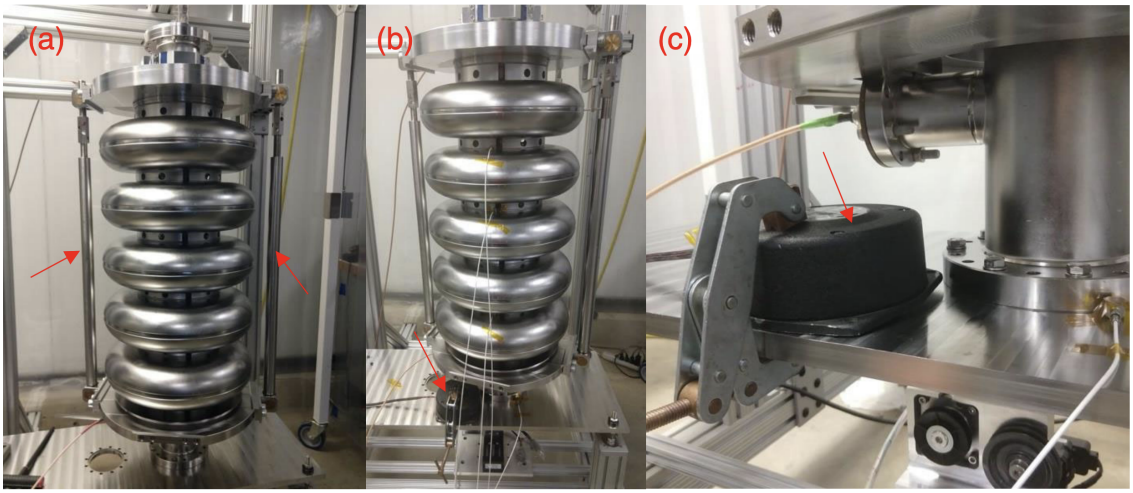

Figure 4.5: (a) 644 MHz cavity assembled with the rigid steel bars (arrows) clamped to the ends of the cavity to mimic the presence of the helium jacket. (b) Cavity assembled on the bead-pull test stand with the mechanical speaker (arrow) in place, with accelerometers (white cables) attached to the cell equators. (c) details of the mechanical speaker coupled to the cavity test stand.

however, these modes are not particularly interesting modes in this measurement since they are not strongly coupled to the RF frequency.

To look for the cavity mechanical modes, a mechanical speaker was clamped to the cavity test stand (Figure 4.5) and driven with a sine wave, scanning a range in frequency from 0 to 200 Hz. 200 Hz was chosen as a maximum based on prior experience with the FRIB linac cryomodules in which we found that extant external mechanical disturbances to the cavity from the linac supporting systems are within several tens of Hz [54]. Furthermore, the highly concerning accordion mode appeared in simulations around 95 Hz, which is well-bounded by the 0-200 Hz scan [48].

While the cavity was being mechanically scanned by the speaker, we excited the accelerating TM_{010} mode, and measured the sidebands of that resonance on a real-time spectrum analyzer (RTSA), which has a 0.1 Hz minimum resolution bandwidth. During the scan, the dominant mechanical resonance coupled to the RF mode appeared at 96 Hz as shown in Fig-

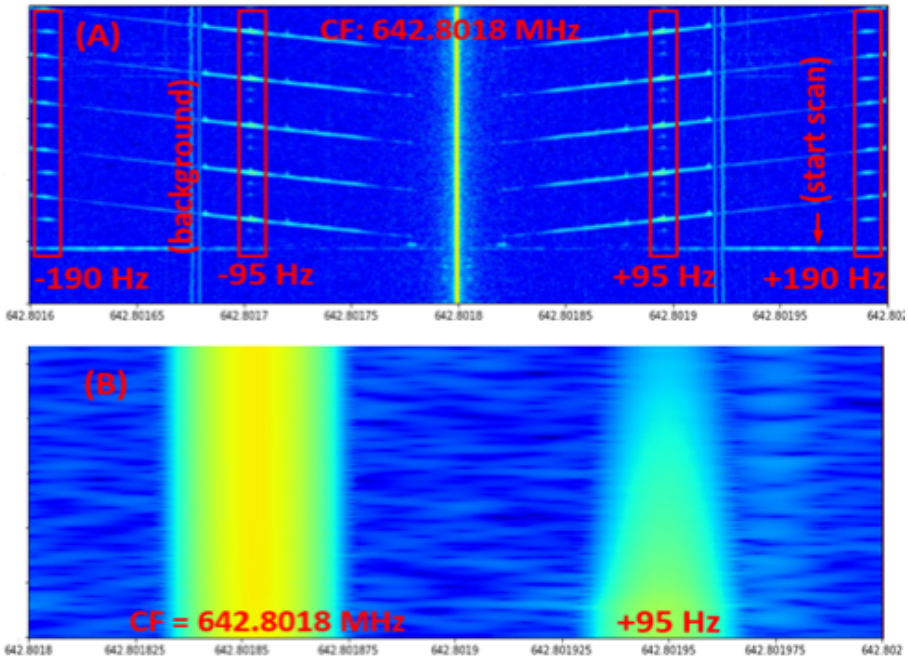

Figure 4.6: (A) Spectrograph of the S65-002 30sec mechanical mode scans. The 95 Hz accordion mode and its first harmonic at 190 Hz are apparent, marked in red. (B) Decay time measurement. Center frequency to the left, sideband decay to the right.

ure 4.6, consistent with the mechanical simulation's predictions. The response of this mode in the bench-test was at least 15 dB stronger than any other mode. As further confirmation that this indeed was the cavity's accordion mode, accelerometers attached to a subset of the cavity cells showed sinusoidal oscillations with a phase advance per cell as shown in Figure **??**, which is roughly consistent with the predicted accordion mode [48] [54].

To determine the cavity's natural damping of this mode (i.e., the mechanical mode's quality factor, Q_m), we drove the cavity at resonance, then excited the 95 Hz sideband to a steady state with the mechanical speaker. The speaker was then switched off, and the decay time of the sideband, which is caused by the mechanical mode and thus has the same decay time constant, was recorded by the RTSA (Figure 4.6). The relationship between the RF sideband decay time and the mechanical mode Q_m was derived as follows: when the accordion mode is excited with the displacement amplitude Δx, the RF resonant frequency

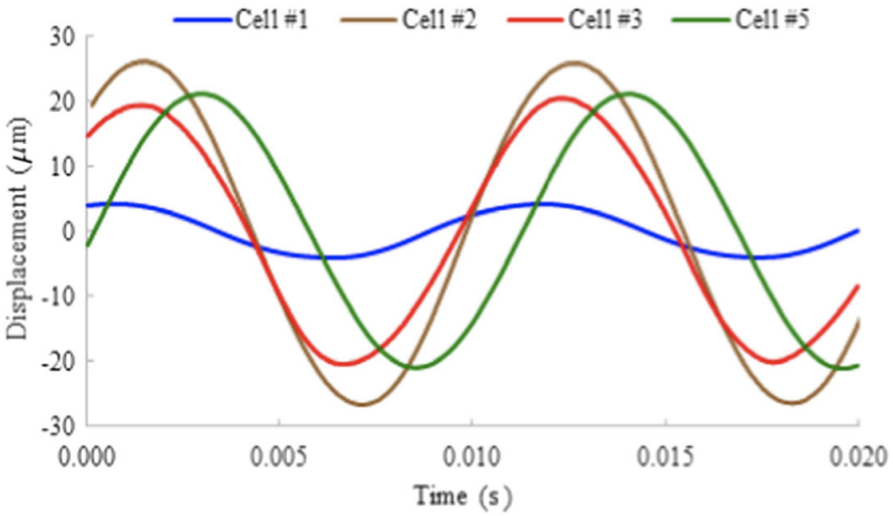

Figure 4.7: Displacement oscillations at the 95 Hz mechanical mode. These are measured from the accelerometers attached on the equators and aligned to the cavity axis (longitudinal direction). The phase advances are 28° from Cell No. 1 to Cell No. 2, -4° from Cell No. 2 to Cell No. 3, 52° from Cell No. 3 to Cell No. 5 [44].

oscillates with the frequency excursion amplitude Δf, which results in the phase modulation with amplitude $\Delta\phi$ in the RF circuit. The mechanical displacement is much smaller than the cavity size, thus we can state $\Delta f \propto \Delta x$. The frequency excursion is much smaller than the room temperature cavity RF bandwidth, thus $\Delta\phi \propto \Delta f$ and $\Delta\phi << 1$ The first sideband power is proportional to $J_1^2(\Delta\phi)$, where $J_1(x)$ is the first-order Bessel function with argument x. Since $\Delta\phi << 1$, the sideband power is approximately equal to $\Delta\phi^2$ and thus is proportional to Δx^2. Therefore, the decay time of the RF sideband power is the same as the decay time of the mechanical oscillation and the mechanical mode Q_m is then

$$Q_m = \omega_m \tau_{SB}, \tag{4.10}$$

where ω_m is the modulation frequency and τ_{SB} is the exponential decay time of the first RF sideband power [44].

The measured decay time is -14 dB/sec as shown in Figure **??** which yields the mechanical

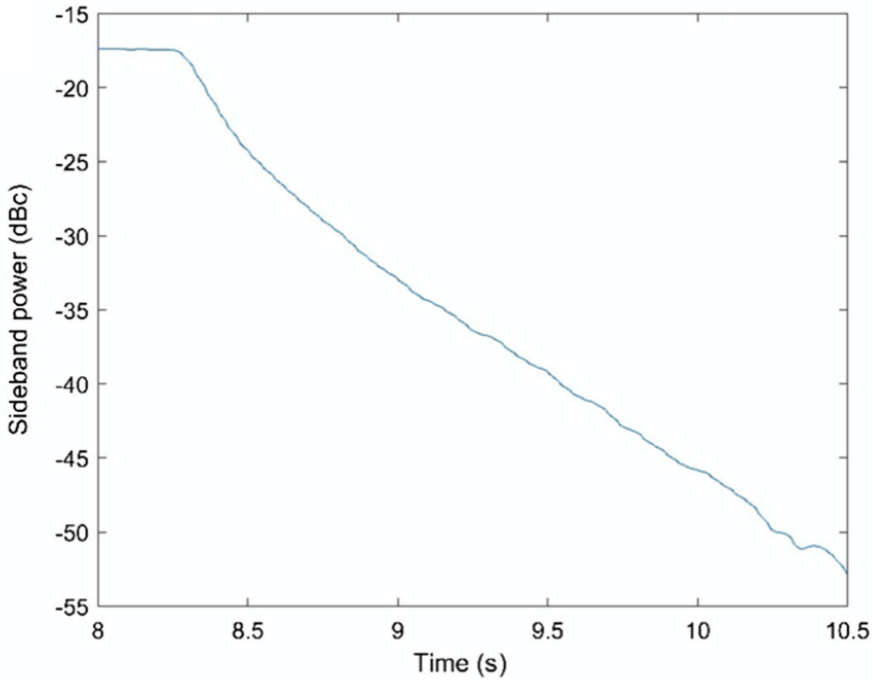

Figure 4.8: The decay curve measured at 95 Hz. The decay rate of the mechanical mode energy is -14 dB/s. [44].

Q of 185. This mechanical mode Q is no higher than that in 1.3 GHz TESLA cavities or FRIB $\beta_{opt} = 0.53$ 322 MHz half-wave resonators [55] [56]. We therefore, by comparison, conclude that the coupling between the mechanical accordion mode and the RF cavity resonant mode in the 5-cell 644 MHz $\beta = 0.6$ cavities is weak enough to not be a significant cause of cavity field instabilities during accelerator operation.

4.2 Surface processing

While the results of the mechanical and tuning studies described above are encouraging, the RF performance remains the ultimate test of the new cavity design. To wit, before sophisticated high-Q_0 development can be pursued in the 644 MHz $\beta = 0.6$ cavities, we must first demonstrate that reasonable Q_0 and cavity RF performance can be achieved with

one or more well-known, industry-standard RF surface processing techniques. If the cavity RF performance were to fail spectacularly at this point, a substantial re-design would be needed, not high-Q_0 studies.

The goal of cavity surface processing is to remove the damage layer formed during cavity fabrication, then prepare a clean, smooth, defect- and particulate- free cavity surface within the RF penetration layer that supports high-Q (low surface resistance) and high-gradient performance. Cleanliness and smoothness on a microscopic scale are critically important given the high internal fields the cavity operates at. Any sharp edge or particle in a high-electric field region can cause electron emission and produce x-rays, degrading cavity performance by bleeding RF power, causing excess heating, and damaging nearby electronic equipment, in a process known as emission, which shall be discussed in depth in a later section.

As mentioned in the introductory chapters, RF surface resistance, R_S, is inversely related to the cavity's intrinsic quality factor Q_0 via the cavity's geometry factor, G. R_S can be broken into temperature-dependent and temperature-independent portions, and RF surface processing treatments generally affect one or both of these to differing degrees. The ultimate selection of an RF treatment must consider the cavity's intended operating conditions, and whether the temperature-dependent Matthis-Bardeen resistance (R_{BCS}, the temperature-independent residual resistance (R_0), or some combination of both, is likely to be most limiting at its given operating gradient, temperature, and required Q_0.

Due to this high degree of sensitivity to surface contamination, cavity surface processing and assembly becomes challenging to optimize control to a repeatable level, particularly at the scale of a large production run. Even the most ideally-prepared high-Q treatment of a cavity can be stymied by poor cavity handling and assembly, or by imperfect high-pressure water-rinsing steps. Thus successful cavity surface preparation depends both on

the fundamental physical details of the prepared RF surface, which we manipulate with various chemical treatments, baking procedures, etc., and the repeatability of the cavity cleaning and assembly steps conducted in the high-grade clean-room environment. The large size of the FRIB400 cavity makes the above processes even harder to control. The large inner surface area increases the statistical likelihood of particulate contamination, and the steep sidewalls make flow-dependent processes such as high-pressure water rinsing, or chemical etching/polishing, precarious. Temperature control also becomes more challenging as a function of the cavity size.

Techniques for processing SRF cavity surfaces have matured, in the span of a few decades, over a wide range of operating frequencies and particle velocities. With the inertia provided by a long history in the literature, and with many applications worldwide, the high-β 1.3 GHz TESLA cavities have been the testbed of choice for investigations of novel, high-gradient and high-Q_0 surface processing treatments [57]. In these cavities, electropolishing (EP) [58] [59], became the basis of the "standard ILC" treatment developed for the high-β cavities for the International Linear Collider [60]. In the context of the mass-production of over 800 EP cavities for the European X-ray Free Energy Electron Laser, good industrial process control was demonstrated over EP, resulting in the average cavity gradient for this production run exceeding specifications by 25% [61]. The performance of EP-treated low-β cavities has also been well-developed, resulting in gradients and Q-factors approaching those of leading EP-treated TESLA cavities [62]. In addition to having this strong track-record, EP is also an integral part of the nitrogen-doping treatment, an advanced technique we plan to investigate in the high-Q development for the FRIB400 cavity. Establishing good baseline EP parameters and performance in the FRIB400 prototype cavities is an important component of this first phase of testing.

The ease and relative economy of the buffered chemical polishing (BCP) treatment make it an important conventional process to consider as well. BCP has been well-developed in low-β cavities, and, of particular relevance, BCP conducted in-house in the MSU SRF facilities successfully delivered over 300 $\beta = 0.04$ to $\beta = 0.53$ quarter- and half-wave resonators for the FRIB baseline linac, which met or exceeded all baseline performance specifications [63] [64]. BCP in medium-β also has something of an industrial history: In the sub-GHz elliptical cavities for the Spallation Neutron Source (SNS) and the European Spallation Source (ESS), BCP was used to meet both sets of machine specifications (Q_0 of 5×10^9 at E_{acc} of 10.1 MV/m for SNS' $\beta = 0.61$ cavities, and $Q_0 > 5 \times 10^9$ at E_{acc} of 16.7 MV/m for ESS' $\beta = 0.67$ cavities)[65] [49]. However, as pulsed machines, these Q_0 requirements are around an order of magnitude less than the minimum design goal Q_0 of FRIB400, and even at this stage it seems somewhat unlikely that BCP will deliver the needed Q_0 for a CW machine.

The following subsections provide a brief introduction to EP, BCP, and the 120°C baking treatments used in the first high-power RF tests of the 5-cell FRIB400 prototypes.

4.2.1 Electropolishing

In a basic EP treatment for niobium, the elliptical Nb cavity is partially filled with an electrolyte, commonly, a 9:1 mixture of sulfuric acid (H_2SO_4) and hydrogen fluoride (HF). An electrode (the cathode) is inserted into the cavity and a voltage is applied between it and the cavity surface (the anode), currently between 18 and 23 V at the Argonne EP facilities used throughout this work [66]. The electric potential between the cathode and the cavity surface drives an exothermic, electrolytic reaction in which the thin niobium-oxide layer on the cavity surface and the HF in solution react to form a thin, viscous layer of soluble niobium salts [66]. At microscopic scale, the sharp peaks of a rough niobium surface poke into this

resistive layer of reactants, and concentrate the electric field. The higher electrical gradient in these peak areas drive faster Nb-consuming reactions, meaning a leveling effect is achieved, under what is effectively a Nernst diffusion layer [67], wearing down these peaks and, if the EP parameters are ideally controlled, resulting in a micron-smooth surface [66]. From a chemical standpoint, the key rate-limiting factor to ideal EP appears to be the diffusion rate of the fluoride ions towards the cavity surface [67], however multiple EP parameters can strongly affect this diffusion, and other competing chemical processes occurring at the cavity surface. A high temperature, for example, has been shown to drive an alternative etching process which is sensitive to differently-orientated grains in the niobium surface, resulting in irregular grain-wise polishing [67].

Recent EP studies have confirmed the empirically observed benefit of so-called "cold EP," in which the last few tens of microns of EP is conducted at a temperature of 15-17°C or less, resulting in a smoother EP surface [68]. Unless otherwise noted, all EP treatments applied in the subsequent studies incorporate this Cold EP as part of the EP treatment. The benefit of this Cold EP treatment appears to have a stronger role in retarding damaging gas bubble evolution in N-doped cavities, as opposed to in non-doped cavities, for reasons that are not yet entirely clear [68]. However, since the process appears to be of moderate to strong benefit to all cavity types, we elected to apply it to the FRIB400 cavity EP processing.

4.2.1.1 EP Tooling Modification

Electropolishing 644-650 MHz medium-β cavities was anticipated to be particularly challenging due to the high aspect ratio of of the cavities' cell length to cell width [69]. The iris-to-iris distance of the FRIB400 cavities is 142 mm, whereas the equator radius is 197 mm, making for an aspect ratio of nearly 1.39, whereas the more typically electropolished

1.3 GHz cavities have an aspect ratio of only 0.91. These cavities' equators' greater stand-off distance from the central axis incurs greater electrolytic resistance in the EP process due to the greater volume (i.e., greater linear distance) between the EP electrode and the cavity surface. This in turn varies the surface current applied the cavity undergoing EP as a function of linear distance travelled along the cavity's central (longitudinal) axis, raising the concern of non-uniform removal. Preliminary studies in electropolishing the prototype $\beta = 0.6$ 650 MHz cavities for the PIP-II accelerator suggested several modifications to the electrode [69], attempting to counteract this effect. These modifications were then adopted by our collaborators at Argonne National Laboratory (ANL) to develop the EP technique ultimately used in electropolishing the FRIB400 cavities [44].

First, particular care must be taken with regard to temperature control of the cavity surface and acid bath during the EP process [69]. Recall, electrolytic reaction is an exothermic one, and the removal rate increases as a function of processing temperature. Thus, it is critical to stably control surface temperature across the entire surface of the cavity to ensure uniform removal. The challenge of temperature control necessarily scales with cavity size, with the $\beta = 0.6$ 5-cell elliptical cavities being among the largest-dimensioned elliptical cavities upon which electropolishing has been attempted thusfar. In the case of these large cavities, ANL removes heat from the cavity surface by cooling the acid bath, and pumping chilled water over the cavity exterior. To monitor and control the exterior cavity surface temperature, ANL installed eight thermocouples placed as follows: one on each beam tube, at each equator, and one additional sensor on a cavity iris. In the case of the single-cell versions of the FRIB400 prototypes, the eight thermocouples were placed on each beam tube, on each iris, halfway up each sidewall, and on either side of the equator weld.

As in conventional EP treatments, the FRIB400 cavity was partially filled with acid to

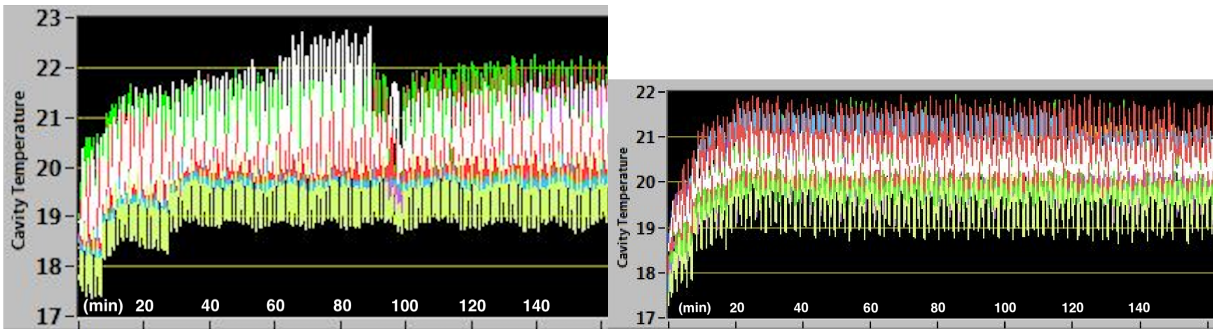

(a) (b)

Figure 4.9: (a) Single-cell FRIB400 cavity surface temperature time-series plot during an EP treatment, including the final stages (left) of "Cold EP." The upper and lower bounds of the temperature values correspond to the thermocouple rotating into and out of the acid bath. Note the lower limit of this oscillation is well-controlled within +/- 0.5 degrees C of the target EP temperature values. (b) 5-cell FRIB400 cavity surface temperature time-series plot during an EP treatment, including the final stages (left) of "Cold EP."

just above the cavity midpoint. This acid is pumped through the cavity at a flow rate of approximately 2 gallons per minute (gpm). With water cooling, ANL demonstrated good control of the cavity surface temperature within its natural cyclical variation of approximately +/- 1.5°C of the target temperature, as the monitors rotate into and out of the acid bath. Importantly, the minma of this cyclic vary by under half a degree per cycle, demonstrating stable temperature control throughout the process, as seen in Figure 4.9.

To improve the electrode-to-cavity surface area ratio closer to the 10:1 'rule of thumb' [69], aluminum 'doughnuts' were fabricated and fitted to the electrode, shown in Figure 4.10. Teflon masking was applied at the longitudinal position of the cavity beam pipes and the cavity irises. These modifications to the EP process were then validated with several ultrasonic (US) thickness measurements along the cavities' surfaces, taken before and after bulk (150 μm) EP processing. The configuration of the stiffening rings on the 5-cell cavity limit thickness measurements to the equator regions and beam pipes, as indicated in Figure 4.10. Measurements at these points showed an average of 149 μm of removal across all

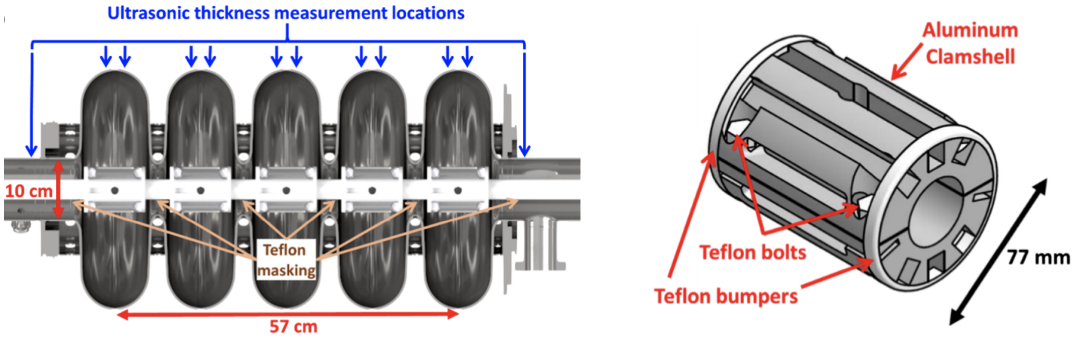

(a) (b)

Figure 4.10: (a) EP cathode integrated with the cavity. The doughnuts can be seen mounted on the cathode at the equator locations and Teflon shielding at the iris locations. Red arrows indicate the locations for ultrasonic thickness measurements. (b) Close-up image of the aluminum doughnuts fabricated for the EP electrode.

equator positions, with a standard deviation of 6 μm, and 199 μm of removal from the beam-pipe positions. The greater removal from the pipe regions is the expected result of the cavity surface's closer proximity to the electrode in those regions, and, as long as the removal is not too excessive, is not of concern since this region is not of high functional relevance to cavity RF performance.

The fabrication of a single-cell cavity enabled a more detailed mapping of material removal across the cavity surface after bulk EP. Using a single-cell version of the modified EP electrode, a 160 μm bulk EP was conducted, then US-measured at twenty different measurement points along the cavity surface, shown in Figure 4.11. An average of 160 μm of removal was attained, with a standard deviation of 6 μm, with no major systematic differences in removal amounts between the cavity equator and sidewalls. As in the 5-cell case, the greater removal on the beam pipe region is expected, and of no significant concern.

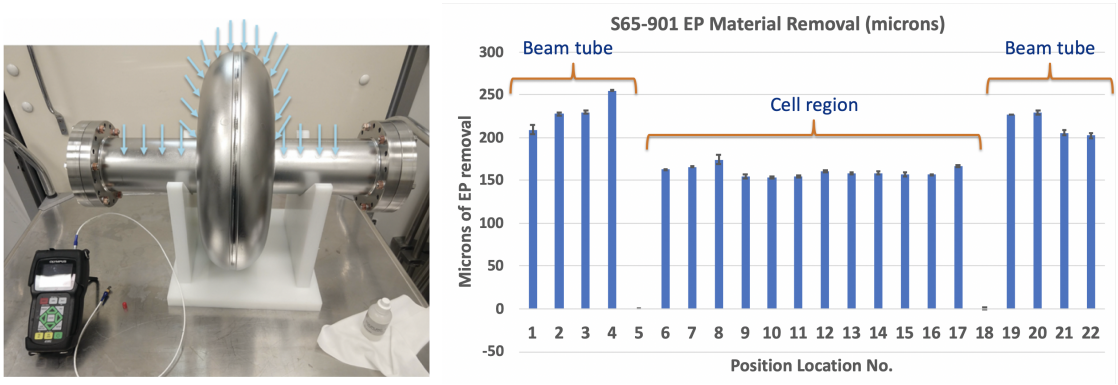

(a) (b)

Figure 4.11: (a) Image of the prototype FRIB 644 MHz β opt = 0.65 single cell cavity, with blue arrows indicating the 20 used ultrasonic thickness measurement locations across the cavity surface. (b) Microns (μm) of removal, with measurement error, showing an average removal in the cell region of 160 m with a standard deviation of approximately 6 μm. No significant deviation exists between the material removal from the near-vertical sidewalls (positions 6-10, 13-17) and the cavity equator (position 11-12). Positions 5 and 18 encroached upon the high-curvature region near the cavity iris and the ultrasonic thickness measurement tool could not produce accurate readings.

4.2.2 Buffered chemical polishing

Buffered chemical polishing (BCP) is similar to EP in that it consists of a chemical etch, however, unlike EP, no electric field is applied to drive the reaction preferentially at high-point areas on the cavity surface. In the course of BCP, differential etching as a function of niobium grain orientation occurs, and, as a result, BCP generally yields a surface roughness nearly an order of magnitude higher than that of EP [70]. Further, Q_0 in BCP cavities was found to dip significantly at high gradient, an effect dubbed the 'high-field Q-slope' (HFQS). This was later found to be ameliorated by 120°C baking, as explained in the next section.

The BCP treatment chosen for the FRIB400 cavity was identical to that used to successfully deliver the FRIB baseline quarter-wave and half-wave resonators: a '1:1:2' solution, consisting of 1 part HF acid, 1 part Nitric acid, and 2 parts phosphoric acid [71]. Again, the size of the FRIB400 cavity makes the application of BCP technically challenging. Effective

cooling of the cavity surface and adequate flow rate of the chemical mixture are required to avoid the formation of nitrogen dioxide bubbles on the cavity surfaces during BCP [66].

BCP of the FRIB400 prototype cavity was conducted with the cavity in the vertical orientation, which is the only configuration that fit into the existing BCP fixture at FRIB. No additional cooling was applied beyond that which was provided by the acid itself. After the BCP treatment, pitting was observed on one of the sets of sidewalls throughout the cavity. This set of cavity sidewalls would have been the "upper" set in one of the orientations in which the cavity was polished, leading to the suspicion that BCP conditions had changed for a time, leading to gas bubble trapping on the upper sides of the cavity cells. Upon review, it was found that the batch of acid was changed out partway through the procedure, and that it was possible that the fresh acid etch generated more heat than could be successfully managed by the acid cooling, leading to bubble formation. Since the Q_0 achieved by BCP for SNS and ESS is nearly an order of magnitude lower than the FRIB400 goal, it is unlikely for BCP to become the production recipe for the FRIB400 cavities. Though, this episode illustrates that additional cooling measures, and possibly a larger BCP cabinet allowing a horizontal orientation of the cavity under treatment, ought to be developed if large-size cavities such as these are to be processed for other projects at FRIB in the future.

4.2.3 120°C Baking

"Low-temperature baking" or, 120°C baking emerged as an empirical cure for the high-field Q-slope (HFQS) in niobium cavities [72] [73]. Low-temperature baking is conducted *in situ* after the cavity is assembled to the test fixture, under vacuum. The cavity is then heated to 120°C and maintained at this temperature for 48 hours. Both EP and BCP cavities have been found to benefit from this treatment, although the mechanism leading to

this benefit is not well understood [74]. Studies have found that the hydrogen content of the cavity niobium is greatly reduced in low-temperature baked cavities [73], though how the presence of hydrogen directly leads to Q-degradation at high fields is not well-defined, although some suggest it could be related to vortex-impurity dynamics [74]. Romanenko et al. [75] employed sequential HF rinses in order to determine the relevant length scale of the 120°C baking effect, finding that, in 1.3 GHz cavities, the high-field Q-slope reappeared after about 100 μm of niobium material removal [76]. While not able to propose an exact mechanism based on this result alone, the authors plausibly suggest that the presence of small niobium-hydride groups may be responsible. To wit, prior to low-temperature baking, and despite hydrogen degassing, the first tens of microns comprising the RF penetration layer remain relatively hydrogen-rich, with some population of vacancy-hydrogen complexes formed [75] [77]. Upon cooldown, these hydrogen-vacancy complexes provide nucleation cites for niobium-hydrides, which are superconducting by the proximity effect, but, at critical RF fields below that of pure niobium, are driven out of this superconducting regime and begin to strongly degrade Q, creating the HFQS [77]. The notion is that the low-temperature bake eliminates the vacancy-hydrogen complexes, thereby eliminating the niobium-hydride nucleation sites and thus eliminating the HFQS[77].

120°C was conducted at FRIB with the FRIB400 cavities assembled to their test inserts. After the cavity was under vacuum, heat tape was installed as shown in Figure 5.10 a, and monitored with Cernox temperature sensors throughout treatment. The controllers for the heat tape were set for 120°C, and aluminum foil was installed to maintain the the cavity heat environment. After approximately 48 hours, the aluminum foil and heat tape were removed, and the cavity was allowed to return to room temperature. Without further processing, and without further disassembly/reassembly, the cavities were inserted into the

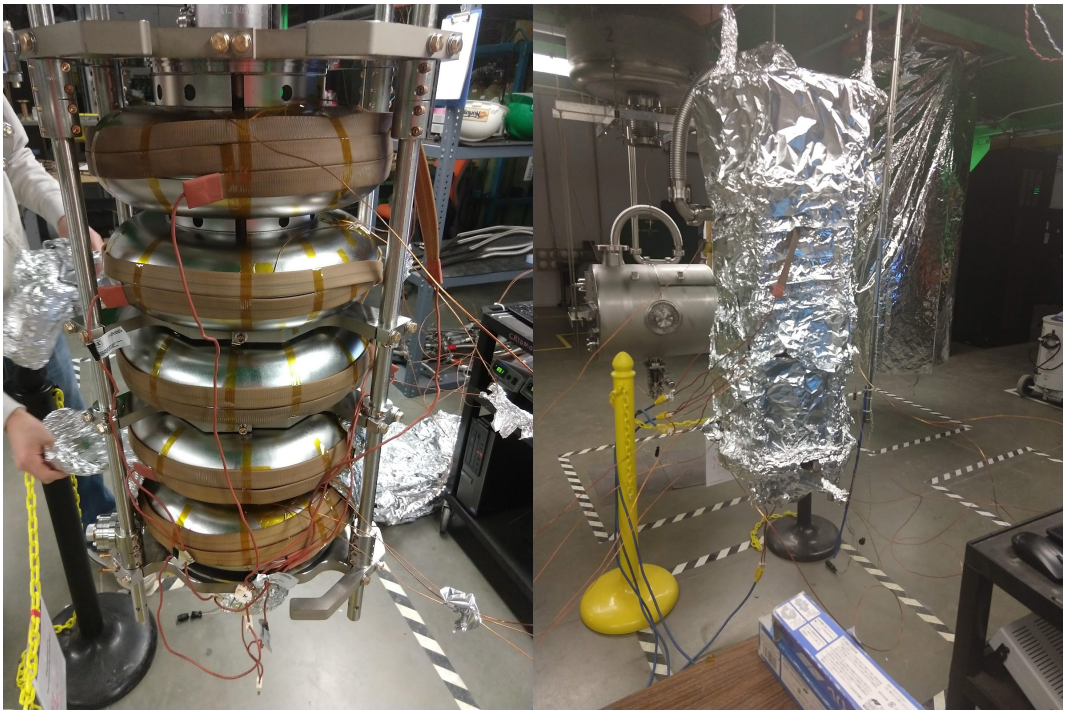

(a) (b)

Figure 4.12: (a) Image of the FRIB400 prototype cavity with heat tape installed for the purposes of conducting a low-temperature (120°C) *in situ* bake for 48 h. (b) Image of the cavity during *in situ* baking, with aluminum foil installed for heat retention.

vertical testing dewar. Since no part of the 120°C baking process takes place before the final clean assembly, it is worth noting that this particular treatment does not carry with it the risk of cavity particulate contamination.

4.2.4 Prototype Surface Treatments

The initial surface treatment of the first prototype cavity, S65-001, was based on the "standard ILC" recipe for EP, with a modified hydrogen degassing step [60]. After receipt of the cavity from the vendor, it underwent the aforementioned 150 μm bulk EP at Argonne National Laboratory (ANL), with the modified electrode, resulting in an average of 199 μm of removal from the beam pipes and an average of 149μm from the equatorial regions. S65-001 was then vacuum-baked for hydrogen degassing, first at 350°C for 12 h, then at 600°C for 10 h. The cavity was then tuned, as described, to 97% field-flatness, and shipped back to ANL for a final 20 μm EP, high-pressure water rinsing and clean assembly. S65-001 was then baked at 120°C for 48 h *in situ*, i.e., assembled to the dunk-test insert and under vacuum, then high-power RF tested. This is, henceforth, the 'EP+baking' trial.

For the 'EP-only' trial, S65-001 was "reset" with 40 μm of EP at ANL, with the last 10 μm being"cold-EP" performed at 15-17°C [68]. The cavity was then returned to FRIB, where high-pressure water rinsing and clean assembly was conducted in FRIB cleanroom facilities. The HPR device [78] consists of a robotic wand that at this time was optimized for the baseline production of the half-wave and quarter-wave resonators, which have much different internal geometries from the large, axisymmetric 644 MHz 5-cell elliptical cavities.

The second prototype, S65-002, underwent a 120 μm BCP etch, followed by 600°C hydrogen degassing, then another 20 μm BCP etch, all conducted at FRIB facilities. This cavity was then *in situ* baked at 120°C for 48 h, and high-power RF tested as the 'BCP+baking'

trial.

4.3 First vertical test RF results

All vertical tests were conducted at the FRIB vertical testing facilities, whose methods are discussed in detail both earlier in this work, and in [30].

The 2 K Q-curves (Q_0 vs. accelerating gradient, E_{acc}) for the EP+baking and EP-only trials are shown in Figure 4.14

In the first high-power RF testing of the FRIB400 prototype cavity design, the EP-only trial achieved a Q_0 of 2.3×10^{10} at the operating gradient, 17.5 MV/m, which exceeds the design goal of Q_0 of 2×10^{10} by 15% at that operating gradient. The cavity reached a maximum gradient of 26.1 MV/m, which was limited by the amplifier power available within the FRIB vertical testing facility. Still, the available RF power was sufficient to reach the gradient of apparent onset of the high-field Q-slope, around 23 MV/m. X-ray detection beginning at a gradient of around 25 MV/m and gradually increasing with power indicates the presence of mild field-emission (FE). However, the rate of x-ray emission remained below the threshold at which field-emission induced Q-degradation occurs [79]. The observed Q-drop above 23 MV/m is thus taken to be the result of the RF properties of the cavity, and not due to the presence of field-emitting particulate contaminants.

The EP-only trial exceeded the performance of the EP+baking trial, which achieved a Q_0 of 1.9×10^{10} at 17.5 MV/m. X-rays characteristic of FE again appeared, this time around 10 MV/m, and were strong enough to significantly limit the amplifier power available for the test, and thus the cavity gradient was ultimately limited to 17.5 MV/m. Both instances of field emission are believed to be the result of suboptimal configuration of the HPR system

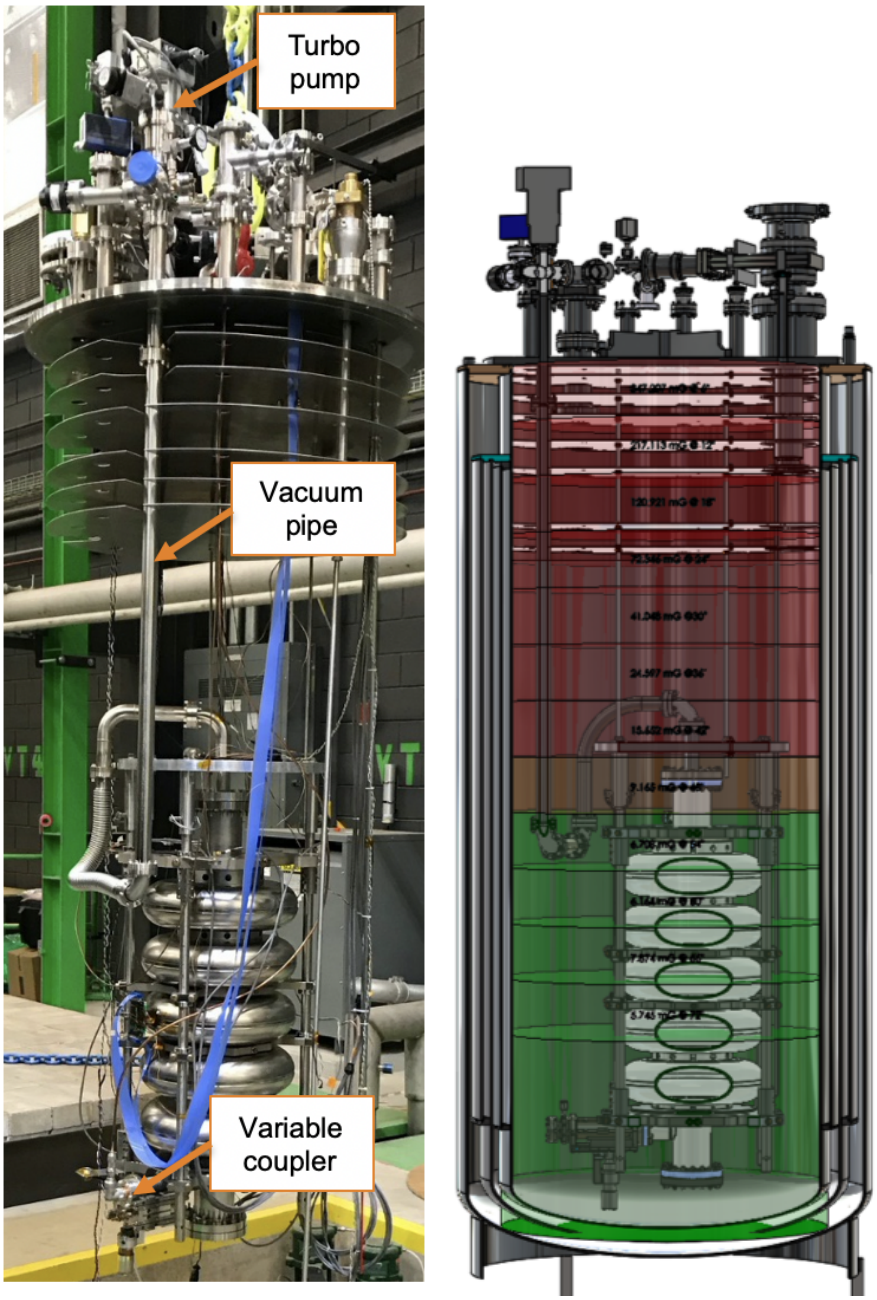

(a) (b)

Figure 4.13: (a) FRIB400 cavity assembled to the dewar insert at the MSU/FRIB test facilities. (b) Solidworks diagram of the cavity insert installed in the MSU/FRIB vertical testing dewar.

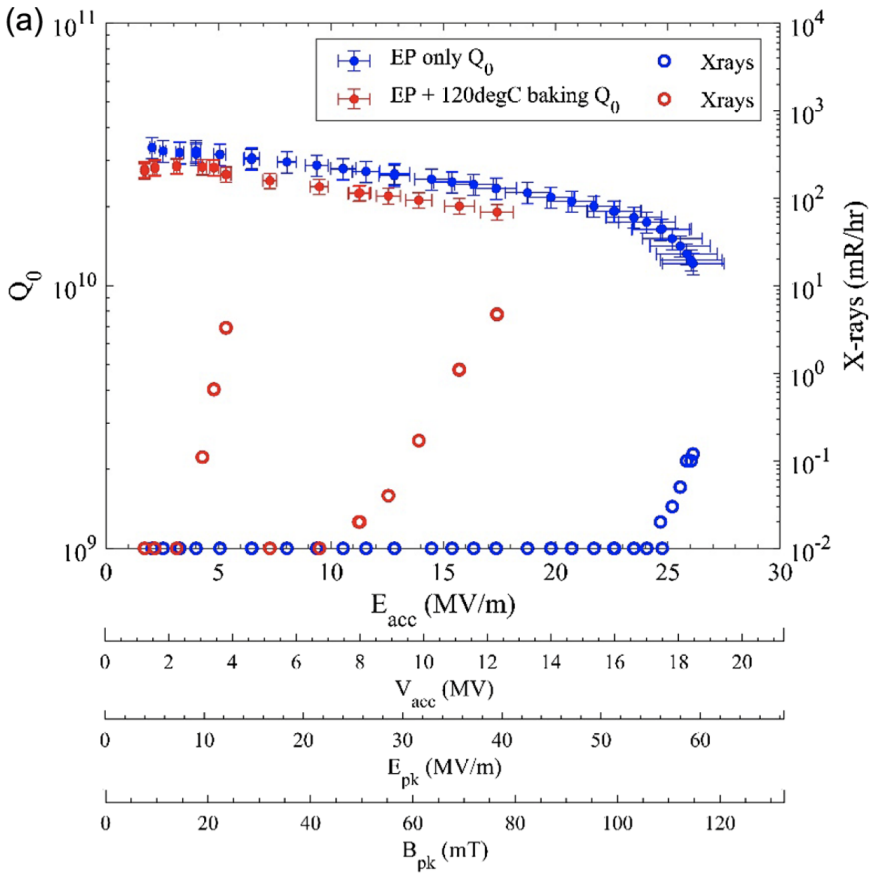

Figure 4.14: 2 K Q curves comparing EP only vs EP + 120°C baking recipes in S65-001. The blue circles are the EP-only case and the red circles are the EP + 120°C baking case. The open circles are field-emission X-rays, as read on the right-hand vertical scale. In all trials FE remained well below 100 mR/h. Noticeable degradation in Q_0 due to FE occurs at 100 mR/h and above [79] [44]. For the readers' interest, multiple conversions of the cavity field units are provided.

at FRIB, as shall be addressed in the next section.

From Figure 4.14, the effect of the 120°C baking appears to have slightly lowered the overall Q_0, but it is difficult to glean more detail from the Q_0 vs E_{acc} scheme. By employing the relation between the cavity geometry factor G and RF surface resistance, R_S, $R_S = G/Q_0$, the data in Figure 4.14 may be replotted in terms of the RF surface resistance vs. cavity field. Though $R_S = G/Q_0$ is a field-independent expression for R_s, it is an applicable relation in this context [80]. This refactoring of the data appears in Figure **??**, where the x-

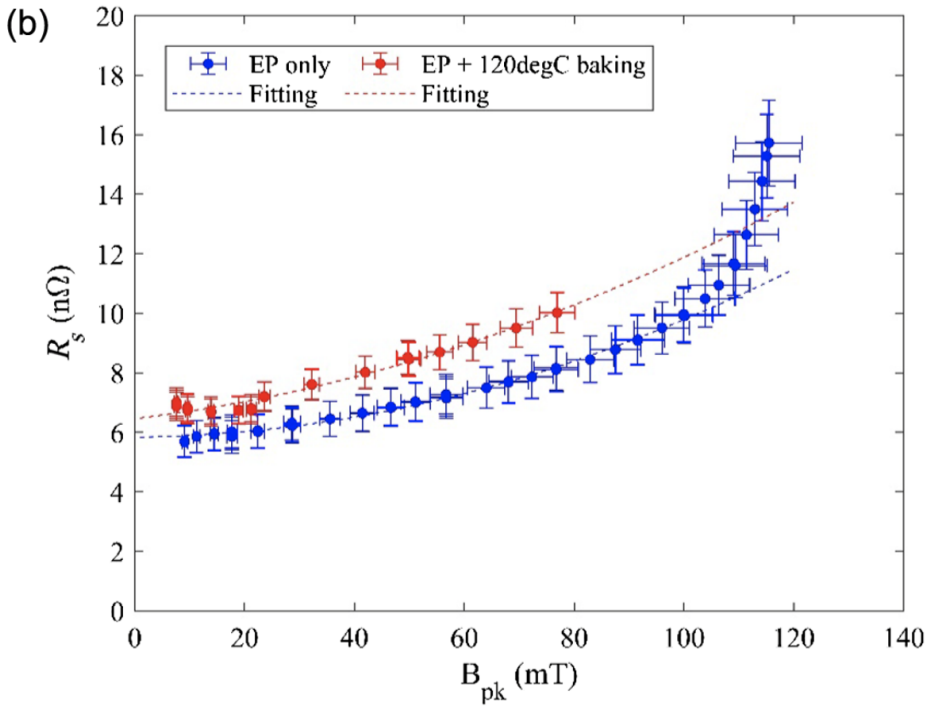

Figure 4.15: Replotted data showing the R_S as a function of cavity field, in terms of B_{pk} in mT. Second-degree polynomial fits of each data set appear as dashed lines. These fits correspond to the range in which Bpk is between 20 to 100 mT, but are extrapolated into the range of 1 to 120 mT for readability [44].

axis has been converted from accelerating gradient (MV/m) to peak surface magnetic fields, B_{pk} in mT, in order to emphasize the operative relationship between B_{pk} and R_S. This scheme more clearly shows the effect of 120°C baking in electropolished FRIB400 cavities: R_S vs B_{pk} is both increased overall in the 120°C baked cavity, and acquired a steeper slope.

The rise in R_s in the region from around 20 to 100 mT, and thus drop in Q_0 over the same range, is discussed among researchers as the 'medium-field Q-slope' (MQFS). Multiple physical effects appear to come into play in this medium-field range, one primary component of which appearing to contribute to a linear dependence of R_S on cavity field, the other contributing to a quadratic dependence [81]. In the MFQS model developed in [81], the quadratic dependence of R_S on B_{pk} arises from excessive Joule heating, and can be expressed as,

$$R_S(T, B_{pk}) = R_{S0}(T)\left[1 + \gamma^*(T)\left(\frac{B_{pk}}{B_c}\right)^2 + O(B_p^4)\right] \tag{4.11}$$

R_{S0} is the cavity low-field R_S, taken at 20 mT, which, at temperature much above 1.8 K is the sum of R_{BCS} and R_0 at that field level. B_c is the critical field, taken to be 200 mT for niobium at $T = 0$, as previously discussed [81]. T in this equation is the helium bath temperature. Here, the MFQS is captured by the $\gamma^*(T)$ coefficient, which itself is dependent on both the low-field R_{BCS} value as well as other material parameters related to the thermal conduction properties of the cavity such as the Kapitza resistance, thermal conductivity, and cavity wall thickness. If the MFQS shows a strong second-order coefficient ($\gamma^*(T)$), in the R_S vs B_{pk} fit, it would be a good indication that the R_S losses in the midfield range resulted from cavity contaminations, regardless of how the contaminants were localized in the cavity.

The origin of the linear term is somewhat more complex. Ciovati and Halbritter propose this term results from hysteresis losses due to the formation of Josephson fluxons across oxide-field boundaries permeating the niobium RF penetration layer along micro-cracks or grain boundaries [73] [82]. These hysteresis losses (R_{hys}) are expressed,

$$R_{hys}(B_{pk}) = \frac{4}{3\pi}\frac{\omega}{2J_{cj}\left[1 + (\omega/\omega_0)^2\right]^{3/2}}\frac{2\lambda}{a_J}B_c\left(\frac{B_{pk}}{B_c}\right) = R^1_{res}\left(\frac{B_{pk}}{B_c}\right) \tag{4.12}$$

where J_{cJ} is the critical current density, ω_0 is the characteristic fluxon nucleation frequency, which ranges from 5 GHz to 10 MHz, depending on J_{cJ} [81].

To align the baked and unbaked EP trials of the FRIB400 cavities with this analysis of the MFQS, we fit the data in Figure **??** to a second-order polynomial equation,

$$R_S[n\Omega] = C_0 + C_1 b + C_2 b^2 \tag{4.13}$$

where b is the field normalized to B_{pk0} which is taken as the value of B_{pk} at the FRIB400 design accelerating gradient, 77.5 mT. Thus, $b = B_{pk}/B_{pk,0}$. The coefficients C_0, C_1, and C_2 are the zeroth-, first-, and second-order coefficients respectively. In terms of the previous discussion, C_2 corresponds to $\gamma^*(T)$ and C_1 corresponds to R^1_{res}, and C_0 reflects the field-independent R_S. The fitting results, shown as dashed lines in Figure **??**, yield the table of coefficients, Table 4.3.

Table 4.2: Measured FRIB400 5-cell cavity passband modes

Case	C_0	C_1	C_2
EP-only	5.6 ± 0.023	0.15 ± 0.077	2.3 ± 0.052
EP+baking	6.5 ± 0.042	1.7 ± 0.19	1.9 ± 0.18

contributions to C_0 and C_1 are further illustrated by Figure 4.16. With the cavity held at a low, constant accelerating gradient of around 2-4 MV/m, the cavity is pumped down from 2 K to the lowest achievable temperature in the vertical test dewar, which is around 1.8 K for the FRIB vertical testing area cryoplant. The resultant data is R_S as a function of T_C/T, which, when plotted on a log scale, allows us to take advantage of the relation,

$$R_S \propto e^{-\left(\frac{\Delta(0)}{k_b T_c}\right)\frac{T_c}{T}}. \tag{4.14}$$

The temperature-dependent decrease of R_S results from the decrease in R_{BCS}, and the flat-line saturation limit that appears towards low-T (towards the right, in this scaling) approaches the value of the temperature-independent component of R_S, the residual resistance, R_0. By examining this plot we find that the low-T saturation limits differ, with the baked cavity having a higher residual resistance than the unbaked cavity at 2 K (4.6 in terms of T_c/T), a difference which is reflected in the increased value of C_0 between the baked and unbaked cases. Though C_0 technically corresponds to the sum of R_{BCS} and R_0, at low

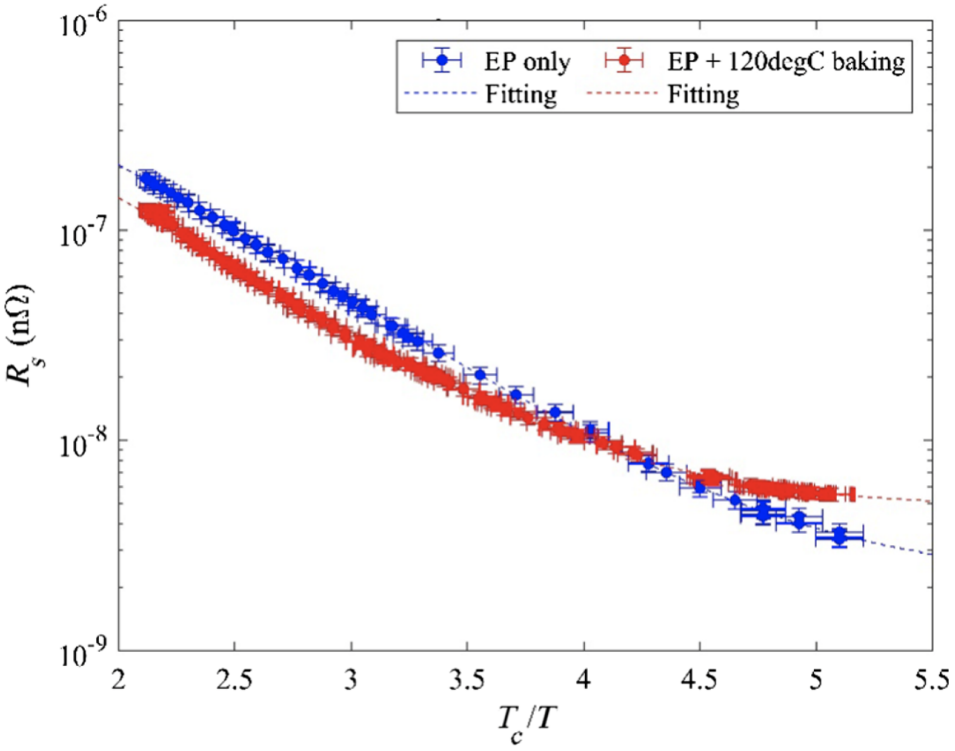

Figure 4.16: R_S as a function of T_c/T, where $T_c = 9.2$ K, the critical temperature of niobium. T is the liquid helium bath temperature. These data were recorded at constant E_{acc} of 2 MV/m for the EP-only case, and at approximately 4 MV/m for the EP+baking case. This difference in field level is not regarded as significant because the total surface resistance, R_s, is fairly field-independent within the range 2-4 MV/m.

temperatures, the contribution of R_{BCS} is exponentially reduced, and C_0 is thus taken as a proxy for cavity R_0.

When fit to the equation,

$$R_S = \frac{A\omega^2}{T} e^{-\frac{\Delta}{k_b T}} + R_0 \tag{4.15}$$

the fitting parameters are shown in Table 4.3. Notably, a $2.6n\Omega$ increase in R_0 occurred in the baked cavity. Thus, despite the visible reduction in R_{BCS} due to the baking treatment, the overall R_S at the FRIB400 operating temperature of 2 K was increased in the baked trial. There were no significant changes in the superconducting band gap (Δ).

Table 4.3: Fitting parameters for R_S

Case	A	$\frac{\Delta}{k_b T_C}$	R_0
EP-only	2.6×10^{-24}	1.9	$2.2n\Omega$
EP+baking	2.1×10^{-24}	2.0	$4.8n\Omega$

120°C baking has previously been shown to decrease the first-order term, C_1, by as much as a factor of two in 1.47 GHz elliptical cavities [73], [83], and we also find this to be the case in the 644 MHz cavities, suggesting this effect is not strongly frequency-dependent. Not all factors contributing to C_2 are known, however likely contributing factors include the thermal feedback effect and the nonlinear pair-breaking effect [73] [83]. This term did not significantly change with baking, further indicating that baking did not introduce new sources of Joule heating or dielectric losses. As one can see in Figure 4.21, the second-order polynomial becomes clearly invalid at field strengths above around 100 mT, where the physics driving the high-field Q-slope becomes dominant.

Notably, this analysis finds that the effects of 120°C baking the FRIB 644 MHz cavity differ from those of baking the 1.3 GHz ILC TESLA cavities, where 120°C baking proved so beneficial at high gradient, it became part of nearly all high-gradient treatments [69][84][85]. This difference likely arises from a variety of factors, some of which include: at 644 MHz, and at a higher B_{pk} than than that of the 1.3 GHz cavities (an effect of the $\beta = 0.6$ geometry), the FRIB upgrade cavity is subject to a greater level of R_0. This is to some degree unsurprising given that the fraction of R_0 due to magnetic flux trapping scales approximately with the square root of the operating frequency, whereas the R_{BCS} scales with the square of the operating frequency [28]. Furthermore, one of the primary benefits of 120°C baking, the removal or 'cure' of the high-field Q-slope, turns out to be somewhat irrelevant to the FRIB400 cavities. In these first RF trials of the FRIB400 prototype, we find the HFQS onset

near B_{pk} of 110 mT, which is nearly 40% higher than the design gradient of these cavities. Given that needing to operate at such a gradient is a near operational impossibility, and that otherwise the 120°C baking *raised* R_S in the relevant parameter space for the FRIB400 cavities, there is no substantial motivation to pursue such low-temperature baking-type treatments further for the 644 MHz $\beta = 0.6$ cavity design at medium gradient.

Since background magnetic field trapped in the niobium cavity during the superconducting transition at $T_c = 9.2K$ can also be responsible for changes in R_0, it is worth taking a moment to understand the magnetic field environment in the FRIB vertical testing dewar. Magnetic shielding is installed throughout the dewar, and with the lid in place, we were able to conduct a magnetic survey of the region occupied by the cavity as it hangs in the dewar for testing. The results appear in Figure **??**, where we find the background field is constrained to 7 mG or less, with an average of 2.23 mG, with the upper and lower elliptical cells subject to higher field levels than the middle cells.

EP (and BCP, for that matter) cavities are not known for their sensitivity to magnetic flux trapping. This, combined with the consistency of the magnetic shielding, suggests that the difference in R_0 between the baked and unbaked trials truly reflects the effect of the baking treatment and not any extrinsic changes to the cavity's testing environment.

Moving to the BCP trial, the 2 K Q-curve is shown in Figure **??**, in which the EP+baking data is reproduced for the purposes of making the most direct comparison. The most notable feature of the BCP+baking trial is a relatively strong low-field Q-slope (LFQS), which manifests as an inverse-Q slope in the field range B_{pk} below about 20 mT. Due in part to the nature of this LFQS, the BCP+baking treatment actually achieves higher Q_0 in the low and medium field regions, however a stronger medium-field Q-slope (MFQS) pushes the Q_0 vs E_{acc} trend in the BCP+baking cavity below that of the EP+baking cavity from $B_{pk} =$

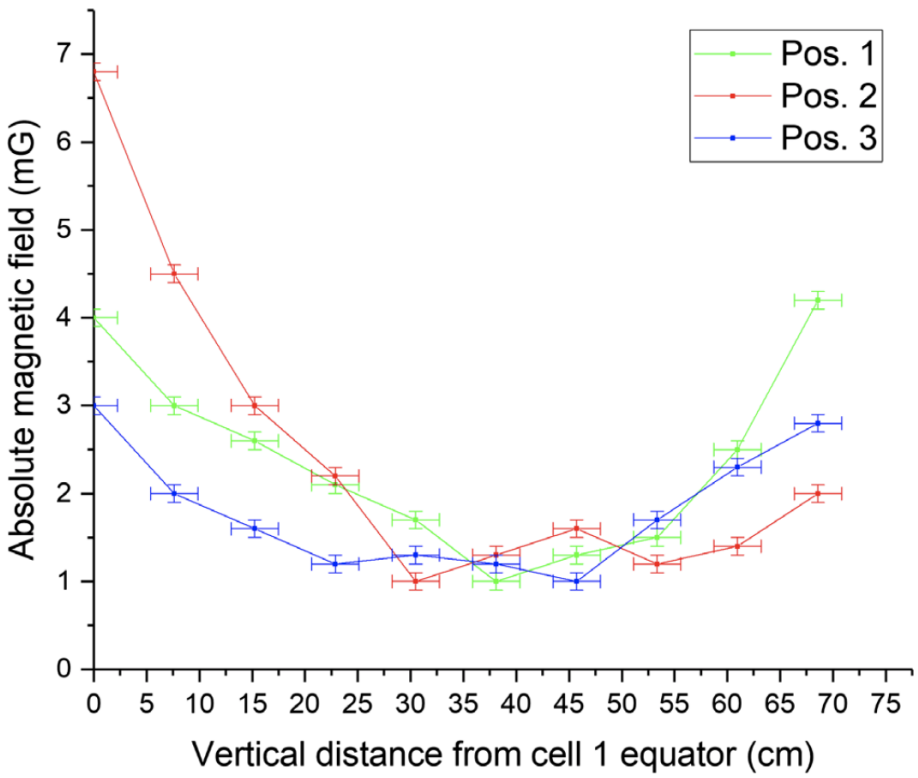

Figure 4.17: Background magnetic field in the vertical test dewar. The fields were measured by lowering fluxgate magnetostatic sensors in increments to create a vertical scan at three different azimuthal locations, spaced evenly 120° around the edge of the dewar. The sensor locations were offset from the center axis by the same distance as the cavity equator. These were measured with the cavity installed in the dewar together with the dewar lid; however, this measurement could only be conducted at room temperature, not at 2K.

60 mT upwards, which is not helpful given that the FRIB400 operating gradient is higher than this value, at a B_{pk} of 77.5 mT.

As shown, field emission was also present in this trial, but remained below 100 mR/h, making the measured Q_0 in this trial valid to compare to other field-emission free trials, up to about 14 MV/m. Across all trials, the Q_0 observed at fields below 10 MV/m, the level below which field emission was absent in all cases, was similar between field-emitting and non field-emitting cavities. This implies field-emitting cavities experienced no inherent Q_0-degradation below the x-ray emission threshold as a result of the field-emitting contaminants.

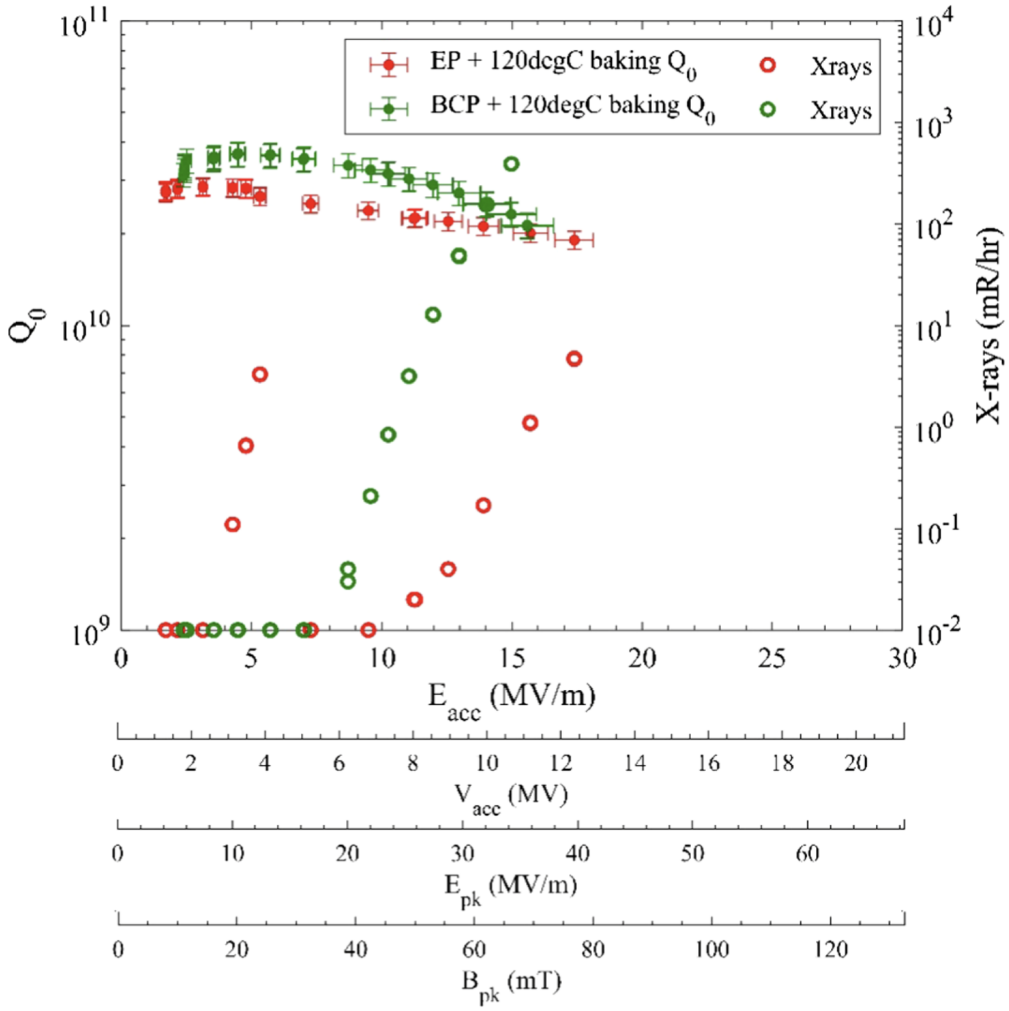

Figure 4.18: 2 K Q curves of the BCP+120°C baking treatment (green) compared to the previous EP+ 120°C baking treatment (red). The maximum gradient was limited in the BCP+baking test by field emission. The open circles denote field-emission x-rays, to be read on the right-hand vertical scale.

Thus the field-emission, while in some cases limiting to the maximum achievable gradient, was not limiting to the measured cavity Q_0.

For the sake of completion, and to close this section on the high-power RF testing, the coupling for the input (Q_{e1}) and pickup (Q_{e2}) antennae for the π mode and four other passband modes was measured and recorded below in Table 4.4. The appropriate input and pickup coupling for the π-mode may vary by vertical testing system, i.e., a lossier system

would do better to have a stronger pickup coupling, however Table 4.4 is meant as a general reference for the modal coupling.

Table 4.4: Measured FRIB400 5-cell cavity passband modes

Mode	Freq. (MHz)	Q_{e1}	Q_{e2}
#1 ($\pi/5$)	638.720	9.83×10^9	1.22×10^{14}
#2 ($2\pi/5$)	640.858	3.00×10^9	4.14×10^{13}
#3 ($3\pi/5$)	642.142	1.52×10^9	2.38×10^{13}
#4 ($4\pi/5$)	643.316	1.17×10^9	1.76×10^{13}
#5 (π)	643.789	1.61×10^9	4.36×10^{13}

4.3.1 Field Emission

A number of the trials above encountered field emission, which will now be addressed in some detail.

Field emission occurs when applied high-powered RF fields statistically causing electrons to tunnel out of their potential well and emit from the inner cavity surface. The emitted electrons then encounter the cavity fields, which accelerate the electrons until they impact the cavity walls, where their energy converts to x-rays as Bremsstrahlug radiation, and heat. Since sharp points tend to concentrate and enhance the electric field, the energy threshold for field emission is breached at lower fields at surface irregularities in the niobium, such as dust particles or regions of microscopic damage, than it is breached elsewhere. As one can see from the results above, field emission is highly undesierable. It bleeds RF power from its intended use to accelerate beam, and increases the heat output of the cavity, burdening the cryogenic system. Badly field-emitting cavities also unnecessarily increase radiation damage to accelerator electronics and other material components. To the vertical test operator, field-emission x-rays appear gradually, slowly increase with cavity field. The extent to which

these can be conditioned away depends variously on the cavity, the field emitter, how much time the operator has, how much the operator is willing to risk exploding the field emitter and catastrophically de-conditioning the cavity, the experimental setup, and more.

If a field emittor is present, heat and x-ray emission both increase as a function of applied RF field, eventually causing the cavity to quench, or causing the field-emitter to explode and spray particulate matter throughout the cavity, at which point the cavity requires reprocessing. Because reprocessing is so costly in time and resources, many institutions will place so-called 'administrative limits' on cavity gradient during testing, especially in the presence of field emission, to keep the more adventuresome VTS operators from de-conditioning too many cavities.

The current density of the field-emitted electrons follows the classical Fowler-Nordheim law,

$$j \propto \frac{E^2}{\Phi} \exp(-\frac{a\Phi^{3/2}}{E}) \tag{4.16}$$

where E is the applied electric field, and Φ is the work function of the material, 4.3 eV for niobium [29]. Wangler provides the following approximation for use in cavities,

$$j(10^{12} A/m^2) \approx (6E)^2 \exp(-\frac{6}{E}) \tag{4.17}$$

where E is measured in units of 10^{10} V/m. Unfortunately, in practice, it is not a straightforward process to apply this formula to a field-emitting cavity under RF testing, since the measured cavity field may be greatly enhanced by the aforementioned surface irregularities at the point of field-emission[29].

Cavity cleanliness is of course paramount to mitigating field emission. However, the large

surface area of the 644 MHz 5-cell elliptical cavities make them subject to more statistical defects such as particulate contamination. The chief method for cavity cleaning, high-pressure water rinsing (HPR), is further challenged by the $\beta = 0.6$ 644 MHz cavity geometry, which has a higher standoff distance from the center axis along which the HPR nozzle travels, and a low-aspect surface presentation in some areas due to the steep sidewalls.

In vertical testing of the FRIB400 prototype cavities, two x-ray detectors were installed inside the radiation shielding, one on the side of the Dewar and one on the lid, and monitored throughout testing. As noted, the initial RF testing of the FRIB400 cavities encountered field emission in most trials. Though high rates of field emission can degrade cavity Q_0, no Q_0 measurements were taken with more than 100 mR/hr of x-ray radiation detected, which is well below the threshold of expected field-emission caused Q_0 degradation [79]. Thus, the measured Q_0 degradation as a function of accelerating gradient was representative of the RF surface treatment under test, not the effects of particulate contamination.

As a method of diagnosing the field emission experienced by the RF cavities, an x-ray energy spectrum analyzer was mounted to the dewar lid during one of the vertical tests at FRIB. During a period of x-ray emission, the x-ray spectra were recorded, shown in Figure 4.19. The spectrum revealed the detected field emission consisted of 5 MeV electrons, which, coupled with CST Microwave Studio particle tracking simulations, helped identify the likliest point of origin for the highest-energy field emittor.

The CST Microwave Studio simulation was set up using the FRIB400 5-cell elliptical cavity RF volume geometry, and the field level was chosen to be the same at which the x-ray energy spectrum was recorded, around 15 MV/m. Then, different origin points were chosen throughout the cavity surface for electron emission, and the simulation was run. With the given RF properties of the FRIB400 cavity operating at 15 MV/m, only particles emitted

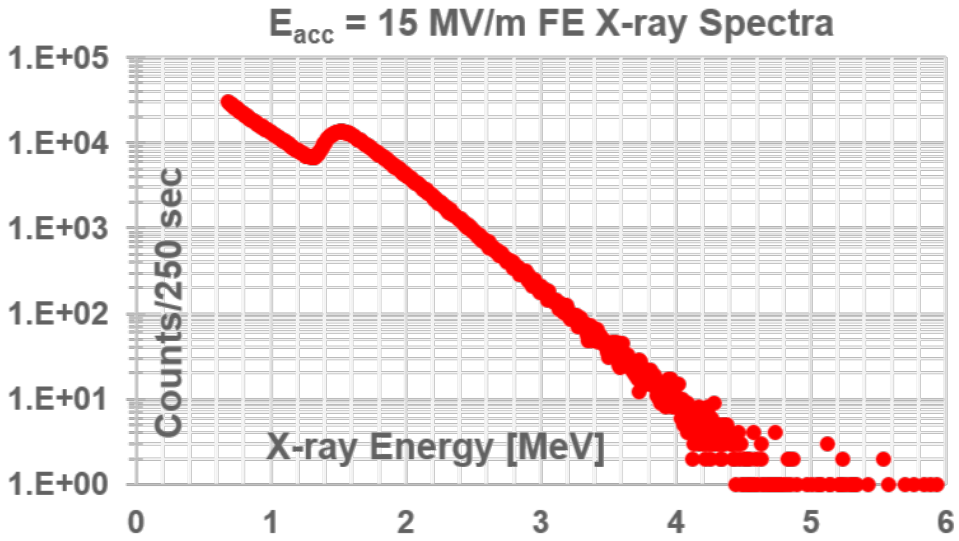

Figure 4.19: Energy spectrum of X-rays detected at the Dewar lid whilst cavity S65-001 was field-emitting. The linear slope intersecting the x-axis near the 5 MeV energy level is characteristic of the bremsstrahlung radiation emitted from a constant source of 5 MeV electrons.

from the middle iris regions were capable of being accelerated to around 5 MeV, as shown in Figure 4.20. The sidewalls, which had been concerning from a cleaning perspective, were not sources of the high-energy field emission (Figure 4.21).

Though this is in some ways unsurprising, since the iris region has the highest surface electrical field, this finding confirmed that the field-emission was due to some general inadequacy of the HPR system, and not solely a result of the device being unable to effectively clean the cavity sidewalls or equator areas. The FRIB in-house HPR system used on the 644 MHz prototype cavities in this study was developed and optimized for the FRIB baseline half-wave resonators (HWRs), which have a significantly different geometry from the elliptical cavity shape. The limited spanning angle of the rinsing wand resulted in a relatively large number of nozzles required to provide a full 360° of coverage needed for the elliptical cavity

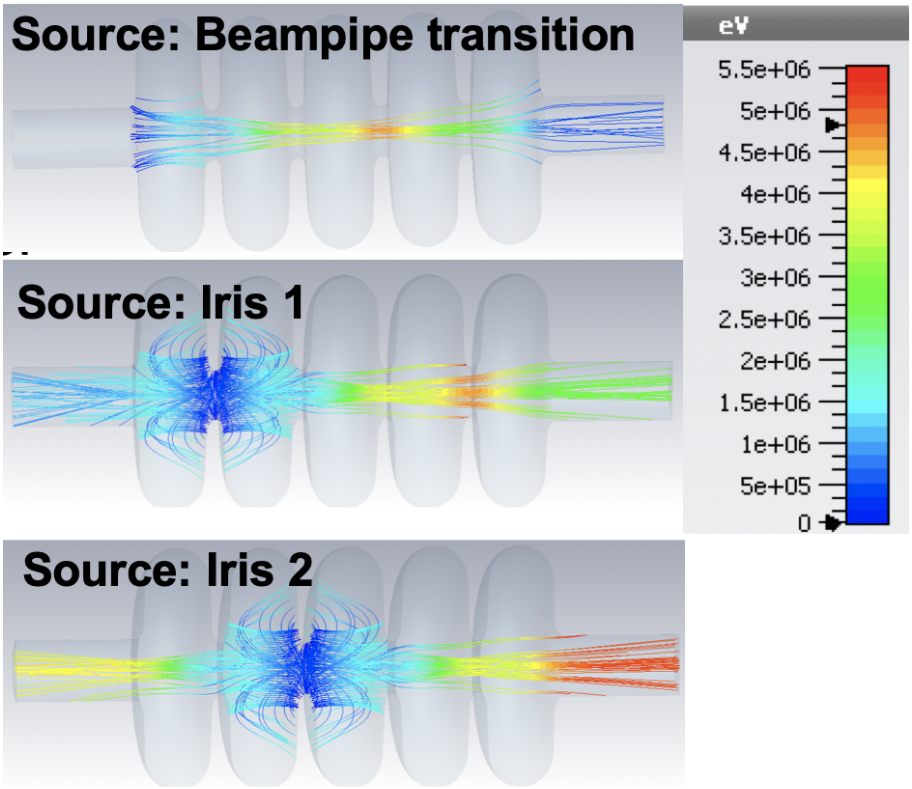

Figure 4.20: CST Microwave Studio particle tracking simulation showing possible accelerating modes of electrons emitted from various locations on the cavity irises, which become accelerated to near 5 MeV (red).

shape. Increasing the number of nozzles reduced the water jet velocity at the cavity surface, and further water jet spray pattern studies showed the course of the wand through the cavity left some gaps in coverage, particularly around the iris regions. Decreasing the number of nozzles from 18 to 12 and improving the programming for the robotic arm's motion through the cavity pushed the onset of field emission out to E_{acc}=25 MV/m, leading us to conclude some combination of these factors had resulted in the early-onset field emission seen in our vertical testing.

To more fully address these issues, a rotational HPR system optimised for use with elliptical cavities is currently under construction at FRIB. In this design, the elliptical cavity is rotated continuously around the HPR nozzle, allowing the number of nozzles to be reduced

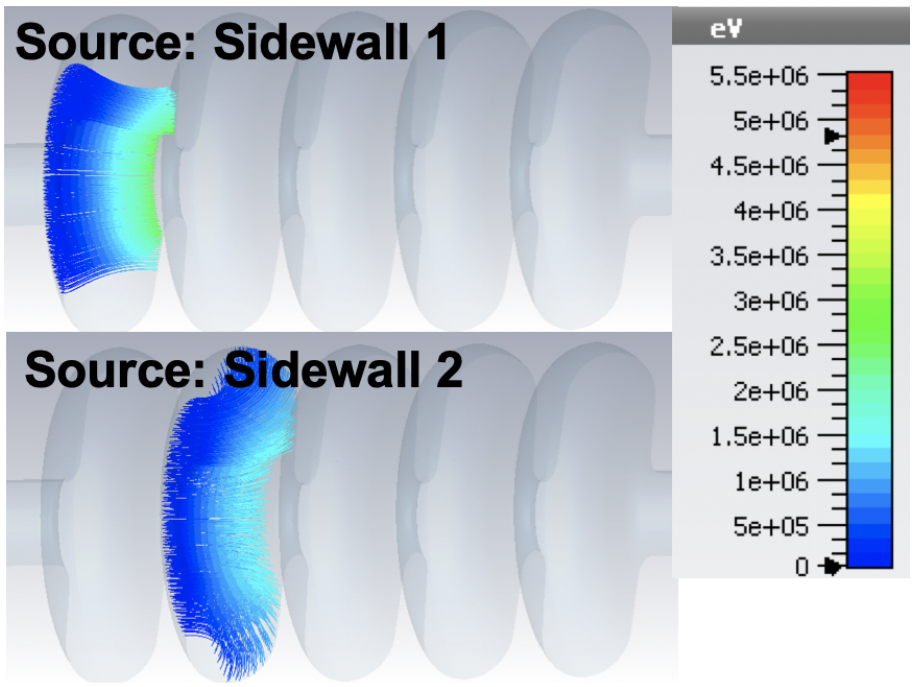

Figure 4.21: CST Microwave Studio particle tracking simulation showing possible accelerating modes of electrons emitted from various locations on the cavity sidewalls. None of the electrons originating on the sidewalls accelerate to energies near the detected 5 MeV.

significantly. With two to three nozzles, instead of 18, the jet velocity and other parameters are significantly improved, and we expect that much more complete and consistent surface cleaning can be achieved with the new HPR system in the near future.

4.3.2 Multipacting conditioning

Cavity multipacting (MP) is a phenomenon that affects virtually all SRF cavities. Prior to the first time the RF cavity is exposed to higher power RF, the cavity electrons are distributed evenly throughout the metal, moving freely. When RF energy is applied to the cavity and slowly ramped up, the applied field eventually reaches a threshold at which cavity electrons can tunnel out of their potential wells and once again interact with the cavity fields. If one (integer) half-period of the RF field is sufficient to exactly transport a wall-emitted

electron to the opposite wall, and the electron arrives with sufficient energy to knock one or more secondary electrons out of their potentials in that opposite wall, we initiate a cascade or shower-like effect, in which the number of electrons interacting with the cavity field increases as multiples of the RF periods [29].

Gradually, this population of electrons statistically shrinks, as electrons begin landing in locations from which they are unable to re-excite secondary electrons. Once the secondary electron coefficient shrinks sufficiently, the cavity gradient can be increased until another band of multipacting is encountered, or the multipacting mode is escaped entirely if the secondary electron generation coefficient drops below one, when the population of resonating electrons dies nearly instantly.[29]. To the operator, this phenomenon looks like x-rays that are relatively independent of cavity field that instantly appear at a high level and then slowly attenuate, before dropping off entirely.

The FRIB400 cavity sidewalls have large surface areas which are nearly parallel to each other, creating a situation in which a large number of electrons can become excited and meet the resonant condition for initiating secondary electron cascades. Furthermore, the range of accelerating gradients over which multipacting is predicted (the multipacting 'band') is fairly close to the operating gradient of the cavity. If significant overlap between the multipacting band and the operating gradient of the cavity is found, the effects could be highly problematic to cavity and linac operation [29].

Multipacting was first encountered in the FRIB400 cavities around 10 MV/m (Figure 4.22), or a B_{pk} of 44 mT. This corresponds to so-called first-order two-point MP resonance at the cell equators. The first-order two-point MP resonance condition on a 'flat-like' surface is

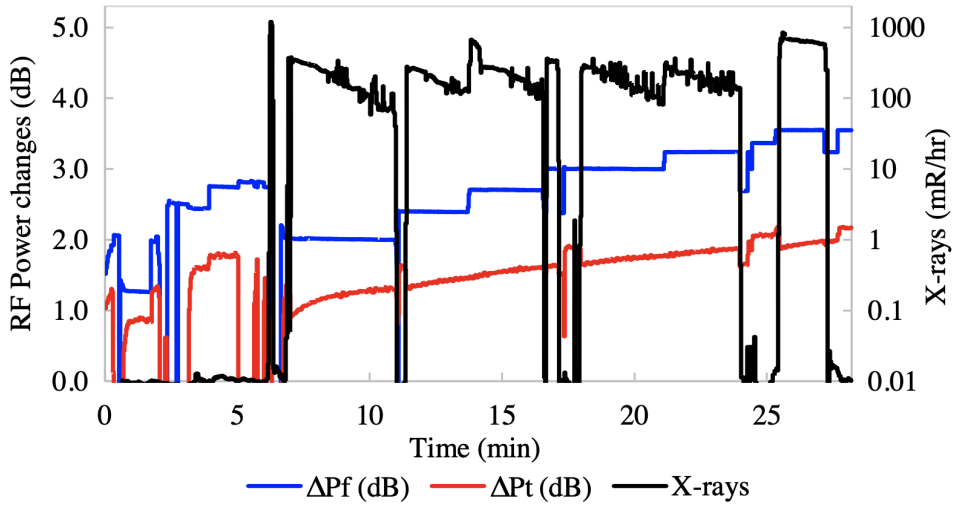

Figure 4.22: RF conditioning of the cavity multipacting in the EP-only test. Pf and Pt are the forward and transmitted RF powers, respectively. The MP first appeared at an E_{acc} of 9.3 MV/m, or $t = 0.3$ min in this plot. The first three sudden drops of Pt (t ¡ 5 min) are due to the MP-induced thermal breakdown with no X-rays. After these events, X-rays were detected and we performed RF conditioning by increasing the Pf stepwise. The MP was fully conditioned, disappearing at an E_{acc} of 10.4 MV/m (t ≈28 min). The X-ray detector was located to the side of the vertical test dewar, within 1 m from the cavity.

$$\omega_R = \frac{eB_{peak}}{m_e} = 2\omega_{RF} \tag{4.18}$$

where ω_R is the electron cyclotron resonance frequency at the given B_{pk}, m_e and e are the mass and charge of the electron, and $\omega_r f$ is the angular RF frequency [28]. At 644 MHz, this resonance occurrs at B_{pk} of 46 mT, consistent with waht was generally observed throughout FRIB400 cavity testing. Of note, the field strength at which this occurs is actually similar to the field strength associated with the multipacting band in 1.3 GHz TESLA cavities, were it scaled to that frequency [86].

In CW-mode, the cavity multipacting was fully conditioned within about 30 min. In principle, cavity multipacting also depends on cavity interior cleanliness, however given such an easy time was had conditioning the MP in all cases, the current FRIB surface cleaning

procedures and vacuum system management appear sufficient to avoid strongly contributing to MP behavior.

While the lower Q_0 observed in both 120° baking trials may disqualify the treatment automatically, 120° baking has the potential to benefit the FRIB400 cavities in other ways, namely by reducing cavity multipacting strength. However, in the course of testing we encountered no strong or hard multipacting barriers in the multipacting band, around $E_{acc} = 10MV/m$, or $B_{pk} = 44$ mT, thus 120° baking need not be employed for this purpose.

4.4 Discussion

First and foremost, we celebrate the success of the EP-only treatment, which exceeded the FRIB400 minimum design goal by 15%, with a record Q_0 of 2.3×10^{10} at an E_{acc} of 17.5 MV/m. Historical doubts regarding the feasibility of the cavity shape, and design, are thus dispelled, and the FRIB400 cavity is cleared to advance to the high-Q_0 development stage. With a Q_0 of 2.3×10^{10} at an E_{acc} of 17.5 MV/m, and given an R/Q of 386 Ω, the dynamic heat load of the cavity is calculated to be 18.2 W, which falls within the design budget of 20 W [48]. Any improvements of subsequent RF treatments on the cavity Q_0 are highly desirable as they shall increase this somewhat tight margin.

Despite successes in high-gradient 1.3 GHz TESLA cavities, we find 120°C baking did not impart any benefit to the FRIB400 cavities. Since the FRIB400 operating gradient sits well within the domain of the Q-curve dominated by the medium-field Q-slope, 120°C baking would have had to reduce the MFQS to improve cavity Q_0, however, both theoretical and experimental studies have shown that 120°C baking *increases* MFQS [73] [83] [87]. Since our results confirm these findings, there is no reason to continue development of 120°C baking

for this particular application.

Though 120° baking reduces R_{BCS}, our results show it can increase R_0, which is the dominant contribution to R_S at the relevant operating temperature of 2 K. Given the high operating B_{pk}, 77.5 mT, the scaling of the fraction of R_0 that is due to the resistance of trapped magnetic flux with the square root of the operating frequency, R_H, as opposed to the scaling of R_{BCS} with the square of the operating frequency, becomes significant. Higher-frequency cavities thus suffer more from R_{BCS} and less from R_H, and stand to benefit more from 120°C baking than the 644 MHz cavities considered here. Finally, the FRIB400 cavities also do not operate in a gradient regime in which the 120°C baking's ability to cure the high-field Q-slope is applicable.

Further bolstering the cavity design, we find herein that low-frequency accordion mode of the undressed cavity at room temperature was relatively weakly powered and has a smaller mechanical Q than that of other cavities currently operating in the FRIB baseline linac. This serves as a positive demonstration that the dominant mechanical mode of this cavity will not be resonantly excited by external vibrations in the form of microphonics, or through interaction with the Lorentz force detuning effect, leading to ponderomotive instabilities. In this vein, the next qualification step will be a demonstration of successful resonance control over the Lorentz detuning effect in a helium-jacketed cavity, and the final confirmation will be validation of the cavity resonance control stability in the fully integrated cryomodule environment, in the presence of the cryogenic systems and low-level RF control.

With an eye towards the full development of the FRIB400 linac, it is worth mentioning at this point that significant effort will be required to transfer the performance of undressed cavities in the vertical testing dewar to dressed cavities integrated into an actual FRIB400 cryomodule. In particular, further development and integrated testing of the cavity and

cryomodule subsystems will be required. Some of the most critical of these systems include the fast/slow piezo and mechanical tuners [48].

Ultimately, we have established a strong basis from which to begin study and optimization of leading high-Q_0 RF surface treatments. N-doping, of perennial interest, has proven to be a strong candidate for dramatically increasing Q_0 in 1.3 GHz TESLA cavities, [88], however substantial work is needed to understand how to adapt these successful N-doping treatments to different cavity frequencies and geometries. Preliminary studies of the frequency dependence of the N-doping effect highlight that the treatment's effect on R_{BCS} ranges from a total reversal of the dependence of Q_0 on cavity field, to a more mild reduction in R_{BCS} that does not invert the slope of the typical trend. No fully realized theory for this effect yet exists, so in the case of translating treatments such as N-doping to the FRIB400 cavities, we are left to heavily rely on the experimental method. It is therefore highly interesting to regard these prototype cavities as an additional opportunity to study the fundamental physics of the frequency dependence of the N-doping technique [89] [90]. An understanding of this dependence and how to manipulate it will be broadly useful in designing N-doping recipes for a range of cavities for a range of applications where high-Q will be useful in experimental physics as well as in industry.

4.5 Conclusions

At this stage, we have demonstrated that the novel medium-β 644 MHz 5-cell elliptical cavity design is capable of achieving reasonable levels of performance in terms of both Q_0 and E_{acc} with conventional RF surface processing techniques, and therefore is a valid cavity design in which to pursue high-Q_0 development. While the results include trials that achieve

the FRIB400 minimum design goal of a Q_0 of 2×10^{10} at an accelerating gradient of 17.5 MV/m, the potential cost-savings and state-of-the-art advancement offered by a high-Q_0 development program strongly motivate the next stage of research into the advanced high-Q_0 processing techniques. At present, we have found that the EP-only trial delivered the best performance, with a lower MFQS and lower R_0. Neither BCP nor 120°C baking appear likely to deliver the required quality factor or gradient, thus we elect to pursue no further development of these recipes at this time. Bench-top mechanical mode studies have alleviated concerns regarding the coupling of the 'accordion' resonant mode to the RF mode, which is a promising result for the prospective stability of the cavity resonance control. Despite the eccentricities of the medium-β shape, we do not expect microphonics or even ponderomotive instabilities to feed this dominant cavity mechanical mode. The cavity multipacting barrier was found to be quite surmountable, with MP conditioning taking only about half an hour on average, using CW conditioning. It is now time to turn towards the development of advanced techniques.

Chapter 5

Advanced Techniques

The materials appearing in this chapter form the basis of the work, ?Advanced surface treatments for medium-velocity superconducting cavities for high-accelerating gradient continuous-wave operation,? presently submitted to the journal Physical Review of Accelerators and Beams, May, 2023.

5.1 Motivation

In Chapter 4, we outlined the design principles and validated the novel FRIB400 $\beta = 0.6$ 644 MHz 5-cell elliptical cavities, setting the stage for high-Q_0 development. To some, the motivation for pursuit of a high-Q_0 program is self-evident: what performance limit doesn't beg to be surpassed? Particularly, when the rewards include potentially dramatic reductions in accelerator operating costs, bringing new machines into the realm of possibility? To others, however, it is worth asking, why pursue a costly experimental program when the minimum design goal for the FRIB400 cavities has already been met using established methods?

To those others, we respond as follows. A cavity achieving a Q_0 of 2.3×10^{10} at the design gradient of 17.5 MV/m certainly is indeed cause for celebration, however there are a few considerations that merit caution. First, the design goal for Q_0 of at least 2.0×10^{10} is technically the minimum required for *cryomodule* operation. Though FRIB facilities

have proven remarkably successful at preserving the vertical test performance of a cavity all the way through the eventual cryomodule installation [63], it is still prudent to budget for some amount of Q_0 degradation, given that the cleaning and handling processes for these cavities are more challenging than their FRIB baseline predecessors. Reflecting on the many statistical factors that can affect a production runs on the scale of FRIB400 (55 cavities) or PIP-II (36 cavities), a more comfortable margin in Q_0 than 15% is desirable.

Moreover, the demonstrated successes of advanced techniques such as N-doping and, more recently, furnace baking, in 1.3 GHz TESLA cavities, emphasize the potential for significant operational cost savings if either of these treatments can be successfully adapted to cavities operating in different frequency and velocity regimes. N-doping can raise TESLA cavities' Q_0 by two times or more [88], and already has a strong industrial history, being successfully employed to deliver the LCLS-II baseline [19]. Likewise, current and ongoing efforts show strong promise for furnace baking: preliminary results from in 1.3 GHz TESLA cavities show N-doping-like levels of improvement from furnace baking [91], whereas others recently tested the technique a 650 MHz single-cell $\beta = 1$ SRF cavity, achieving a Q_0 of 6.4×10^{10} at 30 MV/m [92] [93].

While encouraging, these results are nowhere near sufficient, without further investigation, to prove these advanced techniques will work to the same effect in medium-β 644-650 MHz cavities. At present, they fall far short of the rigorous demonstration that would be required by any earnest project proposal incorporating advanced techniques applied to novel medium-β 644-650 MHz cavity designs. This is primarily because the physical properties exploited by these advanced techniques have known frequency and geometry dependencies. Furthermore, given that a fully complete theory of the physics behind these advanced techniques has yet to be developed, it is judicious to assume there are yet more unknown

frequency- and geometry-dependent aspects of these treatments. An experimental approach to the optimization of these techniques for medium-β 644-650 MHz cavities is thus warranted, and is the subject of this chapter.

5.2 Nitrogen-doping

Nitrogen-doping (N-doping) is a record Q_0-achieving RF surface treatment for SC niobium cavities pioneered at FNAL in 2013 [88]. Immediately prior to its discovery, efforts to improve cavity Q_0 had focused on attempts to deposit a thin layer of material whose superconducting transition temperature, T_c, was higher than pure niobium's 9.2 K. Since the temperature-dependent component of the RF surface resistance decreases with operating temperature below the material's T_c, simply raising the effective T_c of the cavity material over the RF penetration depth had attracted interest at the time as a potentially potent method for reducing R_s.

Though the idea is relatively straightforward, it quickly became apparent that various practical challenges would make the sought-after degree of improvement in R_s difficult to realise. Multiple laboratories invested in attempts to deposit or diffuse materials such as tin (Sn), titanium (Ti), or nitrogen (N) variously with the aim of building thin layers of high T_c-compounds such as NbTiN ($T_c \approx 16$ K), Nb_3Sn ($T_c \approx 18$ K), and NbN ($T_c \approx 17$ K), [88] [94].

In the course of this work, it generally proved possible to reduce the lower critical field, H_{c1}, and the temperature-dependent component of the RF surface resistance, (R_{BCS}). However, the temperature-independent portion of the RF surface resistance, R_0, frequently increased so dramatically that the cavities were left performing hundreds of times worse as

a result. This degradation was attributed to the concurrent surface development of poorly superconducting phases of the desired compounds [88] [94], where these low-T_c inclusions statistically increased the R_0 across the entire sample.

Then, in cavities reacted with 25 mTorr nitrogen gas in a high-temperature vacuum furnace, Grassellino et al. found that after a light electropolishing of five to seven μm of removal, the Q_0 of these cavities increased dramatically, by upwards of a factor of three, in the mid-accelerating gradient range (16 MV/m) at 2 K [88]. This growth in Q_0 was due largely to the reversal of the dependence of Q_0 on accelerating field, meaning Q_0 actually increased with increasing gradient. The N-doping technique quickly became the focus of the high-Q, high-gradient SRF accelerator community, and with remarkable speed, this N-doping process was refined and industrialized for the Linac Coherent Light Source II (LCLS-II) at the Stamford Linear Accelerator Center National Accelerator Laboratory (SLAC) [19]. As of this writing, SRF cavity vendors Research Instruments (Germany) and Zanon (Italy) both have the capability of N-doping SRF cavities at scale for future projects.

Time-of-flight secondary ion mass spectroscopy (ToF-SIMS) studies of nitrogen-treated cavity cutouts subsequently confirmed that the functional aspect of N-doping was not any surface-deposited NbN phase, which is removed in the light EP step, but the presence of interstitial nitrogen in the niobium (body-centered cubic) lattice [95], [96]. ToF-SIMS uses an incident positively charged ion beam to bombard material samples and eject secondary negatively charged ions. The depth profile of various elements within the sample can then be inferred from the secondary ion signal as a function of sputtering time, with nanometer-scale resolution. From these cavity cutout measurements, we know that below first few microns, which consist mainly of niobium nitrides, the nitrogen concentration becomes constant and remains so over the RF penetration layer, i.e., for tens of nanometers [96]. Even in 9-cell

cavities, it was found that the nitrogen depth profile remained comparable between all nine cells. These studies also proved that diffused oxygen was not involved in producing any aspect of the N-doping effect [96]. Of note, more recently studied advanced techniques find that oxygen diffused into the RF layer also affects the RF surface resistance of the niobium. This phenomenon shall be discussed in greater detail in a later section concerning the furnace baking treatment.

5.2.1 Current physical understanding of N-doping

N-doped cavities access a number of fascinating physical phenomena that make them as interesting as a pure physics problem as they are from an applied accelerator development perspective. From the discovery N-doping and onwards, 1.3 GHz TESLA-type cavities have dominated the field of fundamental N-doping research, in part due to these cavities' prevalence in high energy physics accelerator applications. However, for the purposes of the FRIB400 and PIP-II cavity development, we must now ask how our still largely empirical understanding of these cavities' complex physical phenomena at 1.3 GHz can be 'translated' to 644-650 MHz. The following sections outline our current understanding of the characteristic properties of N-doped cavities, with some comments regarding how we might expect these properties to change (or not) in cavities operating at frequencies closer to 650 MHz. The nature of these comments are necessarily somewhat speculative, given that full theoretical explanations of the curious physical phenomena revealed by N-doping superconducting RF cavities remain under active study, with multiple models under current consideration [94].

5.2.1.1 Anti-Q slope

One of the most intriguing features of N-doped cavities is that the nature of the cavity's dramatic increase in Q_0 seems wholly illogical: in 1.3 GHz cavities, Q_0 increased because N-doping caused the cavity's RF surface resistance to *decrease* as a function of the applied RF field, meaning, somehow, the system was becoming less lossy the *more* energy was put in into it. Thus, as a function of the input power, or, equivalently, the cavity's accelerating gradient, the cavity's intrinsic Q_0 appeared to *increase* over a certain range of applied RF fields—a phenomenon that has since been dubbed the 'anti-Q slope.'

Clearly, something strange is afoot with the cavity's RF surface resistance, R_S, as a function of cavity field. As has been alluded to before, the field-dependence of R_S is quite complex, with different physical effects taking over in different regions of the Q_0 vs E_{acc} curve: the "low-field" behavior (low-field Q-slope, LFQS) is distinct from the "medium-field" (medium-field Q-slope, MFQS) behavior, which is distinct from the "high-field" (high-field Q-slope, HFQS) behavior. No single complete theory describing all of these effects yet exists, but we can still use experimental tools at our disposal to gain insight into the field-dependencies in regions of critical relevance to us, particularly those responsible for the 'anti-Q slope.'

A useful tool exploits the temperature-dependence of R_S to deconvolve the temperature-dependent Bardeen-Cooper-Shrieffer (R_{BCS}) resistance, which is accurately described by weakly-coupled BCS theory, from the temperature-independent residual resistance, R_0. Recall, R_S consists of two primary components, one temperature-dependent ($R_{BCS}(T)$) and one temperature-independent (R_0), vis., $R_S = R_{BCS}(T) + R_0$, or more specifically,

$$R_S(T) = \frac{A\omega^2}{T} e^{-\frac{\Delta}{kT}} + R_0 \tag{5.1}$$

where A captures certain material properties of the niobium, including the superconducting electron mean free path l, and Δ is the superconducting gap. Romanenko and Grassellino [97] were able to exploit this temperature dependence, and the low-temperature range of the FNAL vertical test Dewar, which is capable of reaching 1.5 K, to deconvolve R_{BCS} and R_0. Q_0 vs E_{acc}, or, equivalently, R_S vs E_{acc} data taken at 2 K contains some mixture of the effects of R_{BCS} and R_0, however, once the cavity temperature is reduced to 1.5 K, R_{BCS} exponentially decreases to negligible levels, and the remaining measured R_S (still the reciprocal of the G-factor), is thus essentially equal to the residual resistance, $R_0(E_{acc})$ [97]. The contribution of R_{BCS} at 2 K can then be found by subtracting the measured $R_0(E_{acc})$ from $R_S(E_{acc})$ measured at 2 K: $R_{BCS}(E_{acc}) = R_S(E_{acc}) - R_0(E_{acc})$.

We thus now have the ability to analyze both R_{BCS} and R_0 as functions of cavity field, which is a significant enhancement over the treatment of the previous chapter. Due to the limitations of the FRIB cryostat, R_0 was previously estimated by cooling the cavity from 2 K to 1.8 K at a constant field level, 2 MV/m, and extrapolating to find the saturation limit of R_0 at that field level. This was then taken to be generally the R_0 of the cavity throughout the entire field range. R_{BCS}, similarly, was taken to be the fitted slope of this R_S(T) at this field level.

With the temperature-dependent deconvolution method, we instead have the ability to extract R_{BCS} and R_0 dependencies throughout the entire field range. In 1.3 GHz TESLA cavities, [97] not only find clear field dependencies in R_0 and R_{BCS} but also find differing responses in each to various RF surface treatments. For example, the HFQS in EP-only

cavities evolves from a sharp increase in R_0 at high field, which 120°C baking nearly eliminates [97]. R_{BCS} field dependence was found to be strongly affected by 120°C baking in the 1.3 GHz TESLA cavities, reducing R_{BCS} overall, yet causing a strongly sloped increase in midfield ranges, in both BCP and EP cavities [97].

Applying this deconvolution analysis to 1.3 GHz N-doped cavities, Grassellino et al. revealed that N-doping completely *reverses* the field-dependence of R_{BCS}. This reversal in fact enables R_{BCS} to descend *below* the lowest possible value for R_S predicted by the Matthis-Bardeen theory [88]. N-doping was also found to moderately reduce R_0 overall (though in the presence of magnetic field R_0 can be substantially increased) but no substantial changes in the field dependence were observed [88]. The anti-Q slope phenomenon thus evidently stems from the N-doping treatment's specific ability to manipulate the physics underlying R_{BCS}, that is to say, some refactoring of the behavior of the superconducting quasiparticles near the fermi surface has occurred.

Previous work by Martinello et al. showed that the cavity operating frequency strongly affects the strength of this field-dependence of R_{BCS} [89]: in the medium-field range, R_{BCS} decreases as a function of field at frequencies higher than approximately 1 GHz in N-doped cavities. However, as the operating frequency lowers, this behavior gradually reverts back to the more typical increase in R_{BCS} as a function of field. Martinello et al also find that low-field R_{BCS} is decreased by N-doping as compared to EP for all frequencies, and the magnitude of this decrease grows with operating frequency [89]. The authors note it is plausible that the frequency dependence of R_{BCS} results from the applied RF field enabling the system to access frequency-dependent non-equilibrium electrodynamic effects within the superconducting niobium [89].

5.2.1.2 Non-equilibrium superconductivity

The topic of non-equilibrium superconductivity is not typically included in discussions of superconducting RF, however, the hypothesized connection between non-equilibrium superconductivity and the nitrogen (or, later, oxygen)-doping effects in SRF cavities makes it worthwhile to provide an overview of the concepts here. A more thorough introduction can be found in [36], which the following overview draws on substantially.

Picking up from where we left BCS theory in Chapter 3, a superconducting system at rest (in the ground state) consists of some population of Cooper pairs. These have accessible to them the single-particle (quasiparticle) excitation states of energy E_k,

$$E_k = (\Delta^2 + \xi_k^2)^{1/2} \tag{5.2}$$

where Δ is the band gap from BCS theory, and ξ_k is the energy of the k-th excitation state measured from the Fermi energy. The nature of these quasiparticle excitations is such that when excited above the Fermi energy they take on electron-like qualities, and in that way can be thought of as a version of the normal-conducting electrons in the two-fluid model from Chapter 3. The work of Chapter 3 assumed these quasiparticles were in thermal equilibrium, and thus by definition, the probability distribution of their occupation of available states is the regular Fermi function,

$$f_0\left(\frac{E_k}{k_T}\right) = [1 + e^{E_k/k_B T}]^{-1} \tag{5.3}$$

Non-equilibrium superconductivity arises when some stimulus causes the *actual* distribution of the quasiparticle occupation of states, f_k to differ from this equilibrium function

above, i.e., $f_k \neq f_0\left(\frac{E_k}{k_T}\right)$. In the context of superconducting RF cavities, stimulus is the applied RF field, and in light of the results of Martinello et al., we seek to understand how the RF frequency, or n-doping modification of the niobium surface within the RF penetration depth, (or both) could support some sort of non-equilibrium distribution of quasiparticle states, f_k.

The frequency-dependence of the effect found in [89] provides a significant clue. Any non-equilibrium system has an inherent time-scale associated with it, the relaxation time, τ_R, which is a measure of how long it takes the non-equilibrium states of f_k to vanish after the stimulus (the EM field) has been removed. This is equivalent to asking how long it takes the normal fermi distribution of quasiparticle states, f_0, to return after the EM field is turned off. Crucially, our particular EM field is an RF field, thus it is repeatedly turned off and on again on a time-scale defined by the cavity operating frequency.

We can now ask what happens when one of these time-scales is longer (or shorter) than the other. Clearly, if the RF driving the system repeatedly kicks it faster than f_k returns to f_0, a stable non-equilibrium state is established and some f_k becomes constant in time. While how *much* faster the RF switching needs to be than τ_R is undefined, Martinello et al., find strong anti-Q slopes emerging in *untreated* SRF cavities operating at 3.9 GHz [89], which has a corresponding time-scale of around 0.259 nanoseconds. This places at least an upper bound on the τ_R of the untreated superconducting niobium system under the influence of driving RF. Similarly, given the emergence of the anti-Q slope in 1.3 GHz N-doped cavities, it is plausible that N-doping reduced τ_R in some way, such that the time-scale defined by an operating frequency of 1.3 GHz sufficiently fast to sustain a similar f_k.

The question emerging from this analysis is thus, what are the factors that determine the τ_R of a cavity system, and how can they be 'tuned,' via N-doping or other means, to the

benefit of Q_0 at the desired operating frequency? The serendipitous discovery that 2/6 N-doping of 1.3 GHz TESLA cavities, which have a mean-free-path lengths around 90-100 nm, apparently modify τ_R enough to establish the correct relationship between the RF period timescale and the τ_R time-scale.

Cavity operating frequency, however, is strictly set by the machine parameters. Thus, the more practically tunable timescale is τ_R. Unfortunately, the means by which τ_R can be modified are much more nebulous, and to some extent, still remain unknown [98]. It is certain that the electron-phonon scattering rate is directly proportional to τ_R however [36].

Experimental evidence for this effect has arisen over some time in other contexts, such as in aluminum resonators [99], where it was possible to measure that resultant broadening of the density of quasiparticle states decreases the population of quasiparticles near the superconducting gap, making them less susceptible to losses due to photon absorption. Above minimum temperatures, this effect lead to increasing Q_0 as a function of the applied field. Recent theoretical work in the dirty limit of niobium has confirmed one can expect the amplitude of these quasiparticle states, and thus the nonlinear effects, to be significantly attenuated below operating frequencies of about 1 GHz [100]. It thus seems plausible that the results of Martinello et al. are another instance of the same microwave enhancement of superconductivity. While this understanding is insightful, its utility is still somewhat limited given that the precise role of the dopants (either N or O) in altering the relaxation time of the superconductor remain a current topic of research.

While this suggests we cannot expect to reap the benefit of the anti-Q slope in 650 MHz cavities with current N-doping recipes, Martinello et al. showed that N-doping still lowers the rate of R_{BCS} increase at medium fields, such that one can estimate that at the FRIB400 peak magnetic field (Bpk) of 77 mT, of R_{BCS} is still likely to be lower overall after N-

doping. The authors find that in both single and multi-cell 650 MHz cavities that N-doping delivered the best quality factors of the tested treatments, despite this detrimental frequency dependence. These N-doped cavities experienced quench fields on average around 24 MV/m, which is comfortably above FRIB400 operating gradient, 17.5 MV/m [89].

5.2.1.3 Flux sensitivity

On cooling through T_C, superconducting materials expel applied magnetic field, however, in the case of a type-II superconductor such as niobium, some field inevitably becomes quantized and trapped within the bulk material in the mixed superconducting state. These quanta of trapped magnetic flux, or "vortices," contribute to the temperature-independent fraction of cavity losses, R_0. N-doped cavities are notorious for their tendency to have stubbornly high values of temperature-independent surface resistance (R_0), even after ideal surface preparation removes the typical contributions of normal conducting defects and poorly-conducting oxides and hydrides to R_0. The remaining, intractable source of increased R_0 in N-doped cavities is their significantly increased sensitivity (S) to trapped magnetic flux. S, defined as the increase in additional cavity resistivity per unit of trapped magnetic flux, measured in units of nΩ per mGauss, has been found to increase by as much as three times in N-doped cavities over their electropolished baseline value [101] [102]. This tendency is so pronounced that R_0 essentially always makes the dominant contribution to the overall RF surface resistance in N-doped cavities. Thus, the mechanisms that lead to high R_0, primarily through increased S, and the possible means of mitigation, occupy a significant fraction of N-doping optimization efforts.

Without mitigation, cavities are typically subject to around ten of mGauss of background DC magnetic field, stemming mostly from the Earth's magnetic field, with some possible

contributions from nearby magnetized equipment. In the context of a cryomodule, good magnetic hygiene and passive shielding can reduce this ambient field significantly, however in N-doped 1.3 GHz cavities, S values of between 3-4 nΩ/mG are not uncommon [101]. Thus, even when the background magnetic field is successfully attenuated to just a few mGauss or less, an S of 3-4 nΩ/mG can still be highly detrimental to cavity performance, particularly in high-Q cavities aim for an overall R_S of well below 8-10 nΩ.

In 1.3 GHz single-cell cavities, Martinello et al. [102] and Gonella et al. [103] both found that S was highly dependent on the electron mean fee path, l. Curiously, this dependence is bell-shaped, showing minima in S for both very low ($l <$ 70nm, typical of 120°C baked cavities) and very high ($l >$ 180nm, typical of EP/BCP cavities) mean free path lengths, with a peak in S occurring roughly between 80 and 120nm [102]. Unfortunately, N-doping a cavity reduces l from its EP baseline value, bringing the cavity into the worst region of increased S as a function of l. Heavier doping treatments produce the l values (l=80 to 100nm) closest to the maximum of S, but lighter doping treatments, resulting in cavities with l values of 120-180+ nm, are able to somewhat avoid the peak S region. Recall, however, that R_{BCS} is also a function of l, and at 1.3 GHz, as Nature would have it, this function is minimized around l = 100 nm at 16 MV/m [102]. There is thus a difficult balance to be struck between tuning l to minimise both R_{BCS} and S at 1.3 GHz, suggesting the same is likely true at 644-650 MHz.

Initial theoretical treatments of the dissipative mechanisms of flux-trapping considered trapped flux vortices as objects with normal-conducting cores of a radius a on the order of the coherence length, ξ [103]. The applied magnetic field ($B_{applied}$) is split among N vortices of flux quanta Φ_0, such that $B_{applied} = N\Phi_0$. The field of Φ_0 decays over the penetration length λ_L from the center of the core, and the dissipative loss due to each vortex in this

simple model is just the area of the normal conducting core ($\pi(a \approx \xi)^2$) multiplied by the normal conducting resistance of the niobium, R_n. The sensitivity thence becomes

$$S = \frac{\pi a^2 R_n}{N\Phi_0} \tag{5.4}$$

Both a and R_n have dependencies on l, and R_n is also frequency-dependent (ω). The nature of these dependencies change in the "dirty" ($l < \xi_0$) and "clean" ($l > \xi_0$) limits, and following Martinello's analysis in [104], in the normal skin effect regime, S takes on the two different forms

$$S_{clean} = \frac{\pi}{\Phi_0}(1.16\xi_0)^2\sqrt{\frac{\mu_0\omega\mu_F}{2ne^2l}} \tag{5.5}$$

$$S_{dirty} = \frac{\pi^2}{3\Phi_0}l\xi_0\sqrt{\frac{\mu_0\omega\mu_F}{2ne^2l}} \tag{5.6}$$

Leaving aside the frequency (ω) dependence for the moment, we see S_{clean} winds up with a $1/\sqrt{l}$ dependence, and S_{dirty} has a $\sqrt{l}$ dependence. These two functions, and the imaginable transition region between them, roughly reproduce the general bell-shape dependence observed in the experimental data. However, on closer inspection, this model overestimates S, and shifts the observed peak region left, confirming what one might have suspected from the start: that, while intuitive, a simple treatment of vortex losses as static normal conducting cores with finite radii does not capture the full range of physics at play [104].

Checchin et al. [105] have since showed that the bell-shaped l-dependency of S seen in the experimental data can emerge from a vortex-dynamics treatment alone. In this model, Checchin et al. consider a vortex as a one-dimesnional filament whose displacement is defined

by a pinning force that changes as a function of depth, z, from the RF surface. Thus the vortex can be multiply pinned along its length, allowing it to assume a more string-like nature as opposed to the straight, rigid core imagined in the first model. In their analysis, Checchin et al. solve the equation of motion for a single vortex, with inertial mass M which is subject to the usual Lorentz force (f_L), a pinning force (f_p), and a viscous drag force (f_v):

$$M\ddot{x} = f_L + f_v + f_p \tag{5.7}$$

The Lorentz force is the familiar cross product of the RF-induced eddy currents ($\mathbf{j}$) acting on the normal component of the magnetic field $\phi_0\hat{\mathbf{u_n}}$. where the Lorentz force takes the form:

$$f_L = |\mathbf{j} \times \phi_0\hat{\mathbf{u_n}}| = j_0\phi_0 \sin\theta e^{i\omega t - z/\lambda} \tag{5.8}$$

An expression for the vortex viscous drag coefficient ξ developed by J. Bardeen and M. Stephen [106] enable the definition:

$$f_v = -\xi \cdot x = -\left(\frac{\phi_0 B_{c2}(T)}{\rho_n}\right) \cdot x \tag{5.9}$$

where ρ_n is the normal conducting resistivity, and also define the vortex inertial mass, M. Checchin et al. then construct a bi-dimensional pinning potential. The first dimension consists of the Lorentzian potential as a function of depth, z, from the RF surface, as it affects the multiple considered pinning sites along the length of the vortex. The second dimension consists of a parabolic approximation of the pinning potential traveling along the direction of oscillation, x. From this point, Checchin et al. develop an analytic solution to the vortex equation of motion, the results of produce a function for S that is impressively

well-matched to the experimental data.

The extremum of the bell-shaped curve in this analysis illustrate two distinct regimes of losses: the flux-pinning regime in the short-l limit, and the flux-flow regime in the long-l limit [105]. The flux-flow regime has the simpler implications for lower-frequency cavities: a longer mean free path length, l, leads to a smaller normal conducting resistivity, ρ_n, meaning the viscous drag coefficient ξ is enhanced. The pinning potential weakens significantly, thus the flux-pinning force, f_p, becomes negligible. Qualitatively, this describes a limit in which the vortices flow freely between local pinning locations. Solving the equation of motion for the flux-flow regime alone, Checchin et al. find that the resistivity has no frequency dependence, and is determined only by the mean free path, where longer mean free path lengths minimize the resistivity arising from vortex flow [105]. Thus at 644-650 MHz we do not expect significant changes to the flux sensitivity, S, from its 1.3 GHz value, in the clean limit, and indeed we have already seen as much in the electropolished cavity data discussed in the proceeding chapter.

The flux-pinning regime carries the more complex implications for N-doped cavities operating at lower frequencies. As the mean free path shortens, the viscous drag coefficient, ξ, decreases, and the strength of the pinning potential increases [105]. The vortices are no longer flowing through the material, but are oscillating within their local pinning potential. Checchin et al. show the resistivity assumes both real and complex portions, illustrating that the vortex interaction with the RF field can be both resistive and reactive between between the long-l and short-l limits:

$$\rho(z,l) = \frac{\omega\phi_0^2 \sin^2\theta}{\pi\xi_0^2 p^2}[\xi\omega + ip] \tag{5.10}$$

importantly, we see an ω^2 dependence emerging in the pinning regime [105], indicating that, even without sophisticated analysis, operating frequency likely plays a role in defining the RF loss mechanisms due to trapped flux. As the mean free path further decreases, the imaginary coefficient is minimized and the vortex resistivity becomes completely real, i.e., reactive, [105]. Since our present concern is with intermediate-l in the N-doped cavities [90], we now move to a closer examination of the frequency dependence of that troublesome mid-peak region.

As one might intuit, the frequency-dependence and the mean-free-path-dependence of the cavity's sensitivity to trapped flux, S, ultimately turn out to have an interesting inter-relationship [90]. Rewriting the resistivity to make the l and ω dependence more explicit, Checchin et al. develop the expression:

$$\rho(l,\omega) \simeq \frac{\omega\phi_0^2}{\pi\xi_0^2[(p(l)-M(l)\omega^2)^2+(\xi(l)\omega)^2]} \times [\xi(l)\omega + i(p(l)-M(l)\omega^2)] \tag{5.11}$$

Neglecting the imaginary portion, (and the vortex inertial mass, M, which is small) we find that not unlike the case with l, two different regimes of behavior emerge for high- and low- ω. In the low-ω limit, the real portion of the resistivity approaches the value $\rho \approx \xi\omega^2/p^2$, whereas in the high-$\omega$ limit we find ρ approaching a constant value. As observed in [90], these two limits once again correspond to the flux-pinning and viscous flux-flow regimes of vortex behavior in superconducting materials, revealing that the operating frequency of the cavity has the ability to 'tune' the point of interchange between these two loss mechanisms in a manner similar to l. The dependence of the flux sensitivity S on frequency becomes somewhat complicated for values of ω between the two extrema addressed above. Following

from the full discussion in [90], for constant l, decreasing the operating frequency, ω, has the effect of shifting the peak of cavity sensitivity, $S(l)$, to the right, towards higher l values.

Having developed this basis, we may now hypothesize how flux sensitivity will affect the FRIB400 644 MHz cavities after they have been N-doped. The expected l resulting from N-doping 644 MHz cavities should not deviate significantly from that measured in the 1.3 GHz cavities, thus it would be on the order of roughly $l = 80$ to 100 nm. For constant l, the effect of decreasing the operating frequency from 1.3 GHz to 644 MHz is to shift peak sensitivity $S(l)$ to higher values of l, meaning the $l = 80$ to 100 nm range, which fell at peak sensitivity for 1.3 GHz cavities, falls more to the left of the peak for 644 MHz cavities, suggesting these cavities will be subjected to, at worst, similar, but at best, lower S than their N-doped 1.3 GHz counterparts. Simulation data in [90] confirms this, in the simplified view of a single pinning center. However, as the authors note, the nature and distribution of the pinning centers in the material can significantly change the global nature of this function integrated across the an entire cavity. Without knowing, *a priori*, the nature and distribution of the pinning centers in the bulk niobium material, the predictive power of the above formulation is somewhat limited. Fuller consideration of the nature of the flux pinning centers in SRF cavities is reserved for Chapter 6, where material properties affecting flux trapping in the bulk niobium are investigated in more detail, however, for the purposes of this section, we note that possible flux pinning cites include grain boundaries, dislocations, and other material imperfections in the niobium matrix. These vary depending on cavity heat treatments, the working methods, and even on the niobium material vendors.

A final consideration rests in the field-dependence of the flux sensitivity [107]. Using Monte Carlo simulations of single-vortex behavior in a random arrangement of pinning centers, Checchin and Grassellino find that, in this simplified model, at low fields, the vortex

response is linear and thus resistivity is fairly constant as the vortex remains within its local pinning center [107]. As the applied field increases, adding energy to the system, the vortex gradually acquires the ability to jump to nearby pinning centers. When this occurs, the power dissipated by the vortex abruptly falls, before beginning to build again as a function of field. As the applied field is increased still further, the vortex dissipation becomes independent of the pinning center distribution, and approaches a constant, saturated value [107]. The authors are again careful to note the strong effect the pinning center distribution has on the crossover points between these behaviors, and the inherent limitations of numerical calculations of this nature given such complete knowledge of the pinning landscape of any given material is impossible to know *a priori*.

Still, the vortex-level predictions of [107] coupled with the experimental data of [90] appear to show that, integrated across the entire cavity surface, in the 4-20 MV/m range, the 650 MHz cavities overall experience a small, linear increases in S, amounting to no more than one to two tenths of a nΩ/mG across the entire operationally relevant gradient range. Experimentally, [90] shows rate of increase in S as a function of field is somewhat frequency dependent, with the higher-frequency cavities experiencing the faster increase, meaning that 644-650 MHz cavities are operating in by far the most favorable region of this particular trend.

In summary, the flux-sensitivity and its contribution to the R_0 of any particular cavity is a complicated function of a fundamental superconducting phenomenon (vortices) interacting with its macroscopic environment, which consists of the random, natural features of the niobium metal resulting from the fabrication and treatment processes. While these extrinsic factors contribute to variance in the expected S, agreement between the models developed by Checchin et al. [105], [90], and experimental trials indicate that in the case of nitrogen-

doping the FRIB400 644 MHz cavities, we can expect no significant worsening of S, and may even see some slight improvement over the S values typical of N-doped 1.3 GHz cavities.

5.2.1.4 Quench limit

Another characteristic RF property of N-doped cavities is that they have significantly lowered quench fields compared to their EP baseline performance, which is of concern in the context of high-Q, high-gradient applications such as the proposed International Linear Collider (ILC), and other even more speculative future projects. While the field of SRF aims broadly to push both the Q_0 and the gradient frontier, in the context of the modest gradient of the FRIB400 research and development project, we are afforded the leeway to pursue high-Q_0 treatments without too much concern for gradient, provided quench fields remain comfortably above 17.5 MV/m.

While the quench limitations of N-doped cavities are thus not the primary concern of this work, early quench is such a prominent feature of N-doped cavity performance that it warrants a brief discussion. Two basic mechanisms causing cavity quench have been proposed 1. thermal quench and 2. magnetic quench [108]. A thermal quench occurs when the applied RF field generates excess heat in a material defect in the cavity surface, such as in a surface-deposited spot of some variety of nitride. This low-T_c material turns normal-conducting at a lower temperature than the surrounding niobium, becoming a significant source of local heating. This additional heat quickly pushes the nearby niobium above the superconducting threshold, initiating the near-instantaneous cascade effect of thermal quench. D. Bafia et al. employed a thermal mapping (TMAP) technique on 1.3 GHz cavities to show that quench spots that are likely thermal in nature often have a long preheating period, in which one can see the thermal output of the hotspot growing gradually as a function of the applied field

before quench occurs. These cavities also tend to quench at lower fields [108].

Magnetic quench is, as its name suggests, not a direct consequence of surpassing a heating threshold, but a magnetic one. As a type-II superconductor, niobium has a defined region between a lower critical magnetic field, H_{C1}, and an upper critical field, H_{C2}, in which it is energetically favorable for magnetic flux to penetrate the bulk niobium material as stable vortices. If the applied field surpasses H_{C2}, the material is driven into the normal conducting regime. As mentioned, H_{c2} for Nb is around 500 mT, yet Nb cavities so far are limited to around 200 mT, indicating the presence of other contributing factors that effectively lower H_{c2} in some way. In TMAP data, a magnetic quench point shows little to no pre-heating before a rapid rise in thermal output as a function of applied field occurs just before quench [108]. Magnetic quenches tend to occur at higher fields, and have origin points nearer the equator of the cavity, where the highest surface magnetic fields are located [108]. In a study of N-doped 1.3 GHz cavities, Bafia et al. conclude from TMAP data that the quenches of N-doped cavities are likely to be magnetic or thermomagnetic in nature, implying that some property specific to the N-doping treatment lowers H_{C2} in these cavities. A lowered H_{C2}, coupled with the field enhancement effects of local magnetic impurities, would indeed seem to make it highly likely the quench-limiting mechanism in N-doped cavities usually magnetic in origin.

Though N-doped cavities appear specifically at risk for magnetic quench, neither thermal quench nor magnetic quench have overt frequency dependencies, thus we do not expect the phenomenon to deviate significantly at 644-650 MHz from this cause alone. However, as always, an important corollary to the frequency change is the differing physical dimensions of the cavity, which enhance the cavity's risk to statistical defects in processing, which may enhance the likelihood of thermal quench.

5.3 Methods

The nitrogen-doping of the two FRIB400 prototype cavities was carried out in collaboration with FNAL.

5.3.1 (2/6), (2/0) N-doping procedures

Following the procedures described in Chapter 4, both cavities were reset with at least 50 μm EP, the last 10 μm of which conducted at 15-17° C for "cold EP." Afterwards, baseline Q_0 vs E_{acc} measurements were retaken for each cavity, which demonstrated that the effect of the previous series of cavity treatments had been successfully removed. Both cavities underwent hydrogen degassing prior to the conventional RF treatment study of the previous chapter, and no other high-temperature treatments were applied to these cavities prior to this study. All EP processing steps were performed at the EP facility at Argonne National Laboratory, using the modified EP cathode described in Chapter 4.

The N-doping of a cavity begins with freshly preparing the RF surface with a bulk EP, culminating in around 10 μm of cold EP. The cavity ports (beam pipe, pickup, and input coupler flanges) are fitted with niobium end caps and foil, which promote even distribution of nitrogen throughout the cavity: in 9-cell TESLA cavities without any end coverings, early quench locations were systematically localized at the end of the cavity that happened to be closest to the nitrogen inlet in the vacuum furnace, which is characteristic of "overdoped" behavior [109]. The cavity is then heated to 800°C in the vacuum-furnace, and maintained at that temperature for around 3 h. Then, 25 mTorr of nitrogen gas is introduced via a manifold system and input port in the vacuum furnace for some number of minutes (X minutes, in the 'X/Y' recipe naming convention), followed by some (Y) minutes of annealing

at 800°C, before cooling the cavity to room temperature. The doping time (X) most directly controls the doping level, which can be understood in terms of the electron mean free path, l. Long doping times lead to shorter l, which carries with it characteristically low quench fields. The precise function of the annealing time is less well understood, with values of anywhere between 0 and 60 minutes having been trialed to varying degrees of success.

Thus, it has been through empirical means that a few popular X/Y combinations have been identified. 2/6 doping has been extensively studied and ultimately employed for the LCLS-II baseline [19]. 3/60, proposed by Jefferson Laboratory, was investigated in 1.3 GHz cavities and found to lead to very low R_{BCS}, however, suffered from lowered quench fields, and elevated sensitivity to magnetic flux [108]. In high-β 650 MHz single-cell cavities, 3/60 doping significantly reduced quench-field compared to 1.3 GHz cavities, and also had the highest R_0 of the treated cavities, and as a result, this recipe was not elevated for study in multi-cell 650 cavities, in favor of the superiorly performing 2/6 recipe, which was [110]. Investigations of 2/0 doped cavities suggested they had lower trapped flux sensitivity [109]. 2/0 doping, plus post-doping cold EP, was then applied to 1.3 GHz 9-cell cavities for the LCLS-II HE verification cryomodule, leading to that recipe's choice for the LCLS-II HE production run [111].

In view of these findings, we elected to trial 2/6 and 2/0 doping in S65-001 and S65-002, aiming for reduced (although not reversed) R_{BCS} and minimal R_0. These first treatments were conducted in the vacuum furnace at FNAL capable of N-doping large cavities. Time-series plots of both temperature profiles and residual gas analyzer (RGA) pressure data for both treatments are shown in Figure 5.1 and Figure **??**.

The performance of N-doping treatments is also sensitive to the depth of niobium removed in the post-doping light EP step. The primary function of this step in all cavities is to remove

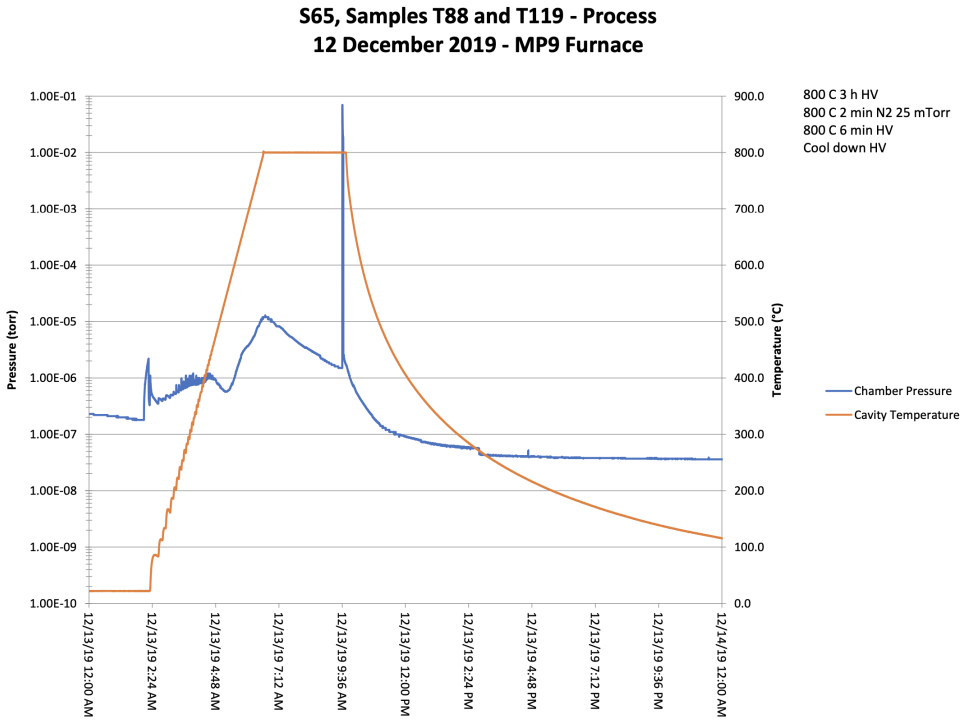

Figure 5.1: Time series gas pressure and temperature profile of the first 2/6 N-doping procedure conducted on S65-001 at FNAL.

surface-grown niobium nitrides, however it has been empirically established that there exits a "happy medium" between too little removal, and too much removal. Martinello et al. found that 7 μm was optimal in 2/6 N-doped high-β 650 MHz cavities [110], which we adopted for the $\beta = 0.6$ 644 MHz cavities. The limit between too little (early quench) and too much (reduced performance gains of N-doping) post-doping EP removal appears to be on the order of a few μm, which requires an impressive degree of control and uniformity of removal on the scale of the inner surface of the 644 MHz 5-cell elliptical cavities. While the results herein demonstrate that current EP processes are up to the task, tolerances this narrow are still worth being wary of.

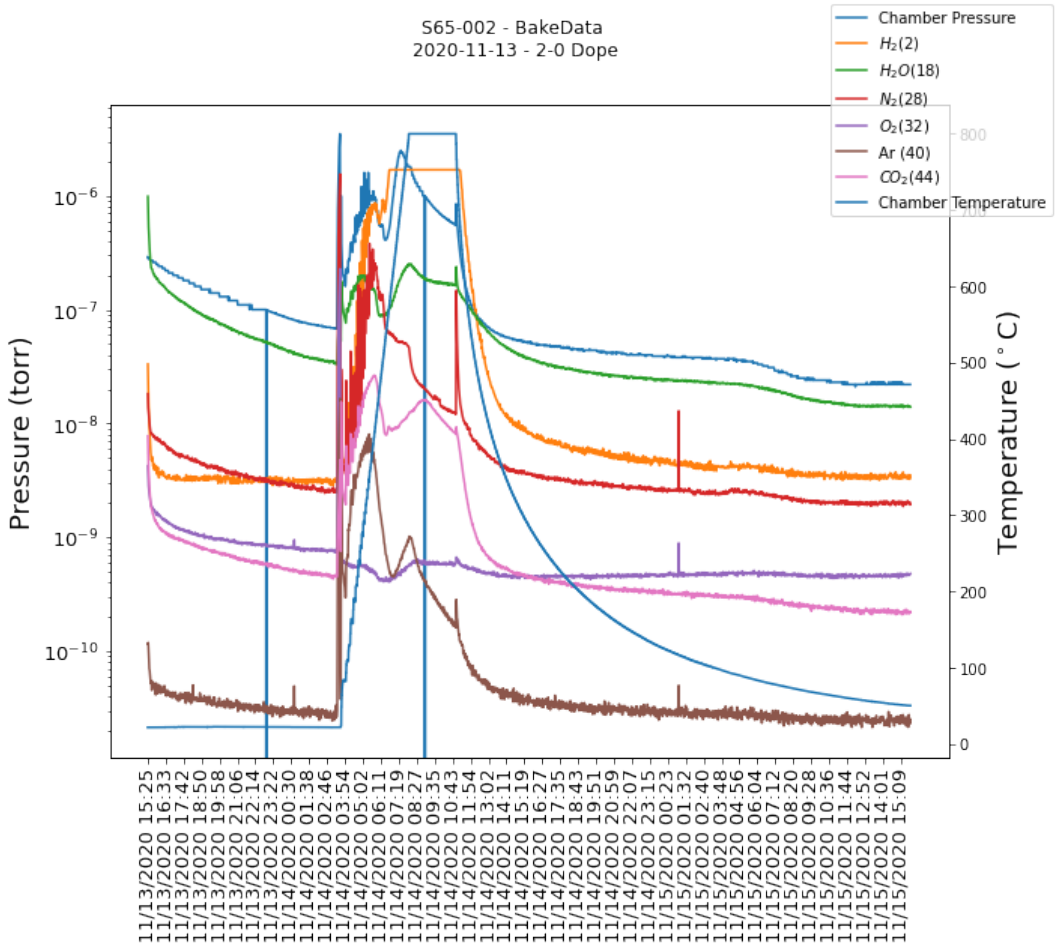

Figure 5.2: Time series gas pressure and temperature profile of the first 2/0 N-doping procedure conducted on S65-002 at FNAL. Note the spike in the read curve corresponding to nitrogen injection.

5.3.2 RF testing results

RF testing of the N-doped cavities was conducted at both MSU and FNAL vertical testing facilities. Given the expected sensitivity to magnetic flux trapping, it is worth pausing a moment to revisit the background magnetic flux mitigation strategies of both facilities. The MSU/FRIB vertical test dewar is equipped with passive magnetic shielding, and this, along with meticulous electrical isolation of the cavity from its support fixture to combat any thermoelectric currents, achieved the results of the previous chapter. In addition to

passive magnetic shielding, FNAL also applies an active field cancellation method, in which Helmholtz coils are fitted directly on the cavity under test, as seen in Figure 5.3(a). The magnetic field in the dewar is monitored during cooldown, and the current in the coils is adjusted in an active control loop to ensure the measured magnetic field is minimized during the superconducting transition. This method is generally successful at achieving a background magnetic field of 1 mG or less.

Since the N-doped FRIB400 cavities were a) expected to be more sensitive to background magnetic flux and b) to be tested and compared in both vertical test facilities, we were motivated to devise a method for reducing the background magnetic field in the MSU/FRIB vertical test dewar to levels comparable those achieved by the active compensation method in the FNAL vertical test dewar. In the MSU/FRIB vertical test dewar, previous measurements and general intuition lead us to conclude the remaining background magnetic field inside the dewar was entering through the joint between the dewar lid and sidewalls. The simplest method to counteract this field source is to devise a method to cancel it in that same location: thus, 30 turns of wire were installed around the edges of the dewar lid, as shown in Figure 5.3(b). The current in these coils was adjusted until the cavity-installed fluxgate magnetic probe indicated the field at the cavity (center cell) had been minimized. We confirmed this was the case by performing another magnetic survey, with the cavity installed in the dewar, and cancellation coil active. The results of this survey are shown in Figure 5.4, which show substantial improvement over the previous magnetic field survey conducted in Chapter 4. We thus can state with some confidence that the magnetic field environment of the respective test dewars had minimal effect on the RF testing results.

In addition to magnetic field mitigation and electrical isolation of the cavity from its fixture, so-called "fast-cooldown" techniques were also implemented at both FNAL and MSU

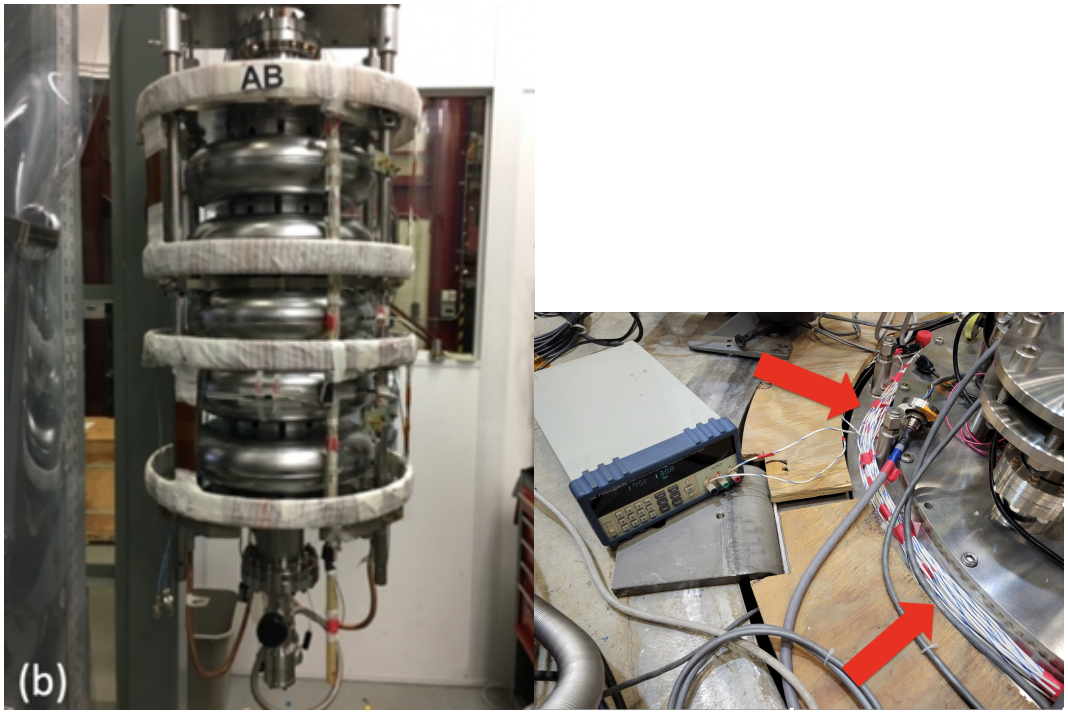

(a) (b)

Figure 5.3: (a) S65-001 644 MHz FRIB400 cavity after clean assembly to the vertical test insert at FNAL. The installed Helmholtz coils dynamically compensate the measured background magnetic field during cooldown, so field applied to the cavity is constrained to 1 mG or less for most tests. In both cases, the niobium cavity was electrically isolated from the titanium cavity fixture (support frame). (b) Installation of the MSU/FRIB dewar magnetic field cancellation coils (red arrows), shown with power supply.

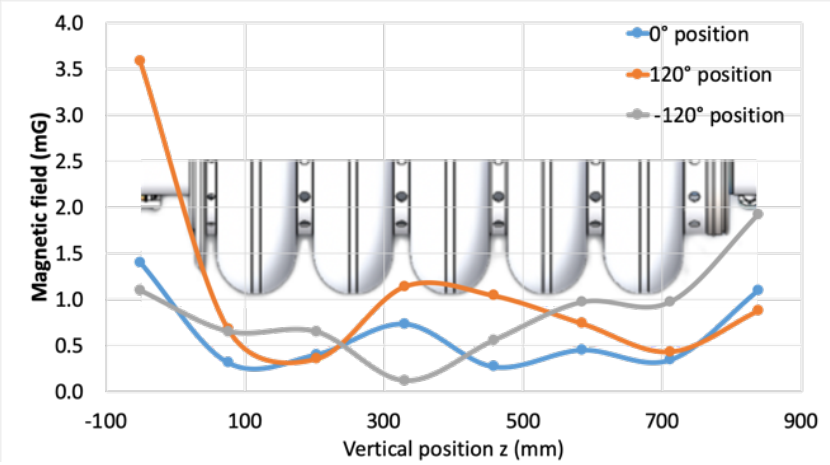

Figure 5.4: Magnetic survey of the MSU/FRIB vertical test stand (VTS) Dewar demonstrating efficacy of the MSU/FRIB field cancellation technique. A cartoon-cavity is overlaid to show approximately where the cavity equators lay in relation to the vertically scanned magnetic field in the Dewar at the three 120-degree offset positions.

to minimize trapped flux as previously discussed. Further discussion of the results of the fast cooldown method is reserved for after presentation of the RF results.

As stated, in the first N-doping of 644 MHz 5-cell elliptical $\beta = 0.6$ cavities, S65-001 underwent 2/6 doping followed by 7 μm cold EP. Initial RF testing at both MSU/FRIB and FNAL vertical test facilities showed the cavity experienced enhanced R_0, lowering Q_0 compared to the EP baseline, as seen in the blue set of points in Figure 5.5. After verifying that the cavity was subject to the same magnetic environment in both tests, we were left to conclude that the post-doping EP was not complete, and therefore elected to apply an additional 5μm of EP. Upon retesting, we found R_0 decreased by nearly 1 nΩ at the FRIB400 operating gradient, 17.5 MV/m, resulting in a Q_0 of 2.6×10^{10} at this operating gradient. The maximum gradient achieved was an impressive 29.5 MV/m, where the cavity ultimately quenched. Notably, field emission was entirely absent in this trial. Q_0 at this maximum gradient was 1.4×10^{10}. This second test occurred in a slightly enhanced background magnetic field compared to the first, which further supports the notion that the improvement in

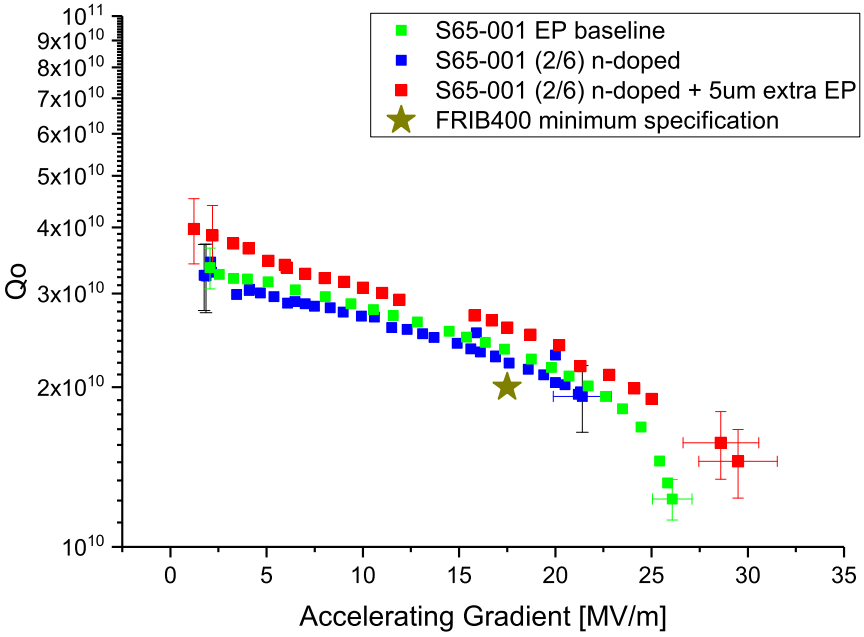

Figure 5.5: Q_0 vs E_{acc} results of the first 2/6 N-doping of FRIB400 prototype cavity S65-001. The green set of points is the baseline EP treatment, and the initial 2/6 N-doping is shown in blue, with somewhat decreased performance, likely due to incomplete niobium nitride removal in the post-doping EP step. After additional removal, the cavity was re-tested, yielding the red set of points, improving upon the baseline EP results. The error bars are shown on the first and last points for clarity, but are consistent throughout the data set.

R_0 was indeed due to more complete removal of the niobium nitride layer left over from the N-doping. Had the background magnetic field remained at exactly the same level between tests, we would have expected even greater improvement in R_0 reduction.

Cavity S65-002 underwent 2/0 N-doping at FNAL, followed by 7 μm cold EP. This cavity was initially tested in the FNAL vertical test dewar, which showed only a modest improvement over the EP baseline (Figure **??**). The cavity was then shipped to MSU/FRIB and retested in the dewar newly-equipped with the magnetic field cancellation coils. The cavity then achieved a record-setting Q_0 of 3.5×10^{10} at 17.5 MV/m. The cavity quench limit was reached at 22 MV/m, where the Q_0 was 2.8×10^{10}. While we await the opportunity

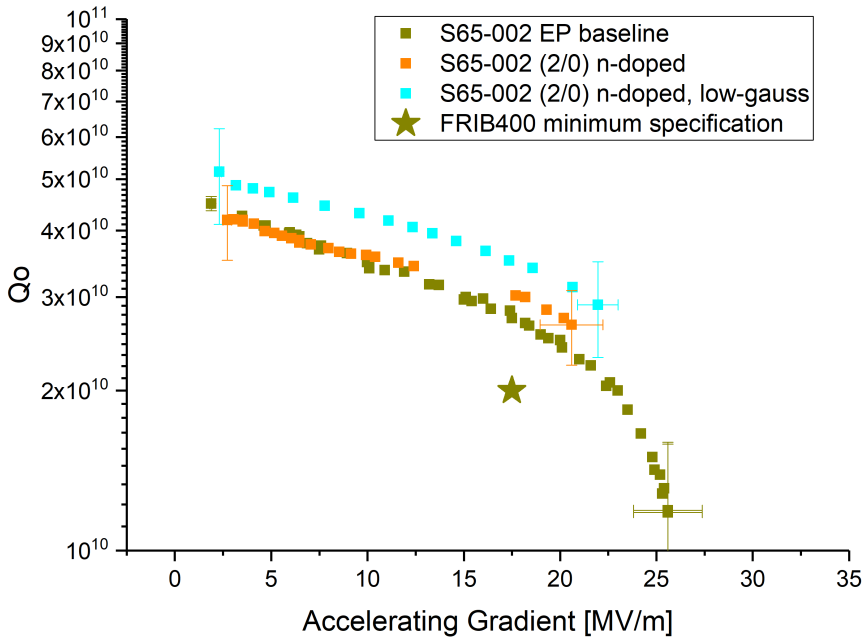

Figure 5.6: Q_0 vs E_{acc} results of the first 2/0 N-doping of FRIB400 prototype cavity S65-002. The EP baseline of the cavity (gold) was conducted at the FNAL vertical test facilities, as was the first test of 2/0 doping (orange). The second trial of 2/0 doping was tested at the MSU/FRIB facility with the magnetic field cancellation coils installed on the dewar lid, yielding by far the best results for this cavity, a Q_0 of 3.5×10^{10} at 17.5 MV/m.

to measure the flux sensitivity of the 2/0 N-doped 644 MHz medium-β cavity, sensitivities measured in 1.3 GHz N-doped cavities range from 1-5 nΩ/mG of trapped flux are typical [103], which again makes it possible for small variations in trapped flux to account for the difference in Q_0 measured between the two cavity trials.

We now pivot to focus more closely on the deconvolution of R_{BCS} and R_0 data, which is calculated from the Q_0 vs E_{acc} data as described in the prior section, shown in Figure 5.7. As expected, both R_{BCS} and R_0 exhibit field dependencies in all cases. R_{BCS} (Figure 5.7(a)) is highest in the EP-baseline treatments (green), with moderate slope in the mid-field range, until encountering the sharp upward bend of the high-field Q-slope onset around 20 MV/m. The 2/0 N-doping treatment reduces R_{BCS} the most, achieving well under 2 nΩ

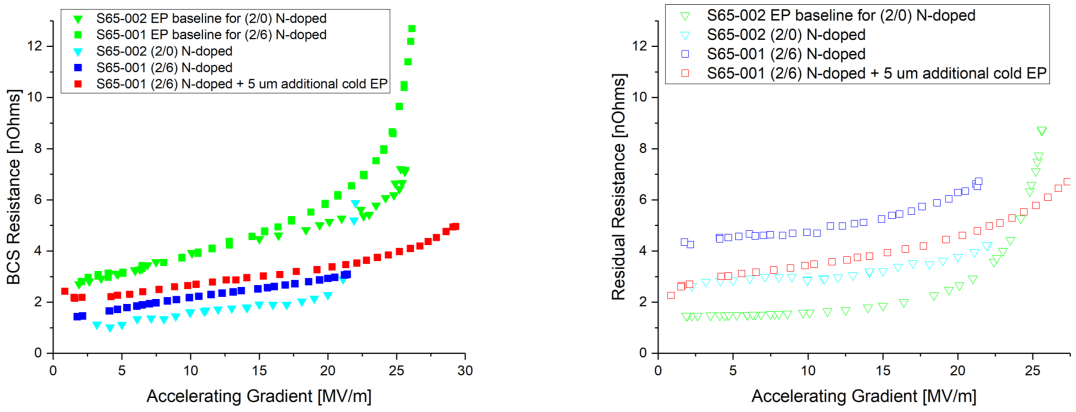

(a) (b)

Figure 5.7: R_{BCS} and R_0 deconvolution for EP baseline and all N-doping trials of the FRIB400 prototype cavities. (a) As expected, EP-treated cavities have the highest R_{BCS} at medium field, and N-doped cavities have the lowest. Additional 5 μm EP in the 2/6 doped cavity (12 μm total post-dope) slightly increased the R_{BCS}. For reasons that have yet to be fully explored, is not consistent with [110] in which additional 10 μm EP lowered RBCS in 2/6-doped cavities. (b) Residual resistance was highest in N-doped cavities and lowest in EP cavities.

at the operating gradient. 2/6 treatment has consistently elevated R_{BCS} compared to the 2/0 trial, which is significant in that R_{BCS} is a clear feature of the recipe under test (as opposed to R_0, which can be tricky to interpret given the effect of fast-cooldowns, magnetic environment, etc.). From R_{BCS} alone, the 2/0 recipe clearly appears to be the strongest candidate.

R_0 (Figure 5.7(b)) results align well with what we surmised from the Q_0 vs E_{acc} results. The initial 2/6 N-doping has clearly elevated R_0, which was reduced by the 5μm of additional EP. The 2/0 doping recipe had the lowest R_0 of the N-doped trials, but was still around 1 nΩ higher than the EP-baseline trials. As expected, N-doped 644 MHz cavities also seem to increase in sensitivity to trapped magnetic flux. A precise measurement of this increase in sensitivity awaits trial in the single-cell 644 MHz cavities.

A discussion of these results would incomplete without pausing to briefly address the

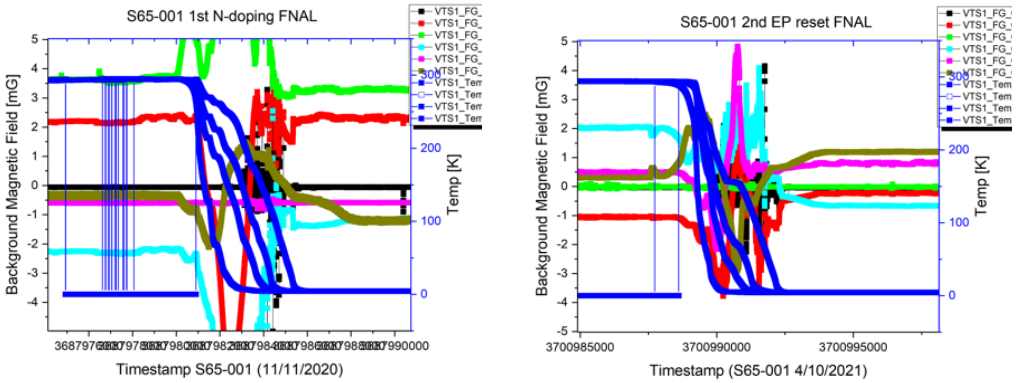

(a) (b)

Figure 5.8: Magnetic field traces overlaid with temperature traces for the (a) 1st 2/6 doping and (b) + 5 μm additional EP trial.

cooldown dynamics relevant to each vertical test, since the cooldown speed has been shown to affect cavity flux expulsion [112]. Representative time-series plots of cavity cooldown overlayed with measured magnetic field at various locations in the dewar have been selected for a few cases in which there was some question as to whether the background magnetic field was responsible for the cavity performance, or some other factor intrinsic to the cavity treatment was the cause of lowered (or increased) Q_0. As shown in Figure 5.8, the difference between the initial 2/6 doping and 2/6 doping with 5μm EP was not due to a decrease in the background magnetic field, or a significant change in cooldown speed. Since the background magnetic field was in fact slightly higher in the 2nd trial, we may conclude that it was the additional 5 μm of EP removal that lead to the improvement in Q_0, supporting our conclusion that insufficient EP removal lead to decreased N-doped performance in the 1st 2/6 N-doping trial of this cavity. This is further supported by the significant decrease seen in the R_0 after the additional 5 μm of EP removal, despite the somewhat enhanced background magnetic field.

In Figure 5.9, we find the background magnetic field in the vicinity of the cavity is

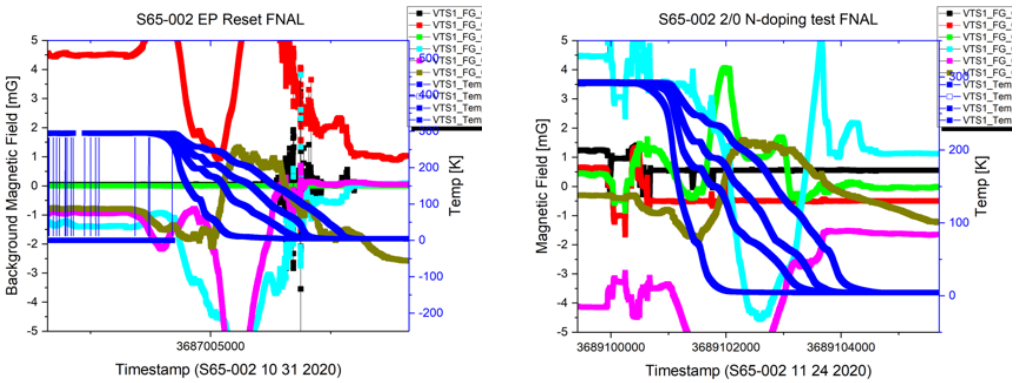

(a) (b)

Figure 5.9: Magnetic field traces overlaid with temperature traces for the (a) 1st and (b). 2nd N-doping trials of S65-002.

generally constrained to 1mG or less, and is fairly comparable between the two trials. In the associated Q_0 measurements at FNAL, the 2/0 N-doped cavity performance improves upon the EP performance, despite the expected increased sensitivity to background magnetic field and the slightly elevated levels of background magnetic field experienced in this particular trial. The subsequent test of this cavity at MSU/FRIB with a different method of field cancellation was more successful and lead to the very strong Q_0 vs E_{acc} performance, both confirming the increased sensitivity of the cavity to background magnetic field, and the success of the 2/0 N-doping recipe.

5.4 N-doping Conclusions

The ability of the 2/0 recipe to achieve a Q_0 of 3.5×10^{10} at 17.5 MV/m represents significant potential for advancement in further optimizing N-doping for the FRIB400 cavities. This cavity experienced quench at $E_{acc} = 22$ MV/m, or at a peak magnetic field of approximately 97 mT, which is comfortably above the FRIB400 operating gradient, 17.5 MV/m.

As anticipated, the anti-Q slope does not appear in this sub-GHz frequency cavity, although clearly N-doping remains capable of imparting significant benefit. The 2/0 recipe shows the best R_{BCS} reduction, with no significant increase in the medium-field Q-slope from either the 2/6 trial or the EP baseline.

Due to the tight tolerances of the N-doping post-doping EP step, the first attempted N-dopings of these FRIB400 644 MHz cavities also functions as a finer test of the modified EP tool and process. All EP-baseline trials surpassed the minimum FRIB400 design goal of $Q_0 = 2 \times 10^{10}$, and none suffered early quench, or other faults stemming from obviously poor EP. However, the results of the 650 MHz high-β study in the PIP-II prototype cavities, even adjusted for the scaling of a different geometry factor, indicate that we may well have expected even higher Q_0 than measured in these first trials.

Analysis of the EP conditions experienced by the PIP-II 650 MHz prototype cavities suggests that further optimization of the EP parameters to the 650 MHz may be possible. In particular, Chouhan et al., have experimentally identified an interesting relationship between the length of the doughnuts fitted onto the EP electrode and the voltage applied across the electrode and cavity required to reach the "plateau" region of the current-voltage ("I-V") curve in the medium-β 650 MHz 5-cell elliptical cavities for PIP-II: shorter doughnuts seem to require higher voltage to breach the polishing threshold (plateau region) [113]. In the case of initial EP treatments of PIP-II medium-β 650 MHz 5-cell elliptical cavities, the shortened electrode, coupled with 18 V of applied voltage was not adequate reach the polishing threshold. In the case of the FRIB400 cavities, using the longer doughnut shape, 18 V was much closer to the polishing region, but not firmly in it. Recent upgrades made to the ANL EP facility in light of this finding have increased the voltage available to these EP treatments. Applying higher voltage to the EP treatment step in future has the potential to

produce an even smoother surface, and improve subsequent N-doping outcomes.

We find, as expected, that the residual resistance (R_0) was the strongest limiting factor for Q_0 in the N-doped cavities. The principal culprit responsible for the increase in R_0 is most likely the N-doped cavities' increased sensitivity to flux trapping. Broadly, there exist two options for addressing cavity performance degradation resulting from magnetic field trapping: 1. prevent background magnetic field from being present in the first place (i.e., improving magnetic hygiene), and 2. improve the cavity's ability to expel magnetic field during the superconducting transition.

The efficacy of fast-cooldowns at promoting flux expulsion means that method tends to draw the most technical attention, however, the more cost-effective strategy is to simply reduce or eliminate the background magnetic field in the cavity environment. To demonstrate the point, a "slow-cooldown" of FRIB400 cavity S65-001 was conducted, in the MSU/FRIB dewar equipped with the magnetic field cancellation coils. Despite being cooled so slowly that no thermal gradient existed along the length of the cavity, the RF performance of the cavity was not significantly diminished. This serves as a proof-of-principle that, when thinking forward to the possible implementation of these or similar higher-sensitivity cavities in the context of a FRIB400 cryomodule, successfully reducing the background magnetic field can effectively replace the need to design and implement costly, or at least, very resource-intensive, fast-cooldown capabilities.

To conclude these preliminary studies in N-doping, the technically complex process of adapting the 2/6 and 2/0 recipies with EP modifications to the FRIB400 prototype medium-β 644 5-cell elliptical cavity design were moderately successful, and indicate promising avenues for further improvement, namely by improving the EP step, and ensuring consistently successful background field mitigation. Though 2/6, 2/0, and 3/60 doping recipes cover a

very small number of the possible doping recipes, the results from these recipe trials, and growing understanding of the mechanics of nitrogen diffusion, allow us infer that even minor changes in X/Y are unlikely to yield dramatically better results, and thusfar 2/0 seems a reasonable optimum, even across multiple frequency ranges.

5.5 Furnace-baking

Furnace-baking, in which a cavity is baked in a vacuum furnace for a few hours at so-called "medium" temperatures of 300-500°C (which occupies the region between "low" temperature baking around 120°C, and "high" temperature baking around 800°C and upwards) evolved somewhat ironically from efforts to shield the cavity inner surface from possible contaminants in the furnace environment. Nitrogen "infusion" type recipes, which introduced nitrogen at a lower temperature into the vacuum furnace in an attempt to avoid niobium nitride precipitation and thus avoid post-doping EP [114], turned out to have low repeatability across institutions, likely because the lack of post-baking chemical treatment made the treatment highly sensitive to the specific vacuum furnace in which it was performed [115]. In an attempt to isolate the cavity under treatment from the vacuum environment in which it was treated, Posen et al. [115] developed a method of heat-treating cavities *after* assembly to the test fixture, ensuring the inner surface of the cavity became an entirely controlled environment, independent of the specific vacuum furnace used for the heat treatment. This in-situ medium-temperature baking (eventually dubbed mid-T baking) method then allowed focused study of the function of the oxide layer that develops on the cavity surface after exposure to air. Namely, it enabled the cavity to be baked at temperatures that would dissolve and dissolute the oxygen layer on the cavity surface, then tested without exposure

to air, preventing the formation of the oxide layer after the heat treatment.

Posen et al. found that such a method of dissolving and diffusing the oxide layer without allowing it to regrow lead to high-Q_0 performance in 1.3 GHz cavities. R_0 and R_{BCS} were both significantly reduced, relative to EP cavities, but even more remarkably, R_{BCS} was *reversed* some cases, meaning that, without N-doping, an anti-Q slope appeared! On the basis of SIMS data showing an increase in the niobium nitride (NbN) signal after Mid-T bake, Posen et al. suggest this N-doping like modification of R_{BCS} may be due to environmental N having got into the cavity, possibly degassed from components in the Mid-T baking apparatus. However, they also note that the dissolution and diffusion of the oxide layer into the niobium bulk can result in interstitial oxygen, which, similar to interstitial nitrogen, could alter the mean free path and thus also possibly induce the reversal in field dependence of R_{BCS} [115]. Suffice it to say, no definitive mechanism responsible for the reversal in R_{BCS} dependance is offered at this juncture. With somewhat more confidence, the R_0 reduction was related to the dissolution of the Nb_2O_5 oxide [115].

While Mid-T baking is highly useful in the course of furthering our understanding of fundamental SRF science, it is difficult to imagine a scenario in which constructing an actual linear accelerator with Mid-T baked cavities without ever exposing their inner surfaces to air would ever be practical. When re-exposing the Mid-T cavities of the initial study to air, Posen et al. found that the record Q_0 performance was degraded somewhat, reverting to levels more characteristic of N-doping in these cavities. HF rinsing was found to rescue the performance somewhat, but not return it to the original high-Q_0 prior to air exposure [115].

Still, the relative simplicity of the treatment and potential for Q_0 gains prompted some laboratories to try Mid-T-like treatments (in terms of temperature and duration) in in their vacuum furnaces, naming the process "furnace baking" to distinguish it from the *in situ*

Mid-T baking studied by Posen et al. To be explicit, in furnace baking, the initial oxide layer is dissolved and diffused into the bulk niobium during vacuum furnace baking, but unlike Mid-T baking, it is allowed to reform once the cavity was removed from the furnace and exposed to air. Similar to N-doping, initial explorations of this phenomena have been necessarily experimental, with no clear theoretical guidance available.

In the first of these studies, Ito et al., working with single-cell 1.3 GHz TESLA cavities trialled 3 h furnace-baking treatments ranging from 200°C to 800°C and find that 300°C 3 h furnace-baking produced very high Q_0, of over 5×10^{10} at 16 MV/m [91]. This Q_0 is a little lower than, but still comparable to, the results of Posen et al., who reported Q_0 of 5×10^{10} at 20 MV/m in the same cavity type [115], without air exposure. Remarkably, the 3 h 300°C furnace-baked 1.3 GHz cavity also exhibited an anti-Q slope.

In an attempt to further elucidate the functional mechanism responsible for the furnace-baking effect, Lechner et al., [116] embarked on a focused niobium coupon study. Flat, niobium coupon samples were subjected to various furnace-baking treatments, and then analyzed in SMIS to determine the near-surface depth profile of various ion species. Benchmarking the data against Ciovati's model for oxygen diffusion (Fick's law of diffusion with a source) [117],

$$\frac{\partial c(x,t,T)}{\partial t} = D(T)\frac{\partial^2 c(x,t,T)}{\partial x^2} + q(x,t,T) \tag{5.12}$$

which models the (one-dimensional) diffusion of oxygen from the finite oxide layer into a niobium slab. The solutions to this equation can then be split into the portion that describes the initial distribution of oxygen in interstitial spaces, and the portion that describes the oxygen introduced due to the oxide dissolution. These pieces function as a linear combination,

vis. $c(x,t,T) = v(x,t,T) + u(x,t,T)$ [116], and can be solved:

$$v(x,t,T) = \frac{v_0}{\sqrt{\pi D(T)t}} e^{-x^2/(4D(T)t)} + c_\infty \tag{5.13}$$

and

$$u(x,t,T) = \frac{u_0}{\sqrt{\pi D(T)t}} \int_0^t \frac{k(T)e^{-k(T)s}}{\sqrt{t-s}} e^{-x^2/(4D(T)(t-s))} \tag{5.14}$$

the group finds convincing evidence that oxygen, not nitrogen, is primarily responsible for the furnace-baking effect. Using their data to quantify v_0 and u_0 they align Ciovati's model for oxygen diffusion with their observations [116] and thus propose their model for oxygen diffusion, with their new parameters, which can be used to 'tune' the furnace baking procedure to achieve specific electron mean free paths. If one could theoretically determine the optimum mean free path for a given cavity and given frequency range, the reasoning goes, one can then simply calculate from the oxygen diffusion model what temperature (T) and duration (t) of furnace baking will achieve that mean-free path [116]. While the theoretically optimum mean free path remains an unknown in the case of 650 MHz cavities, this remains an enticing tool in the effort to optimize furnace baking.

5.5.1 The Role of Oxygen

The increasing interest in the role of oxygen in the furnace-baking treatment merits a few more words.

Intriguingly, Wenskat et al. [118] find evidence that, in the case of the diffusion of oxygen into the bulk niobium, hydrogen-vacancy complexes, which act as nucleation cites for lossy sub-surface niobium-hydrides, get preferentially replaced by oxygen-vacancy complexes. This is a near complete analogue of the proposed role of nitrogen by Romanenko et al., in N-doped

cavities [95]. The oxygen-vacancy complexes prevent the formation of the niobium hydrides, which reduce R_0 at higher fields. This idea has been further corroborated in recent work by Bafia et al. [119]. Furthermore, [118] explore the substructure of the oxide layer, which consists not of a single niobium-oxide species but several. The hypothesis is the lattice mismatch between each subsequent layer of differing oxide species contributes to the RF resistivity of that layer, and dissolving and allowing the oxide layer to regrow restructures the oxide layer to an effectively lower-energy state in which the lattice mismatch between layers is diminished [118]. This adds weight to the finding that, despite allowing the oxide layer to regrow, most trials at 1.3 GHz find that furnace baked cavities retain a significant fraction of the performance measured in trials in which the oxide layer is not allowed to re-form.

We close this section by emphasizing an enigma that has emerged in comparison of N-doping with furnace baking: N-doping requires relatively high temperatures (800°C) to diffuse nitrogen into the RF layer of the cavity where it modifies the mean free path length and R_{BCS} (and R_0), whereas furnace baking requires just $300°C$ to diffuse oxygen into the RF layer of the cavity. SIMS studies have found the effective diffusion depths of these elements are slightly different. While the circumstances of this difference can reasonably stem from different diffusion coefficients between N and O in the niobium crystal lattice, where the diffusion coefficient of N is two to three orders of magnitude smaller diffusion coefficient than O [116], the effect on the Q_0 of the cavity remains puzzling, and, as such, functions as an invitation for future study, which promises to deepen our understanding of the fundamental physics being manipulated by the presence of interstitial O or N [98].

5.5.2 5-cell RF testing results

Prior to furnace baking, S65-001 was EP-reset with 60 μm, with the final 10 μm being cold EP. The cavity was re-tested, resulting in a higher EP baseline performance than the previous EP baseline used for the 2/6 doping. The first EP trial at the MSU/FRIB vertical test facilities encountered 2.2 nΩ of R_0 at $E_{acc} = 2$ MV/m, fitted as described from the R_s vs T measurement. This second EP trial had approximately 1.7 nΩ of R_0 at $E_{acc} = 2$ MV/m, constituting a difference in Q_0 of nearly 27%. At higher fields, this difference grows closer to 20%. To anticipate the next chapter somewhat, in which we measure that the EP 644 MHz cavity has a flux sensitivity of 0.45 $n\Omega/mG$, this difference in R_0 corresponds roughly to 1 mG of increased background magnetic field between the trials, which is entirely believable given that the first EP trial was conducted in the MSU/FRIB dewar prior to implementing the field cancellation coils described earlier. To wit, there is no strong evidence that the 2nd EP baseline resulted from an incomplete reset procedure, or is influenced by the results of the previous study, despite the observed increase in Q_0.

The subsequent furnace baking treatment of S65-001 was straightforward: a 300°C 3-hour bake was conducted in a high-vacuum furnace at FNAL, followed by high-pressure water rinsing (HPR) at the ANL facilities. Clean assembly to the test insert was then conducted at FNAL. The Q_0 vs E_{acc} results are shown in Figure 5.10. At first glance, the performance of the furnace baking treatment is underwhelming: no appreciable difference between the EP baseline and the furnace baking treatments is apparent. Only upon examination of the R_{BCS} and R_0 breakdown do they become differentiable: In Figure 5.11(a) and (b) it is clear R_{BCS} was reduced but R_0 increased by nearly equal amounts, washing out any improvement in Q_0, at least, at 2 K.

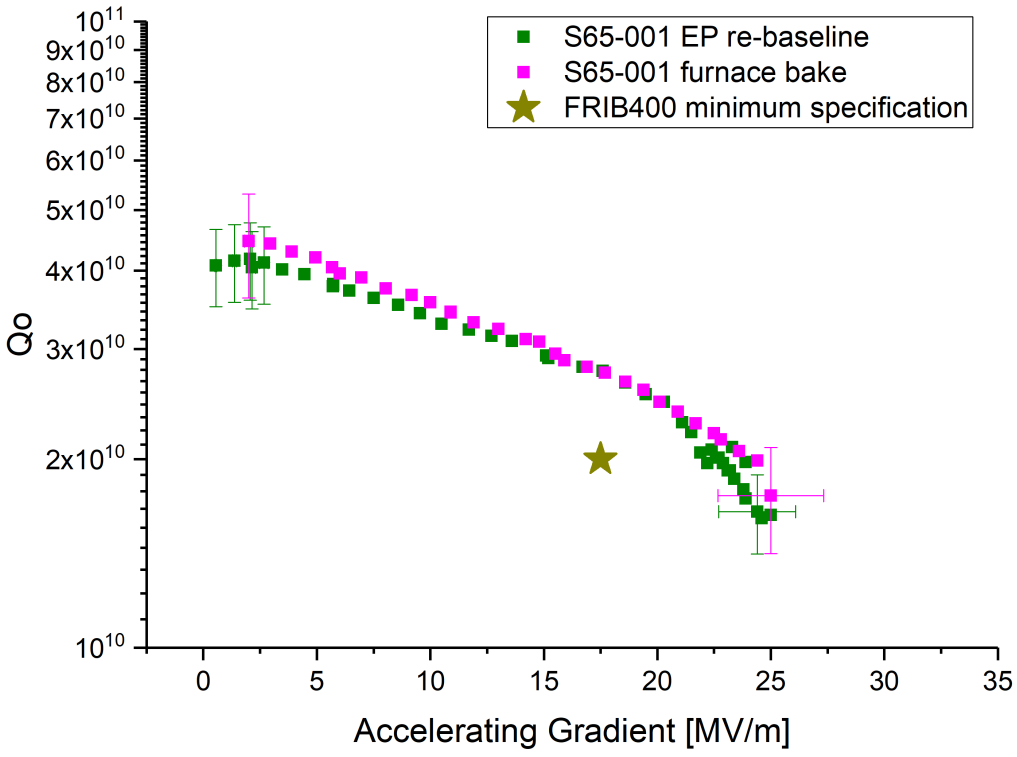

Figure 5.10: FRIB400 prototype cavity S65-001 furnace baking Q_0 vs E_{acc} curves.

While the furnace baking improved upon the 2/6 N-doped results, decreasing R_0 by 19% and only increasing R_{BCS} by 7.5%, it did not significantly elevate the Q0 performance above the immediately prior EP baseline performance. However in the deconvolution of R_{BCS} and R_0 (Figure 5), it is apparent that furnace baking decreased R_{BCS} and increased R_0 in equal, opposite proportions compared to the EP baseline. This overall suggests that preference for N-doping or furnace baking would be dependent on the target operating temperature of the prospective system, with higher-temperature systems possibly preferring N-doping since they are subjected to more losses due to the temperature-dependent R_{BCS}, and the lower-temperature systems may prefer furnace baking, since elevated R_{BCS} would not be a detriment to their performance at low temperatures.

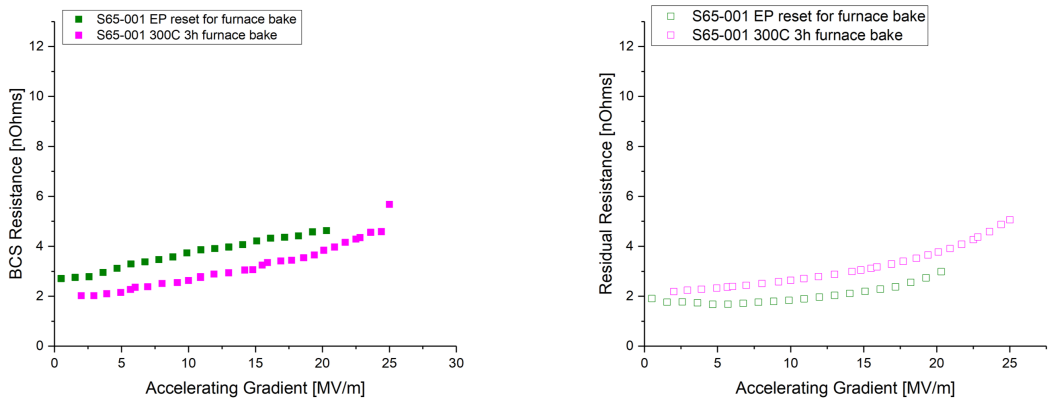

(a) (b)

Figure 5.11: Deconvolution of R_0 and R_{BCS} for the furnace-baking EP baseline trial (green) and the 3 h, 300°C furnace baking trial (magenta). While no major gains in Q_0 performance were seen, the different becomes apparent here: furnace baking decreased R_{BCS} and increased R_0 compared to the EP baseline. Fractionally, this tradeoff was quite balanced, so the furnace baking effect was masked in the Q_0 v E_{acc} representation.

5.6 Single-cell RF testing results

Single-cell cavities are very useful tools for superconducting RF surface treatment research and development projects. These smaller, simplified structures are substantially easier to clean and handle, providing a minimally viable format in which to explore the potential of new RF surface treatments at different frequencies, and iterate treatment parameters relatively quickly. Additionally, single-cell cavities enable more accurate measurement of cavities' sensitivity to trapped magnetic flux, and flux expulsion properties. While we leave in-depth discussion of flux expulsion properties to the material studies of Chapter 6, the recent availability of a single-cell FRIB400 644 MHz $\beta = 0.6$ cavity (S65-903), shown in Figure 5.12, enabled further exploration of the furnace-baking treatment, which we address here.

After receipt of cavity S65-903 from the manufacturer, it underwent tuning, hydrogen

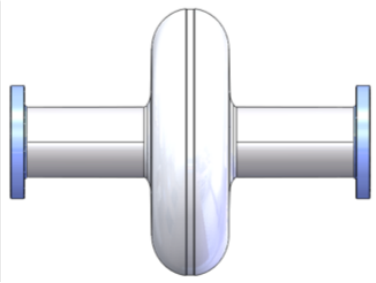

Figure 5.12: Drawing of FRIB400 prototype 1-cell cavity.

degassing, and bulk EP, just as its 5-cell counterparts did. The cavity was then baseline tested twice: First immediately after the final cold EP treatment, then after a 900°C 3h annealing treatment, which was part of a concurrent flux expulsion study, treated more fully in Chapter 6. We then elected to use a 330°C 3h furnace bake to explore the notion that a slightly higher temperature treatment could ameliorate the increase R_0. While the results of Ito et al. show this may also increase R_{BCS}, it is possible this gain can be more than offset by a sufficient reduction in R_0 [91]. The results from all three RF tests of S65-903 appear in Figure 5.13.

The 330°C 3h bake resulted in a 16% improvement in 2 K Q_0 at 17.5 MV/m over the baseline 900°C annealed performance, achieving Q_0 of 3.6×10^{10} at 17.5 MV/m. In the deconvolution of R_{BCS} and R_0 shown in Figure 5.14, we find this improvement in Q_0 over the 900°C baked baseline EP performance was due to the strong decrease in R_{BCS}, as had been expected from previous studies. The R_0 was increased somewhat over the 900°C baked baseline EP trial, and the nature of the field dependence appeared to be somewhat altered: At low-field, the two trials had quite similar levels of R_0, around 1.3 nΩ, however as field increased, the R_0 measured in the 330°C 3 h furnace baking trial increased more rapidly and more linearly, suggesting another mechanism contributing to R_0 had gained some prominence.

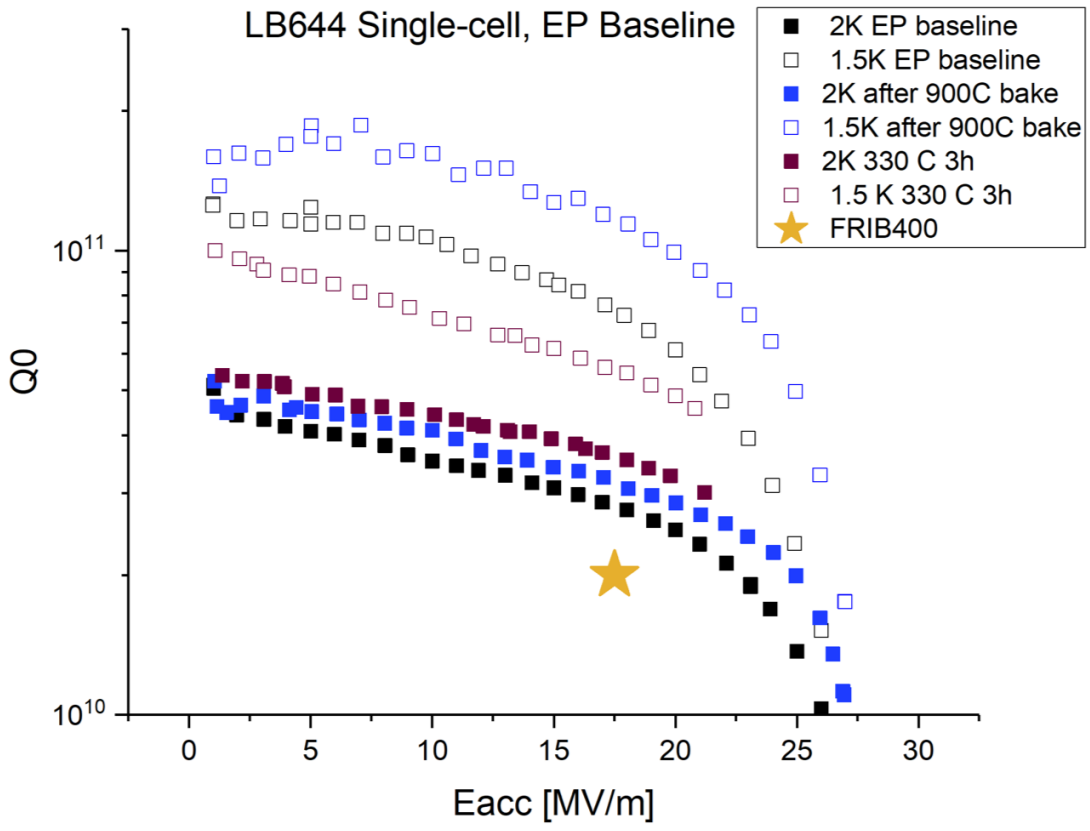

Figure 5.13: FRIB400 prototype 1-cell cavity S65-903 furnace baking Q_0 vs E_{acc} curves.

Recalling the discussion of the role of oxygen and the oxide layer in furnace baking treatments, it seems possible that an alteration of the oxide layer structure as it regrew after the furnace baking treatment could have elicited the change observed in R_0. There is not yet sufficient evidence, either in the literature or in our own research, to support a clear consensus on exactly how detrimental the existence of the oxide layer is. Yet, our result here showing the change in R_0 in the case of cavity S65-903 indicates it may be interesting to try a procedure such as hydrofluoric (HF) acid rinsing. HF rinsing functions by dissolving the few-nm thick niobium oxide layers, and does not react with the bulk niobium itself. After the HF rinse, conducting a water rinse on the cavity surface regrows the oxide layer, which consumes

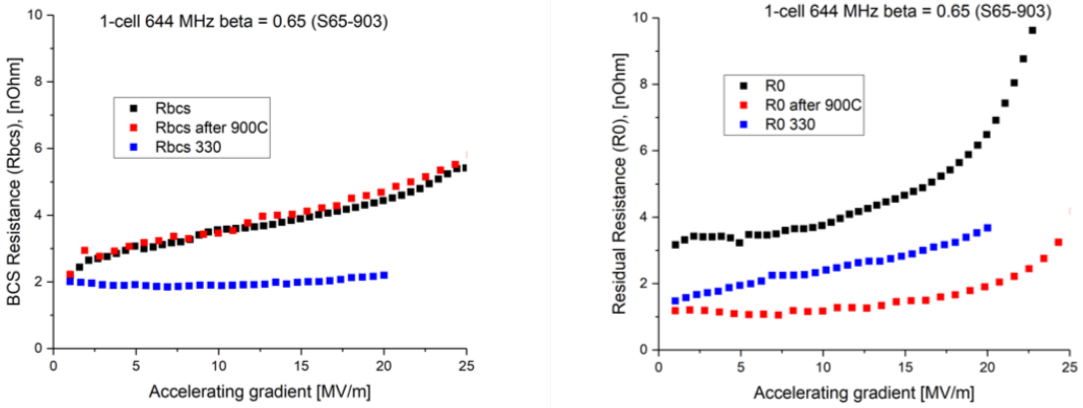

(a) (b)

Figure 5.14: Deconvolution of R_0 and R_{BCS} showing the effect of 330°C baking on each of these quantities in the 644 MHz single-cell prototype medium-β cavity. As expected, R_{BCS} is decreased significantly after the medium-temperature baking treatment, and the faintest hint of a reversal in field dependence of R_{BCS} also appears between 1 and 5 MV/m (a). Residual resistance is increased after the baking treatment (b).

a few more nm of the bulk Nb, resulting in an overall removal of 1-2μm [120] throughout this process. In addition to this highly controlled Nb removal, some circumstantial evidence from other cavity tests here at Fermilab has suggested that some reordering of the oxide layer may be taking place, and regrowing with a less lossy lattice structure. This cavity is in a prime state to test this hypothesis in the coming months.

5.6.1 Sensitivity measurement

Single-cell cavities enable precise magnetic flux sensitivity measurements, which are of critical interest in the present context of exploring advanced RF surface processing techniques that, while improving the cavity Q_0, may also cause increased magnetic sensitivity in a cavity treated thusly. In the highly controllable magnetic field environment of the vertical testing dewar, the focus is generally on the best-case performance of the RF surface preparation under test. However, if the cavity performance gains come at a large cost in terms of cavity

sensitivity S, even if the effect can be successfully mitigated in the vertical testing dewar, increased S remains a risk factor in suboptimal cavity performance in the cryomodule.

Direct measurements of cavity sensitivity to trapped flux, S, are made by fitting Helmholtz coils to the single-cell cavity as depicted in Figure 5.15a. While the cavity is above the superconducting transition temperature of niobium, $T_C = 9.2$K, current is run through the Helmholtz coils, imposing a known amount of magnetic flux on the cavity, measured by a fluxgate magnetic probe mounted on the cavity equator. The cavity is then cooled very slowly through the transition temperature, ensuring maximal flux trapping occurs. The Q_0 vs E_{acc} curves are then taken at 2 K and at 1.5 K, and the subsequent deconvolution of R_0 from R_{BCS} is used to determine how many nΩ of surface resistance was gained by the cavity due to the known quantity (generally 10-20 mG) of applied flux. Plotted in terms of nΩ/mG, we find a roughly 3-fold increase in S after the furnace baking treatment, as shown in Figure 5.15b. A slight field dependence also emerges, resulting in a 3.5-times increase in S at 17.5 MV/m.

An increase of 3.5x in S should give project leaders pause. In this particular case, we have improved Q_0 by only 16%, while opening the cavity to a risk that degrades Q_0 by 25% *per* nΩ of trapped flux. While the aim is always to minimize background magnetic flux in the cryomodule context, in reality, we must acknowledge the practical difficulties of doing so. This test was conducted in less than 1 mG of background, and, while field mitigation strategies are certainly in place in all cryomodules, expecting these to achieve 1 mG or less at the location of the cavities in operation may prove unrealistic.

For reference, current specifications for the baseline FRIB linac call for 15 mG or less inside the cryomodules, and LCLS-II, with their N-doped cavities, specified 5 mG. Reducing the worst-case field limit in the cryomodule context by an order of magnitude clearly merits

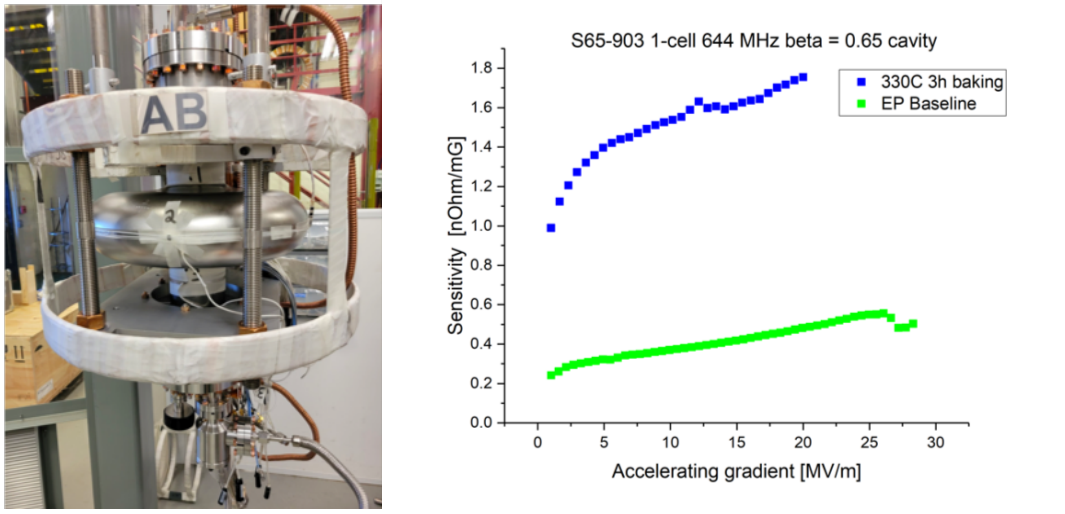

(a) (b)

Figure 5.15: (a) Photograph of the 644 MHz 1-cell cavity experimental setup for measuring flux expulsion/sensitivity. The Helmholtz coils (AB) are used to impose magnetic field on the cavity during slow cool-down. (b) Sensitivity (measured in nΩ/mG), is greatly increased after the furnace-baking treatment.

some technical investigation at the very least before high-S recipes can be put forward with any measure of confidence.

To illustrate the point, and the impact of S on Q_0, Figure 5.16 plots the predicted Q_0 at the FRIB400 operating gradient, 17.5 MV/m, as a function of trapped flux (x-axis). The black line indicates the maximum specification of background magnetic field in the cryomodules. The differing values of S resulting from the previous measurement, (and compared to a similar measurement done on a 5-cell N-doped cavity), emerge as differing slopes in this plot.

Critically, these differing slopes give rise to two regimes: 1, indicated by the circle, in which N-doping and furnace baking provide higher Q_0, *provided* that the cavities can be *guaranteed* to trap no more than around 1 mG. If it is not possible to guarantee this degree flux expulsion consistently across a production run of 55 cavities, we enter the regime in

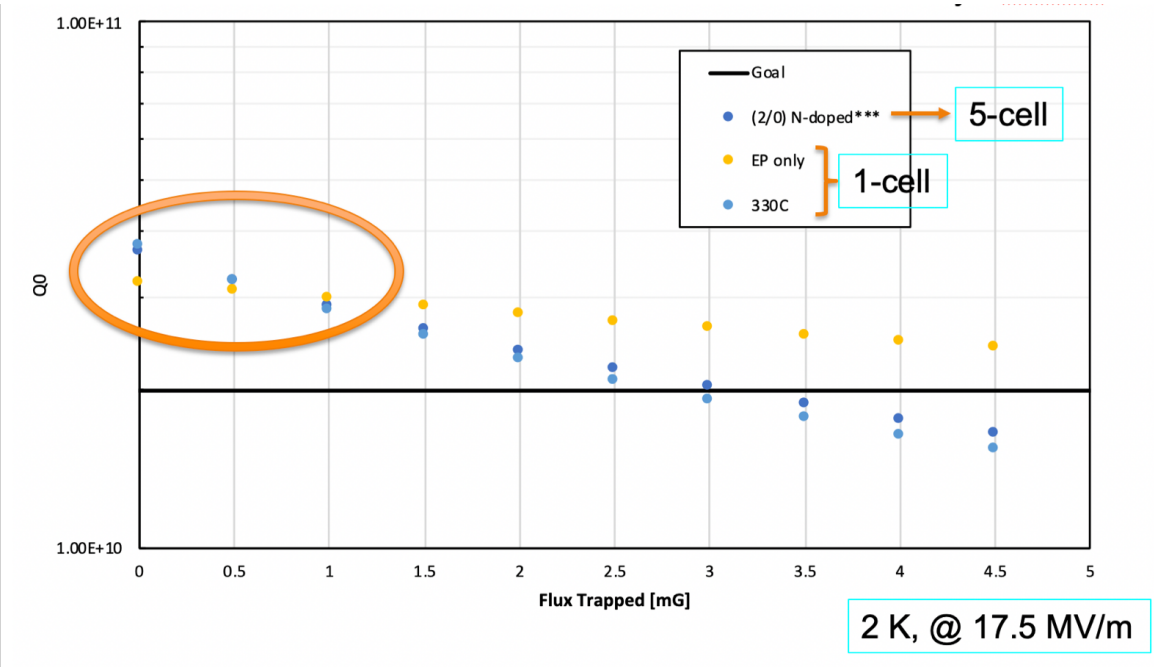

Figure 5.16: FRIB400 prototype 1-cell cavity S65-903 furnace baking Q_0 vs E_{acc} curves.

which EP cavities perform better than the advanced-treatment cavities due to their lower S values.

This result foreshadows the interest in causes and mitigations of flux trapping, which are investigated in earnest in the next chapter.

5.7 Furnace Baking conclusions

As in the case of N-doping, the furnace-baking did not elicit the anti-Q slope sometimes seen in furnace-baked 1.3 GHz cavities. 3h, 300°C furnace baking achieved the lowest residual resistance, R_0, of the advanced techniques, however R_{BCS} was somewhat elevated compared to the N-doped cavities. While this work deals primarily in 2 K applications, it is worth noting that, even without further optimization, furnace baking's low R_0 can be of legitimate value to applications operating in low-temperature ranges. Around 1.5 K and below, R_{BCS}

becomes negligible, and the relative simplicity of furnace baking may make it the more attractive option in this range.

Though furnace baking did not achieve the highest Q_0 of this study, in light of the work by Wenskat et al. [118] cited in the introductory section, it seems likely that more fruitful areas of this parameter space remain to be explored. Moreover, recent work in 1.3 GHz *in situ* mid-T baked cavities suggests that aspects of the R_{BCS} field-dependency may be a function of oxygen diffusion depth in the RF layer [119]. This implies it may well be beneficial to explore different furnace-baking temperatures and durations, and thus different diffusion depths of the oxygen, in the 644-650 MHz operating frequency range. Further experimentation with HF rinsing furnace-baked cavities may also prove beneficial, given the treatment's interaction with the oxide layer, and the possibility that the reformation of the oxide layer in different environments may lead to different properties in R_S.

Furnace baking measurably increases the sensitivity of the cavity, focusing some concern on the achievable levels of background magnetic flux mitigation in the cryomodule context. An important next step will be conducting a 2/0 N-doping of the 644 MHz 1-cell, and measuring the resultant (presumed) increase in S from that treatment. The comparison of the relative enhancements in S will be important in guiding the decision between pursuit of N-doping or furnace baking.

5.8 Advanced Techniques conclusions

With the aim of identifying promising SRF surface preparations to further develop as the proposed SRF surface treatment for the $\beta = 0.6$ 644 MHz 5-cell elliptical FRIB400 upgrade cavities, we have used this chapter to assess three 'advanced techniques' : two flavors of N-

doping (2/6, and 2/0) and two flavors of furnace baking (300°C, 3h in the 5-cell cavity and 330°C, 3h in the single-cell cavity). 2/0 doping, with 7μm post-doping EP, with background magnetic flux constrained to 1 mG or less, produced the highest Q_0 of 3.5×10^{10} at 17.5 MV/m, and quenched at 22 MV/m, with a Q_0 of 2.8×10^{10}. This treatment succeeded in reducing R_{BCS} to the lowest level of all treated cavities, about 2 nΩ. The R_0 of this background magnetic field-limited trial was 3.2 nΩ. Furnace baking, a substantially simplified procedure, achieved a Q_0 of 2.8×10^{10} at 17.5 MV/m, with 3.4 nΩ of R_{BCS} and 3.4 nΩ of R_0. Moving forward, we hypothesize further optimization of EP parameters could improve on both the N-doping and the furnace baking results.

While 2/0 N-doping certainly emerges from this study as the strongest candidate for further optimization, it would be premature to dismiss furnace baking entirely: too many unexplored avenues to improving this treatment for FRIB400-like cavity styles remain. Further optimizing the EP, in addition to exploring innovations such as HF rinsing, as our understanding of the role of oxygen in the RF layer improves, all could deliver the performance gains that would significantly improve furnace baking's candidacy for the FRIB400 proposed high-Q_0 treatment. From a production standpoint, the need to very finely control the large number of relatively complicated steps involved with N-doping introduces substantially more risk to any linac construction project than the implementation of furnace baking would. Avoiding these sorts of production challenges by choosing to furnace bake the cavities instead could be well worth the additional time and resources dedicated to further exploring the furnace baking parameter space. In particular, HF rinsing, and other methods of addressing the increased R_0 or S in this treatment shape our primary focus.

We close this chapter on a somewhat triumphant note, with a best-of summary. In Figure **??**, we show the best EP, N-doped, and furnace baking recipe Q_0 vs E_{acc} curves, all of which

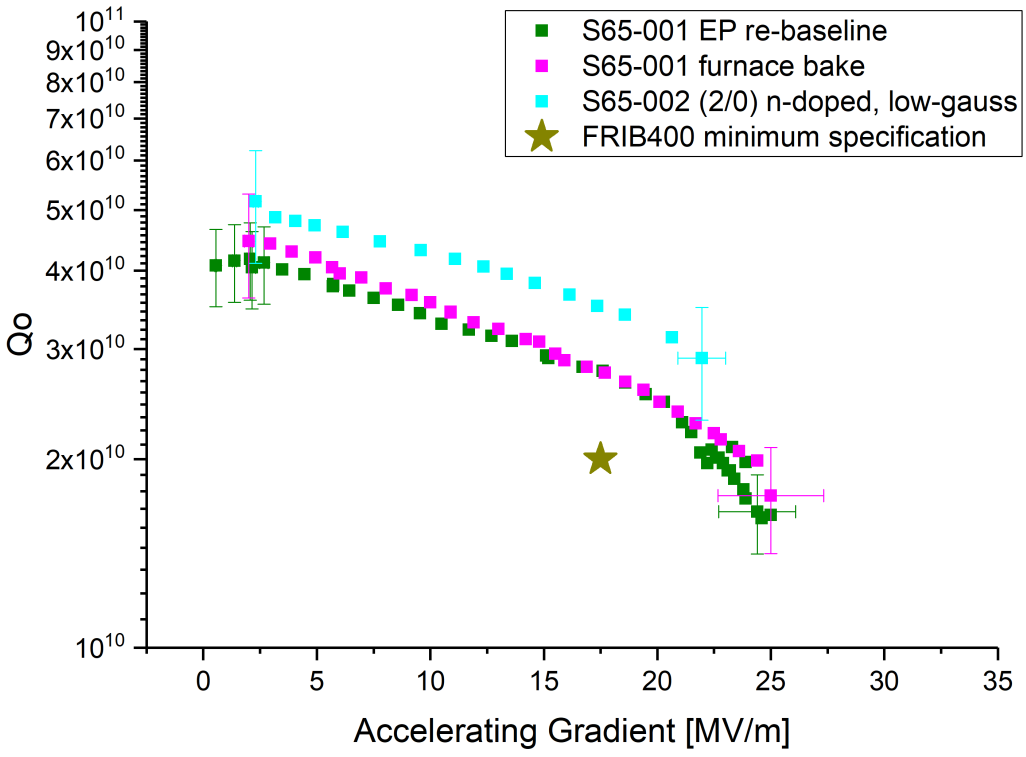

Figure 5.17: Best-of results of EP, N-doping, and 300C 3h furnace baking tests in the 5-cell, FRIB400 prototype cavities.

show substantial improvement over the FRIB400 minimum design goal for Q_0 and E_{acc}.

The associated deconvolution of R_0 and R_{BCS} of the best-of curves are presented in Figure **??**.

And finally, a reference table below notes, in descending order, Q_0 achievements, ordered by Q_0 at the FRIB400 gradient, 17.5 MVm (Table 5.1).

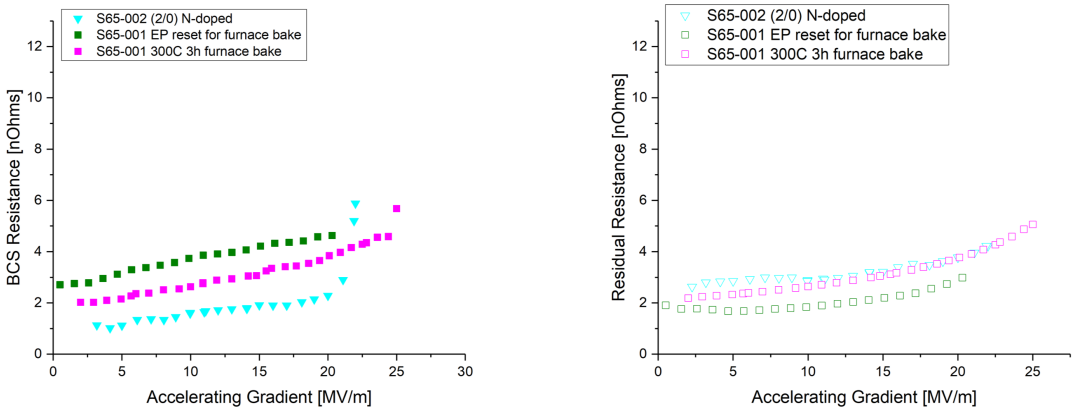

(a) (b)

Figure 5.18: (a) R_{BCS} and R_0 deconvolution for the best-of summary of FRIB400 cavity performance. Note the 2/0 N-doping achieves the lowest R_{BCS} but has relatively elevated R_0, most likely due to increased sensitivity to trapped magnetic flux.

Table 5.1: Summary of FRIB400 $\beta = 0.6$ 644 MHz 5-cell elliptical cavity RF tests

Treatment	Q_0 at 17.5 MV/m	Max Gradient	Q_0 at Max Grad.
2/0 N-doping	3.5×10^{10}	22 MV/m (quench)	2.8×10^{10}
300°C 3 h baking	2.8×10^{10}	22 MV/m (quench)	2.9×10^{10}
EP (re-baseline)	2.7×10^{10}	25.5 MV/m (admin limit)	1.2×10^{10}
2/6 N-doping	2.6×10^{10}	29.5 MV/m (quench)	1.4×10^{10}
EP (1st)	2.3×10^{10}	26 MV/m (amp limited)	1.2×10^{10}

Chapter 6

Bulk Nb properties material study

The study of superconducting RF cavities lives at a fascinating–sometimes, confounding–intersection between quantum-scale phenomena and macroscopic metallurgical properties. On the one end of the scale, we model and calculate single-vortex pinning dynamics under RF fields, the scattering of cooper pairs, and the energy states of quasiparticles. On the other end, we cast ingots of niobium, from which pieces are cut, cold-worked, deep drawn, (or spun), e-beam welded, and so-on. In this chapter we attempt to align some of the macroscopic properties of the metal, niobium, with what we can calculate from first principles, or measure in the RF testing Dewar, with the aim of better controlling and optimizing cavity production processes.

6.1 Flux expulsion in Nb cavities

In the course of introducing the concept of cavity sensitivity to magnetic flux, S, Chapter 5 belabored the various loss mechanisms of magnetic flux, namely, the reactive losses in the flux-pinning regime and the viscous drag of the flux-flow regime, with some peak of sensitivity in the transition region between these two regimes [90]. To wit, we have a reasonable understanding of *why* magnetic flux trapping is detrimental to cavity performance, to varying degrees.

The obvious mitigation strategy has also been discussed: to minimize flux trapping, minimize the amount of flux present during cooldown in the first place. This is accomplished in the vertical test dewar through passive magnetic shielding and active field cancellation using Helmholtz coils of various kinds. In the context of a cryomodule, magnetic shielding is common, however active cancellation is more difficult to employ due to concerns that the applied magnetic field could permanently magnetize other components in the cryomodule, which would effectively make this a single-cooldown only technique–not practical.

We now turn to the complementary question: given the presence of some amount of background magnetic field, what controllable parameters maximize the fraction of this flux that is expelled from the cavity when it is cooled down through its superconducting transition temperature, T_c? A cavity that is 'good' at expelling magnetic flux can tolerate much more background field *in situ* than one that is bad at it. Practical experience with dozens of research and development cavities, as well as with the N-doped production run of the LCLS-II cavities, revealed a wide variation in flux expulsion properties between niobium vendor, and even niobium lot number. Unfortunately, due to the lack of understanding regarding what measurable material parameters are related to the phenomena of flux trapping, experimentalists and accelerator builders are generally left to build cavities and discover their flux expulsion properties afterwards.

Empirically, two main factors have been found to contribute to improved flux expulsion: 1. high-temperature annealing of the niobium cavity (on the order of 900-1000°C for 3 hours) and 2. implementation of the so-called "fast-cooldown." [121]. The physics underlying the efficacy of the fast-cooldown is relatively well-understood, which we review briefly in the next section. The function of the high-temperature annealing, and its relationship to the flux expulsion properties of the cavity is more convoluted, and will guide the material studies

that the rest of the chapter focuses on.

6.1.1 Flux Trapping

The cooldown dynamics of a superconducting RF cavity are governed by the interplay of two opposing forces acting on the vortices: 1. the thermodynamic force, f_t, which which urges the vortices in the direction that minimizes the Gibbs free energy, and the flux-pinning force, f_p, which tugs the vortices towards their local pinning centers.

Following the analyses of [122], [104], the thermodynamic force,

$$f_t = -\frac{\partial g_{sc}}{\partial x} = -\frac{\partial g}{\partial T}\frac{\partial T}{\partial x} \tag{6.1}$$

requires a description of the Gibbs free energy density of a superconductor, g_{sc}. Beginning with the Gibbs free energy density of an object placed in a magnetic field, $g = f + BM$, where f is the free energy density, B is the magnetic field induction, and M is the magnetization, Martinello uses the definition of a superconductor in the Meissner state, in which $B = \mu_0(H + M) = 0$, to write g_{sc} as [104]:

$$g_{sc} = f - BH \tag{6.2}$$

f, the Helmholtz free energy density, can be written as the vortex number density, n, multiplied by the energy per unit length, E, $f = nE$. Also in terms of number density, B can be written as $B = n\Phi_0$. Furthermore, we can use the lower critical field, H_{c1}, to define both E and Φ_0, vis., $H_{c1} = E/\Phi_0$. H_{c1} has a temperature dependence, allowing us to finally write [104],

$$g = b\left[H_{c1}(0)\left(1-\left(\frac{T}{T_{c1}}\right)^2\right)-H\right] \tag{6.3}$$

taking the appropriate partial derivative, $-\frac{\partial g}{\partial T}$ and writing $\frac{\partial T}{\partial x}$, the single-dimensional thermal gradient, as ∇T, we find [104],

$$f_t = \frac{2BH_{c1}(0)T}{T_c^2}\nabla T \tag{6.4}$$

which comes out in terms of force per unit volume, and illustrates that not only do the vortices move in the direction of the spatial thermal gradient, ∇T, as a result of f_t, maximizing ∇T maximizes f_t. Experimentally, thermal gradient has indeed been shown to have a strong effect on the performance of SRF cavities, as shown in [123], [124], as well as in our own testing of the FRIB400 5-cell cavities. The prospect of rescuing cavity performance via a "fast cooldown" has put great technical focus on the effect of high ∇T, as shall be highlighted in the following experimental section.

The flux-pinning force resists this thermodynamic force. Briefly, this force is defined by the minimum current density, J_c, needed to disassociate the fluxons from their pinning centers [104]. This is the point at which the flux pinning force is equal to the Lorentz force acting on the vortex, making the pinning force, f_p,

$$f_p = |J_c \times n\Phi_0| = J_cB \tag{6.5}$$

(in terms of per unit volume), where n is again the number of fluxons consisting of the fundamental field quanta Φ_0, such that the total background field, B, is $B = n\Phi_0$. To find the so-called 'critical gradient,' ∇T_c, at which f_p balances t_t, we simply equate the

expressions, and solve for ∇T [104],

$$\nabla T_c = \frac{J_c T_c^2}{2H_{c1}(0)T} \tag{6.6}$$

The full analysis then moves to consider the statistical nature of the distribution and type of the flux pinning centers in the material [104]. From the expression above, a probability that a certain vortex is pinned with a critical current, J_{ci}, which can be rewritten to the pinning at a certain thermal gradient, ∇T_{ci}, can be assumed to have the Gaussian distribution,

$$P(\nabla T_c) = \int_0^{\nabla T_c} A e^{-\frac{(\nabla T_{ci} - \nabla T_{c_0})^2}{2\sigma^2}} d\nabla T_c \tag{6.7}$$

Where A is a normalization constant which can be found in the usual way by picking a large upper limit, setting the expression equal to one, and solving numerically [104]. This notionally describes a thermal gradient ∇T_{ci}, below which the vortices are expelled from the material (i.e., can be released from their pinning centers), and above which they are *not* released from their pinning centers $(1 - P(\nabla T_{ci}))$. The number of trapped vortices is thus $n_{trap} = [1 - P(\nabla T_{ci})]n$, which can then be related to the total trapped magnetic field, B_{trap} since $B_{trap} = n_{trap}\Phi_0$, where Φ_0 is the fundamental fluxon quanta [104]. We thus have a probabilistic expression for the amount of flux B_{trap} as a result of a certain gradient ∇T_{ci}.

As described in [104], the probabilistic expression for B_{trap} can next be converted to one for the ratio of the magnetic field measured at a point outside a particular cavity before and after the superconducting transition or the sake of modeling B_{SC}/B_{NC} at differing cooldown gradients (∇T). With this expression hand, Martinello is thence able to compare the predictions of this model directly to experimental measurements of B_{SC}/B_{NC} in 1.3 GHz cavities as a function of ∇T, finding that the experimental data is most successfully described

by a double-peaked distribution. This suggests the existence of at least two different varieties of pinning centers, each with their own distribution functions, with unique variances and centroids [104]. As such, to be completely successful at expelling magnetic flux, ∇T must be above ∇T_c for the stronger of these two pinning distributions.

The finding that there are likely multiple pinning distributions will be key to interpreting the flux expulsion studies conducted on the $\beta = 0.6$ cavities, which are the focus of the next few sections. While this analysis is clearly frequency-independent, flux trapping itself being a property of the bulk niobium of the cavity, we close this section with a few notes regarding the implications of this analysis for 644 MHz cavities. Namely, since the operating frequency and velocity dictates the cavity size and shape, flux expulsion dynamics are likely to be difficult to compare across frequencies. This is in part due to a nuance hidden in ∇T: the denominator of this expression is some one-dimensional linear distance measured between two points on the cavity surface. In cavities of differing size and shape, this linear metric does not capture the difference in the *area* of the transition region as the superconducting front progresses up the length of the cavity in the test dewar. We thus shall confine ourselves to only comparing our experimental flux expulsion data across cavities of the same frequency and velocity range.

6.1.2 Flux Expulsion Study Motivation

Focus on factors affecting the magnetic flux expulsion properties of SRF cavities was sharpened during the early stages of the production run of the 9-cell high-β 1.3 GHz LCLS-II cavities, which were the first N-doped cavities produced at scale. Early on, it became apparent that despite identical N-doping treatments, flux expulsion performance was not consistent from cavity to cavity, with some performing particularly poorly [125] [121]. It

was observed in FNAL testing that raw niobium material from different vendors, and also from different lots of niobium within the same vendor, had different flux expulsion performance (i.e., different outcomes for B_{SC}/B_{NC} at the the same ∇T). This phenomenon had been made particularly evident by the N-doped cavities heightened sensitivity to trapped magnetic flux: variance in flux expulsion performance properties exists in all cavities, but the few-times higher S of N-doped cavities strongly magnifies the detrimental effects of flux trapping.

It was found thereafter that certain high-temperature annealing treatments, such as 900-1000°C for around 3 h could rescue certain cavities' flux expulsion performance [121]. This was a boon for LCLS-II production as it provided a roadmap whereby underperforming cavities could be brought up to specification. The work of Posen et al. suggest that since this improvement is correlated with the increase in grain size that comes with the high-temperature annealing, it is possible that the grain boundaries function as at least one of the distributions of strong flux pinning centers hypothesized by Martinello's statistical model [121]. The possibility that the flux expulsion performance can be affected by the surface-treated state of the cavity, both inner and outer surfaces being considered, was also eliminated: this is indeed a bulk effect of the niobium material [121].

Since high-sensitivity cavities appear to be an unavoidable reality in upcoming high-Q_0 projects, we are motivated to identify and investigate the niobium material parameters associated with better or worse flux expulsion performance of the FRIB400-type cavities, and determine which of these parameters are the most controllable and by what means. Since heat treatment appears to be the most direct method of control, we design the following study around the effect of 900°C on the flux expulsion properties of niobium material from two different vendors, Ningxia and Tokyo-Denkai, in cell cavities for the medium-β 644-650

MHz regime.

While this study can provide insight into the mechanism of the high-temperature annealing effect on flux expulsion, it is important to note that, unlike the smaller, stiffer high-β 1.3 GHz LCLS-II cavities, high-temperature annealing may not be feasible to apply to large, sub-GHz 5-cell medium-β elliptical cavities, such as those under consideration for FRIB400 or PIP-II. As highlighted in Chapter 4, material structural integrity is already something of a concern given the steep-sidewall design, and high temperature annealing has the potential to cause the cavities to become even more malleable, which would make them even more challenging to handle or transport without compromising the field-flatness tuning. This represents significant risk since, once the cavities have been helium-jacketed, the only recourse for fixing a de-tuned cavity is to cut the (welded!) jacketing away and retune. Thus, while high-temperature annealing is an operational solution for LCLS-II, in the present work it is of more interest from a fundamental SRF science perspective. Should any outcome of the following study indicate it is necessary to apply high-temperature annealing to production cavities for projects like FRIB400 or PIP-II, it would be prudent to consider additional stiffening measures, and possibly explore a re-design of the stiffening rings currently in place between the cells to better protect against deformation.

6.1.3 Experimental setup

The availability of two single-cell cavities, B61S-EZ-102, a $\beta = 0.6$ 650 MHz PIP-II prototype cavity fabricated from Ningxia-sourced niobium, and S65-903, the FRIB400 $\beta = 0.6$ 644 MHz cavity fabricated from Tokyo-Denkai material afforded us the opportunity to test the consistency of cavity response to high-temperature annealing between these two vendors. Again, unlike the 1.3 GHz studies, these single-cell cavities will be truly representative of

the larger, sub-GHz cavity geometry behavior in imposed magnetic fields. This study is especially important to the FRIB400 and PIP-II projects given their high Q_0 requirements and the liklihood that N-doping techniques, as suggested in the previous chapter, will be used to achieve the ultimate Q_0 specifications for these machines when they go into production.

The flux expulsion performance of single-cell cavities is measured by using Helmholtz coils in the test dewar to impose 10-20 mG of magnetic field on the cavity while the cavity temperature is held above T_c. Fluxgate magnetic probes are placed at the cavity's equator, as shown the diagram in Figure 6.2 (a). The fluxgate probe is monitored through out the cooldown through T_c, and B_{SC}/B_{NC} is recorded from the fluxgate probe reading immediately before and after the superconducting transition. Raw data showing a double-y axis timeseries plot of a typiclal cooldown curve (K, left) and the magnetic field (mG, right) is shown in Figure **??**. Satisfyingly, the jumps in magnetic field measurement, representing the onset of the Meissner effect, and thus expulsion of the magnetic field from the cavity bulk to the cavity exterior, are clearly visible. Furthermore, even by eye, it is clear that the larger thermal gradient lead to the largest increase in magnetic field measured at the cavity equator after the superconducting transition.

This value is then plotted as a function of ∇T, which is measured as follows: the usual Cernox temperature sensors are mounted on the cavity surface, one at the cavity equator and another on the iris immediately above the cavity equator. When the equator temperature sensor reaches T_c, ∇T is calculated as:

$$\nabla T = \frac{T_{iris} - T_{equator}}{x_{top} - x_{equator}} \tag{6.8}$$

Here, $x_{top} - x_{equator}$ is the linear distance as traced along the cavity surface between

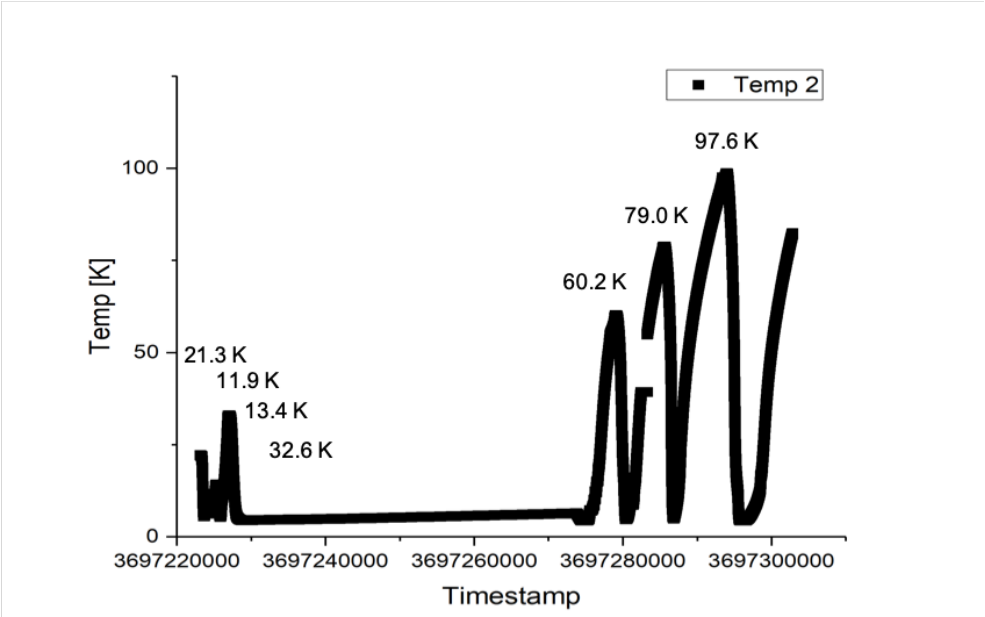

Figure 6.1: Example time-series plot of the cavity temperature during a thermocycling test. The differing maximum temperatures represent different ∇T through which the cavity under test was cooled.

the two sensors, which is longer than the simple projection of the distance in the vertical orientation. This value being the same for both cavities in this study, however, it has little bearing on the following results, and is simply used tthroughout for consistency's sake.

Through magnetic field simulation tools, e.g., CST Microwave Studio, the ideal expulsion ratio at a particular point can be found, which is then compared to the experimentally measured value. The results of such a simulation for a 5-cell FRIB400 cavity, where the ratio is measured at the cell equators, are shown in Figure [**fig:dia**](b). For the single-cell versions of these cavities, the value is somewhat lower, approximately 1.8, near the equator.

6.1.4 Flux Expulsion results

B61S-EZ-102, fabricated from Ningxia-sourced niobium (NX), and S65-903, fabricated from Tokyo-Denkai material (TD), had their flux expulsion performance measured in two different

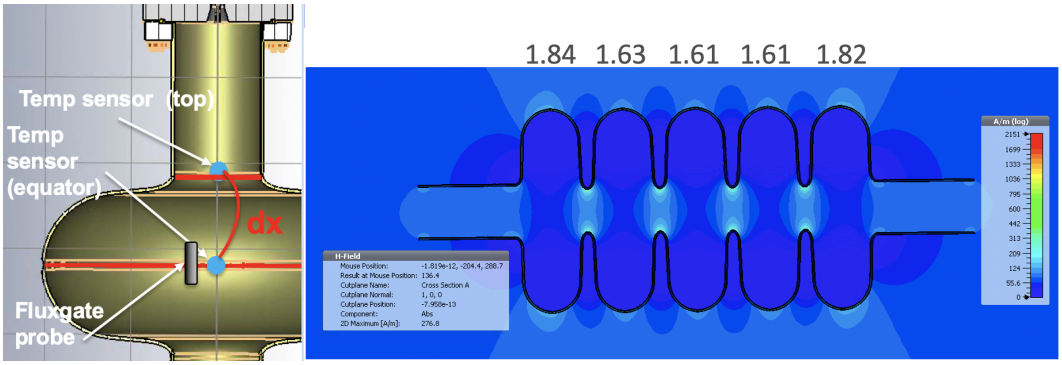

(a) (b)

Figure 6.2: (a) Diagram of the experimental setup with the positions of the fluxgate magnetic probe, and two Cernox temperature sensors highlighted. (b) CST Microwave Studio simulation of idealized flux expulsion in a 5-cell FRIB400. cavity.

states: After bulk EP followed by 10 μm cold EP, then, after 900°C 3 h baking. The results, in terms of B_{SC}/B_{NC} vs ∇T are plotted in Figure **??**.

It is immediately apparent that, despite differing sources niobium, both cavities experience similar improvements in B_{SC}/B_{NC} after 900°C 3h baking. Of note, while cryomodule performance varies from design to design, it is unlikely that any realistic versions will achieve ∇T of much over 0.5 K/cm. Thus, while the right-hand end of the plot in Figure **??** may look appealing, it is unlikely a system will be able to operate anywhere in that region. However, finding that niobium from two distinct vendors behaved similarly is an intriguing finding. Moreso than if material from the same vendor had behaved similarly, this particular scenario has a higher likelihood of isolating the specific causative parameter. We thus turn to material-focused studies to attempt to determine what property of the niobium material is the relevant one to the change in flux expulsion that occurs under heat treatment.

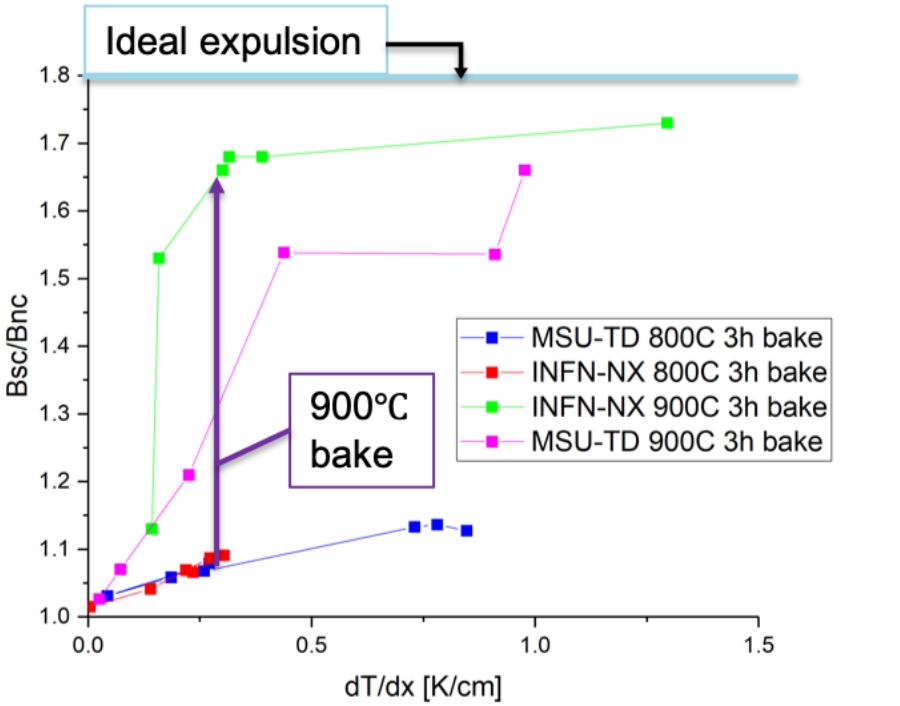

Figure 6.3: Flux expulsion ratio (Bsc/Bnc) is improved significantly in 900 C annealed cavities. Pre-annealing, both cavities performed similarly poorly. 900°C annealing significantly restored expulsion performance. The simulated ideal expulsion ratio,1.8, is marked at the top of the plot.

6.2 Material studies

Having demonstrated that 900°C 3 h annealing affected some material parameter in such a way as to promote flux expulsion, we now attempt to pinpoint said material parameter (or parameters). Apart from satisfying natural curiosity, identifying a measurable material parameter that accurately predicts the flux expulsion performance of a cavity fabricated from said material would be of significant industrial benefit. As has been heavily implied, the only method of determining the flux expulsion properties of a given vendor or niobium lot hitherto is to fabricate a single-cell cavity from the material and test it in the described thermocycling experiment in a test dewar. This is time-consuming and costly, particularly

when the cavities under-perform, and require baking and re-testing (sometimes even for multiple iterations).

If a commonly-measurable material parameter, such as grain size, could be used to predict expulsion performance, and thereby be used to communicate clear material specifications to the niobium vendors, a significant part of the guesswork outlined above could be sidestepped. Evidence indicates that grain size could be a significant indicator regarding flux expulsion, and the instruments available in the Fermilab Material Science Laboratory (MSL) include a scanning electron microscope (SEM) which may be used to conduct electron backscatter diffraction (EBSD) to measure sample gain size and development. The FNAL also has a Physical Property Measurement System (PPMS) which is a device that can directly measure flux-pinning force (f_p) in small niobium samples at temperatures from 2 to 9 K.

6.2.1 Sample preparation

Niobium samples for these studies were taken from the scrap niobium material left over from cavity fabrication. Samples for EBSD measurement are approximately 10 mm square by 4 mm deep, where the depth is simply the thickness of the niobium sheet from which the cavity is fabricated. Samples for PPMS measurement are approximately 3 mm in diameter by 8 mm in length cylindrical pieces. Since these samples were to be baked, it was necessary to conduct bulk EP on these samples in order to protect the vacuum furnace. Again, based on the results of Posen et al., the surface preparation of the samples does not affect the magnetic flux expulsion properties of the bulk niobium under test.

These samples were then divided into three groups. Separate sets of EBSD samples from NX and TD material were either baked at 800°C for 3h, which is representative of the baseline cavity state after hydrogen degassing, or baked at 900°C for 3h, representing

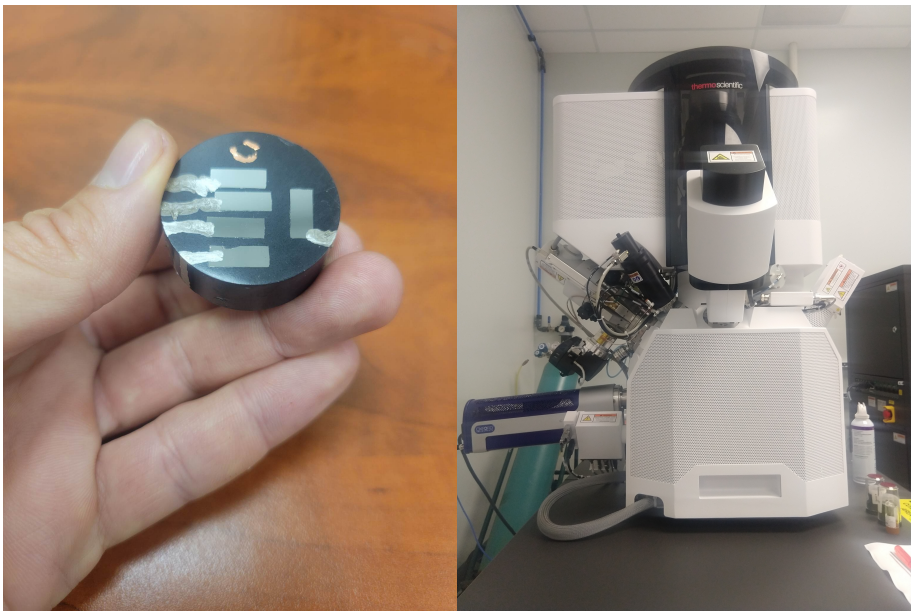

(a) (b)

Figure 6.4: (a)The bakelite-mounted, polished niobium samples prepared for EBSD measurement. (b) SEM/EBSD used at Fermilab MSL.

the high-temperature annealing state, or baked at 950°C, for mostly exploratory purposes. These samples were then cut with a diamond blade and mounted in bakelite molds and polished per standard EBSD preparation procedures.

Samples for the PPMS flux-pinning force measurement were also bulk electropolished and divided into three groups: unbaked, baked at 800°C for 3h, and baked at 900°C for 3h. Subsequent to the first study, the unbaked set were then 800°C baked for 3h, tested, then baked at 900°C for 3h, then tested again, more precisely mimicking the sequence of baking that the cavities fabricated from those materials experienced before being measured in the thermocycling test of the previous section.

(a) (b)

Figure 6.5: (a) PPMS insert device with niobium sample mounted (circle). (b) PPMS instrument used at FNAL.

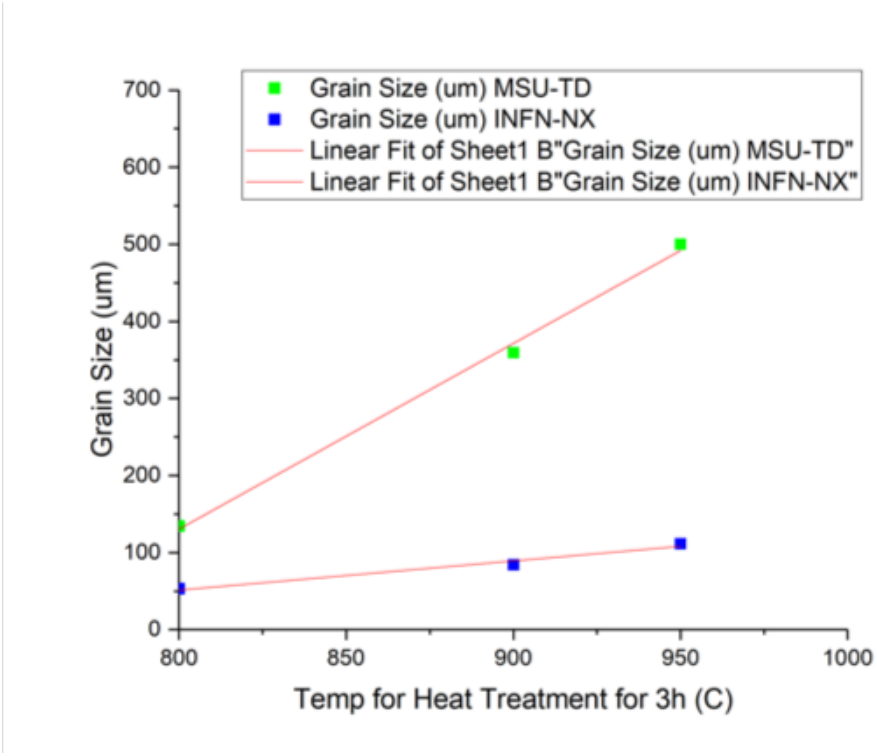

Figure 6.6: Flux pinning force as measured in sequentially heat-treated niobium samples in PPMS. 900 C annealing reduces the flux pinning force measured in small-grain Ningxia (INFN-NX) samples as well as in the larger-grain Tokyo-Denkai samples (MSU-TD).

6.2.2 EBSD Results

The grain size is measured in μm as the fitted major ellipse diameter. As shown in Figure 6.6, fairly linear size development is observed in niobium from both vendors, with the Tokyo-Denkai material starting off with grains of a substantially larger size that growing more rapidly than the Ningxia material, which starts off with grains less than half as large as those in the TD material and grows more slowly.

Recall, the analogous cavities had similarly poor flux expulsion performance after 800°C baking, and similarly improved flux expulsion performance after 900°C baking. Unfortunately the differing grain size measurements both before and after this 900°C baking indicates no absolute link between grain size and flux expulsion performance in the sense that,

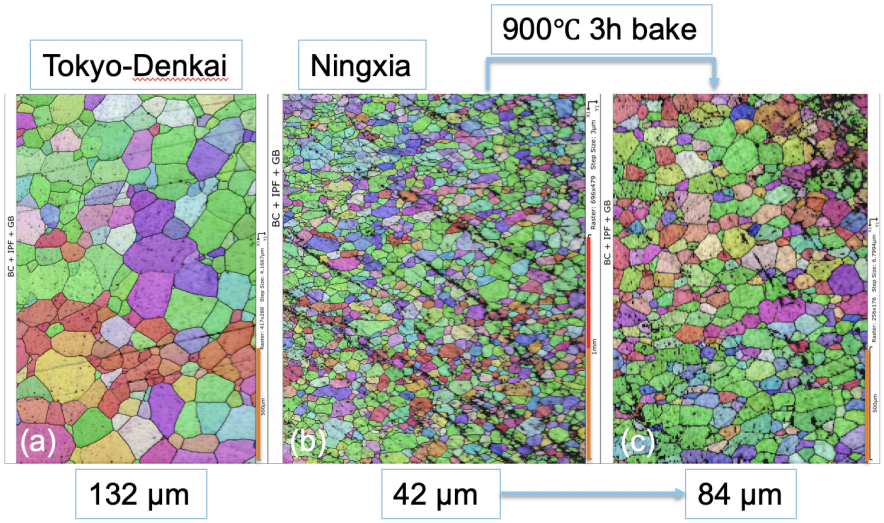

Figure 6.7: Flux pinning force as measured in sequentially heat-treated niobium samples in PPMS. 900 C annealing reduces the flux pinning force measured in small-grain Ningxia (INFN-NX) samples as well as in the larger-grain Tokyo-Denkai samples (MSU-TD).

as one might have hoped, a single grain size could be related to a single flux-expulsion ratio. In a somewhat dramatic refutation of this hope, the Ningxia cavity's grains post-900°C baking, which expels flux well, remain at an average size that is 37% smaller than that of the pre-900°C baked Tokyo-Denkai cavity's grains, which expels flux poorly, as shown in Figure 6.7.

Building on the hypothesis from Martinello's statistical analysis that there are two distributions of pinning centers, it seems apparent that the grain boundaries do not comprise the most significant of these distributions in niobium from either Ningxia or Tokyo-Denkai. The question is, however, difficult to decouple from the presence of boundary-related dislocation-type defects, which may be dissolved with the high annealing temperature. Previous work with ex-situ niobium samples supports this finding: though it is true single-crystal samples trapped less flux than polycrystalline samples in all cases, among the single-crystal samples studied, annealed single-crystal samples trapped less flux than the non-annealed

single-crystal control sample [126]. Specifically, where the single-crystal sample trapped about 73% of the applied flux, the 800°C annealed sample trapped about 62%, and the 1200°C annealed sample trapped only 42% [126]. Among the polycrystalline samples studied, 800°C annealing reduced flux trapping from 100% to approximately 80% [126], possibly due to the conflated effect of grain boundaries and distributed dislocations.

6.2.3 PPMS Results

The results of the EBSD measurement not being as cut-and-dry as one would have hoped, in terms establishing a deterministic relationship between the grain size and the flux expulsion properties in these Ningxia and Tokyo-Denkai samples, we now change focus to making direct measurement of the flux-pinning force (f_p) of the niobium samples.

The PPMS measurements were taken at a temperature of 9 K, which is the closest stably-controllable temperature to the niobium's superconducting critical temperature of about 9.2 K. The device applies a DC magnetic field to the sample, sweeping through approximately 200 Oe in opposite polarizations. The PPMS measures the resulting magnetization of the sample. An example of such a measurement scan is shown in Figure **??**.

The flux pinning force is calculated from this measurement as follows. The magnetization curve is divided into the half in the ascending direction (M_+), and the other half in the descending direction (M_-). The *irreversible* magnetization, M_{irr} is then:

$$M_{irr} = \frac{M_+ - M_-}{2} \tag{6.9}$$

Lange's calculation of the critical current density of hard superconductors from the magnetization of cylindrical samples [127], is commonly used in this analysis, and gives,

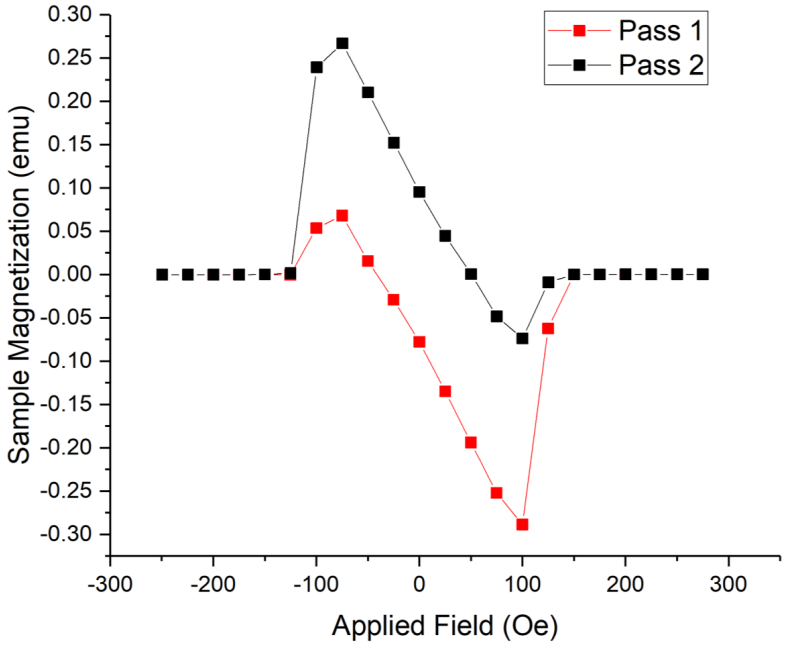

Figure 6.8: Sample magnetization vs. applied field data measured at 9 K in the FNAL PPMS machine. The two sweep directions, Pass 1 and Pass 2, are differentiated by color.

$$-4\pi M_{irr} = \frac{a}{3} 4\pi J_c \tag{6.10}$$

From which we arrive at,

$$J_c = -\frac{3M_{irr}}{a} \tag{6.11}$$

where a is the sample radius. Once J_c is obtained, the flux pinning force is simply $f_p = J_c \times B_{applied}$, or $f_p = J_c B$. Thinking in terms of flux-pinning force is not particularly intuitive, (in this case, winding up in units of 10^6 N/m^3). Converting units, the applied magnetic field is on the order of 100 Gauss, which is quite a bit different from the few mGauss expected in cavity vertical testing. However, we emphasize that the intent with this

particular assay is not to replicate an environment for the niobium that is representative of that of the test dewar or cryomodule. Rather, the aim is to determine if there is any correlation at all between trend in the (absolute) flux pinning force measurement, and the trend in the cavity flux expulsion ratio before and after high-temperature annealing. The tacit assumption is that the relationship between the high-field flux pinning force measurements after different baking treatments remains true and the trend in f_p remains linear down into the very low-field region, well below the sensitivity of the PPMS device.

The results are shown in Figure **??**. The data show the progression of the flux pinning force through three sample states: 1. As received (untreated), 2. After 800°C 3 h baking, and 3. After the sequence of 800°C 3 h followed by 900°C 3 h baking. The plot shows the peak flux pinning force decreases in each case, with the f_p curve responding in a similar way between the Ningxia and Tokyo-Denkai material at each step.

The correlation between the trend depicted in Figure **??** and the trend of the flux expulsion ratio depicted in Figure **??** may seem trivially obvious given the relationship between f_p and f_t derived in the earlier section. However, given the quantity of unknowns in this system, experimental validation of f_p as the figure of merit in terms of determining the eventual flux expulsion performance of a cavity is still highly valuable. PPMS systems, while costly, are industrially available and could be used to 1. specify maximum acceptable f_p in a particular lot of niobium, and 2. be used to iterate over various baking treatments, without the need to fabricate and test a cavity.

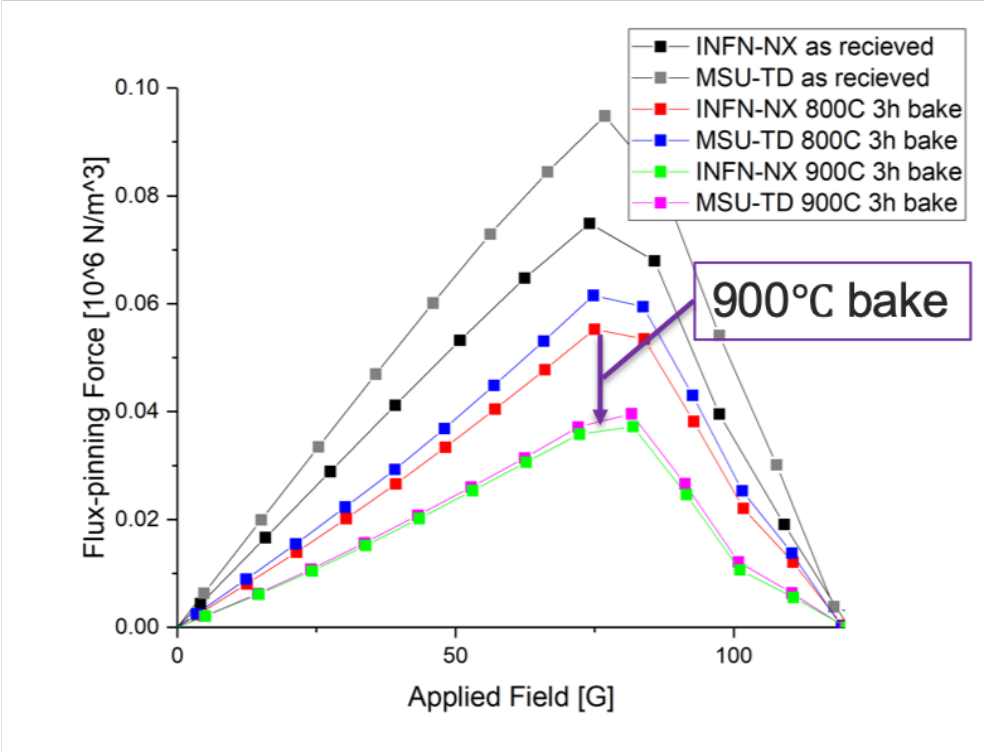

Figure 6.9: Flux pinning force as measured in sequentially heat-treated niobium samples in PPMS. 900 C annealing reduces the flux pinning force measured in small-grain Ningxia (INFN-NX) samples as well as in the larger-grain Tokyo-Denkai samples (MSU-TD) by similar amounts.

6.3 Conclusions

As previous studies indicated, while gain size has some bearing on the flux expulsion performance of the cavity, [121] [126] [104], the most deterministic measure of cavity flux expulsion capabilities appears to be the direct measure of f_p enabled by the PPMS device. The results of this case study of the Ningxia and Tokyo-Denkai niobium establish a promising correlation between f_p and B_{SC}/B_{NC} however, significantly more trials will be needed before it can be stated with any confidence that niobium with an f_p of a particular strength X will always result in a cavity with a B_{SC}/B_{NC} of Y. Unfortunately, it appears that the grain boundaries themselves are somewhat uncorrelated with this performance metric, likely due to the

confounding effect of grain-boundary related dislocations. Ultimately, further understanding of the relationship between material parameters and ultimate quantum properties of a superconducting RF cavity can be highly beneficial, and merit further study going forward.

While this has been an interesting exercise to probe the fundamental properties of flux pinning centers using temperature as a controllable parameter in Ningxia and Tokyo-Denkai material, it warrants re-emphasizing that given the structural concerns inherent in high-temperature annealing the full-size cavities, 900°C baking (and upward) may not be a viable method of R_0 reduction in 5-cell elliptical $\beta = 0.6$ 644-650 MHz production cavities. Preliminary testing of sequentially baked niobium samples at Jefferson Laboratory related to LCLS-II investigations [128] found a downward trend in yield strength (YS) with increasing annealing temperature, however it is difficult to infer from these data, collected from standard flat, dog-bone type samples, what the implications would be for a formed cavity, with much more complicated curved geometry. In addition to the aforementioned concerns regarding the risk of cavity detuning, changes in ultimate yield strength of cavities also have complex implications for pressure vessel safety specifications. Ultimately, systematic and targeted research involving the specific lots of niobium to be used for production cavities will be required to more fully understand the flux expulsion properties of the material and the potential benefits and drawbacks of high-temperature annealing.

Chapter 7

Thesis Conclusions and Outlook

In the course of this work, we have explored many properties of the proposed FRIB400 prototype $\beta = 0.6$ 644 MHz 5-cell elliptical superconducting RF cavity. The fundamental design of the cavity has been validated in terms of its mechanical and RF properties, and the preliminary results of both conventional and advanced surface preparations have shown significant potential to exceed the FRIB400 minimum Q_0 specification of 2×10^{10} at the accelerating gradient of 17.5 MV/m.

Throughout this analysis, it has been shown that the opportunity to explore the properties of N-doping in a low-frequency cavity is intriguing both from a fundamental physics perspective and from the perspective of maturing the technology for use in a full production run for a real-world machine. Of the experimental achievements outlined in this work, the strong Q_0 vs E_{acc} performance 2/0 N-doped cavity remain the most significant, nearly doubling the minimum FRIB400 design goal of 2×10^{10} at 17.5 MV/m.

In a field often singly-focused on pushing the gradient frontier, cavities such as these that can afford to sacrifice gradient for the somewhat single-minded pursuit of high-Q_0 offer a unique avenue of exploration. While some might argue that 'to understand high-gradient is to understand high-Q,' the results herein show this is generally not the case, particularly when considering high-Q recipes such as N-doping that can tend to lower the quench fields of treated cavities. In a machine operating at 17.5 MV/m, a treatment, such as 2/0 N-doping,

that tends to quench at 25-29 MV/m is of no operational detriment, if the Q_0 is sufficiently high.

While significant advances in theoretical understanding have been made in the past decade since the discovery of N-doping, gaps in understanding yet remain that can only be expediently filled by experimental contributions. In parallel, we must also acknowledge the following: while satisfying from a pure physics perspective, it is not a given that "solving" the N-doping effect, or the anti-Q slope, or the loss mechanisms of trapped vortices, etc., would enable us to construct some ideally perfect cavity at any frequency or gradient range. That is to say, fundamental understanding of the quantum-mechanical scale phenomena we seek to exploit in no way guarantees that we have the ability to manipulate the relevant parameters on a relevant scale of precision, either in the highly-controlled context of vertical cavity testing, or the somewhat less controllable context of in-situ accelerator operation.

Still, at the end of this analysis, we are left with several promising courses of action regarding optimizing and improving surface-treatments for FRIB400-type cavities. They are:

1. Focus on improvement of EP parameters that may further improve the outcome of 2/0 N-doping in 644 MHz SRF cavities

2. Focus on passive background flux mitigation strategies that can be implemented with relative ease in the cryomodule context

3. Explore high-temperature annealing if residual resistance losses prove too detrimental

4. Specify fast-cooldown needs in cryomodules

5. Use flux-pinning force measurements as a method to tailor the high-temperature an-

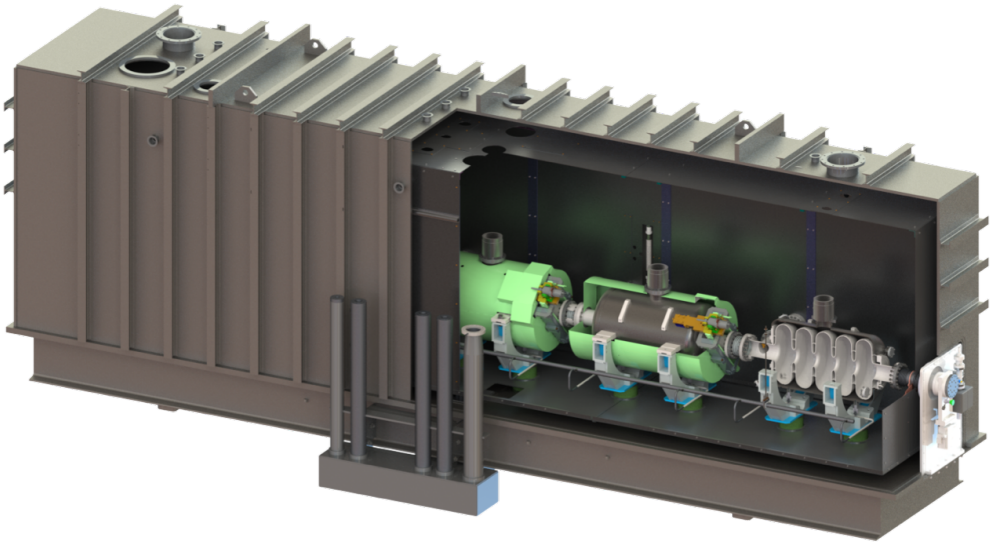

Figure 7.1: Conceptual design drawing of a cryomodule incorporating FRIB400 $\beta = 0.6$ 644 MHz cavities. (Provided by the FRIB Team).

nealing procedure to the particular niobium lot or vendor to achieve maximum flux expulsion

In addition to the enumerated list above, a principal future concern remains: how to successfully transfer the Q_0 performance achieved in the vertical test dewar to the cryomodule context. FRIB baseline production has shown an exemplary ability to transfer cavity vertical test performance to the cryomodule with no degradation in Q_0 [129], however the larger dimension of the FRIB400 cavities makes them more at risk to statistical defects such as particulate contamination. Their (likely) greater sensitivity to their magnetic environment will also contribute to the challenge of maintaining vertical test performance in the cryomodule. As is customary in projects of the scale of the proposed FRIB400, development of a prototype-like cryomodule, such as that shown in Figure **??**, will be critical to validating that the results achieved in vertical testing, described herein, can be successfully transferred to an operational context.

Other outstanding areas of research that are outside the scope of this thesis but are critical

next steps towards realizing a $\beta = 0.6$ 644 MHz cavity cryomodule include integration and testing of the cavity's dynamic tuning system incorporating 'slow' and 'fast' tuners [130], fundamental power couplers [48], and cryogenic system.

BIBLIOGRAPHY

[1] A. Sessler and E. Wilson. *Engines of Discovery*. Singapore: World Scientific Publishing Co. Pte. Ltd., 2007.

[2] S. Weinberg. "A Model of Leptons." In: *Phys. Rev. Lett.* 19 (21 Nov. 1967), pp. 1264–1266. DOI: 10.1103/PhysRevLett.19.1264. URL: https://link.aps.org/doi/10.1103/PhysRevLett.19.1264.

[3] Ed.: M. Vretenar. "Linac4 Design Report." In: *CERN Yellow Reports* 6 (2020). DOI: 10.23731/CYRM-2020-006. URL: https://e-publishing.cern.ch/index.php/CYRM/issue/view/121.

[4] A. Abada, M. Abbrescia, and S.S. AbdusSalam. "FCC Physics Opportunities." In: *Eur. Phys. J.* 79.474 (2019). DOI: 10.1140/epjc/s10052-019-6904-3.

[5] A. Butterworth et al. "SRF for Future Circular Colliders." In: *Proc. of SRF2015, JACoW* FRBA04 (2015). URL: https://accelconf.web.cern.ch/SRF2015/papers/frba04.pdf.

[6] Yuri Alexahin et al. "The Case for a Muon Collider Higgs Factory: A white paper." In: *arXiv* 1307.6129 (2013). URL: https://doi.org/10.48550/arXiv.1307.6129.

[7] J. Brau, Y. Okada, and N. Walker. "ILC Reference Design Report Volume 1 - Executive Summary." In: *arXiv* 0712.1950v1 (2007). URL: https://doi.org/10.48550/arXiv.0712.1950.

[8] A. Grassellino. "Pushing bulk Nb limits." In: *Tutorial, presented at SRF2019* (2019). URL: http://accelconf.web.cern.ch/srf2019/talks/frtu3_talk.pdf.

[9] *Next step toward the ILC realization: MEXT expert panel publishes recommendations*. Compiled by the Inter-University research institute corporation and High Energy Accelerator Research Organization. URL: https://www.kek.jp/en/topics-en/202202251335/.

[10] Bryan W. Lynn et al. "Nuclear matter as a liquid phase of spontaneously broken semiclassical SU(2)L x SU(2)R chiral perturbation theory: Static chiral nucleon liquids." In: *Phys. Rev. C* 105 (1 Jan. 2022). DOI: 10.1103/PhysRevC.105.014313. URL: https://link.aps.org/doi/10.1103/PhysRevC.105.014313.

[11] David M. Jacobs, Glenn D. Starkman, and Bryan W. Lynn. "Macro dark matter." In: *Monthly Notices of the Royal Astronomical Society* 450.4 (July 2015). DOI: 10.1093/mnras/stv774.

[12] The FRIB Science Community. *FRIB400: The Scientific Case for the 400 MeV/u Energy Upgrade of FRIB*. https://frib.msu.edu/_files/pdfs/frib400_final.pdf. Accessed: 2022-08-01. 2019.

[13] *FRIB Scientific and Technical Merit*. https://frib.msu.edu/_files/pdfs/frib_scientific_and_technical_merit_lite_0.pdf. Accessed: 2022-08-01. 2009.

[14] Gordon Arrowsmith-Kron et al. "Opportunities for Fundamental Physics Research with Radioactive Molecules." In: *arXiv* 2302.02165 (2023). URL: https://doi.org/10.48550/arXiv.2302.02165.

[15] L. Merminga. *PIP-II Project Overview*. https://accelconf.web.cern.ch/srf2019/talks/frtu3_talk.pdf. PIP-II Technical Workshop, Dec. 2020.

[16] A. Cano. "Surface structural studies of SRF Nb cutouts at cryogenic conditions using synchrotron radiation-based characterization techniques." In: *Proc. TTC 2022, TESLA Technology Collaboration* (Jan. 2022). URL: https://indico.desy.de/event/32219/contributions/116549/.

[17] Jurgen Bosch. "PPI inhibitor and stabilizer development in human diseases." In: *Drug Discovery Today: Technologies* 24 (2017). DOI: 10.1016/j.ddtec.2017.10.004.

[18] I. Nengo et al. "New infant cranium from the African Miocene." In: *Nature* 548 (Aug. 2017). DOI: 10.1038/nature23456.

[19] D. Gonnella et al. "Industrialization of the nitrogen-doping preparation for SRF cavities for LCLS-II." In: *Nuclear Inst. and Methods in Phys. Research, A* 883 (Nov. 2018). DOI: 10.1016/j.nima.2017.11.047.

[20] D.I. Thwaites and J.B. Tuohy. "Back to the future the history and development of the clinical linear accelerator." In: *Physics in Medicine and Biology* 51.13 (2006). DOI: 10.1088/0031-9155/51/13/R20.

[21] V. Favaudon, C. Fouillade, and M-C. Vozenin. "Ultrahigh dose-rate, flash irradiation minimizes the side-effects of radiotherapy." In: *Cancer radiotherapie journal de la Societe francaise de radiotherapie oncologique* 19.6 (2015). DOI: doi:10.1016/j.canrad.2015.04.006.

[22] J.B. Farr. "The future of medical linacs." In: *Proc. of LINAC22, JACoW* FR2AA02 (2022). URL: https://accelconf.web.cern.ch/linac2022/talks/fr2aa02_talk.pdf.

[23] Inc. Niowave. "Medical and Industrial radioisotope production." In: (). URL: https://www.niowaveinc.com/index.php/medical-radioisotopes/.

[24] Y. He et al. "Development of accelerator-driven advanced nuclear energy (ADANES) and nuclear fuel recycle." In: *Proc. of 10th int. Part. Accel. Conf. IPAC2019, JACow* (). DOI: 10.18429/JACoW-IPAC2019-TUYPLS2.

[25] H. Abderrahim. *MYRRHA: Flexible and FastSpectrum Irradiation Facility*. Switzerland: Thorium Energy for the World, Springer International Publishing, 2016.

[26] C. Kennedy. "Vagueness and Comparison." In: *Vagueness and Language Use*. London, UK: Palgrave-Macmillan, 2011, pp. 73–97. ISBN: 978-0-230-29931-3. DOI: 10.1057/9780230299313_4.

[27] J.D. Jackson. *Classical Electrodynamics*. United States: John Wiley and Sons, Inc., 1999.

[28] Hasan Padamsee, Jens Knobloch, and Tom Hays. *RF Superconductivity for Accelerators*. Weinheim: Wiley-VCH Verlag GmbH and Co, KGaA, 2008.

[29] Thomas P. Wangler. *RF Linear Accelerators*. Weinheim: Wiley-VCH Verlag GmbH and Co, KGaA, 2008.

[30] J. Popielarski. *Cavity Performance Testing: Vertical Dewar and Cryomodule: a Tutorial*. East Lansing, MI, USA, 2021. URL: https://indico.frib.msu.edu/event/38/attachments/159/1271/SRF2021_Tutorial_-_J._Pop.pdf.

[31] T. Powers. "Theory and practice of RF cavity test systems." In: *Proceedings of the 12th International Workshop on RF Superconductivity* SUP02 (2005). URL: https://accelconf.web.cern.ch/SRF2005/papers/sup02.pdf.

[32] O. Melnychuk, A. Grassellino, and A. Romanenko. "Error analysis for intrinsic quality factor measurement in superconducting radio frequency resonators." In: *Rev. of Sci. Inst.* 85.124705 (2014). DOI: 0.1063/1.4903868.

[33] H.K. Onnes. "The Superconductivity of Mercury." In: *Comm. Phys. Lab. Univ.* (1911).

[34] *The Nobel Prize in Physics 1913*. URL: https://www.nobelprize.org/prizes/physics/1913/summary/.

[35] W. Meissner and R. Ochsenfeld. "Ein neuer Effekt bei Eintritt der Supraleitfahigkeit." In: *Physica Naturwissenschaften* 21.787 (1933).

[36] M. Tinkham. *Introduction to Superconductivity, 2nd Ed.* Garden City, NY. United States: Dover Publications, Inc, 2004.

[37] C. J. Gorter and H. Casimir. "On Supraconductivity I." In: *Physica* 1 (1934).

[38] A. B. Pippard. "An Experimental and Theoretical Study of the Relation Between Magnetic Field and Current in a Superconductor." In: *Proc. R. Soc. Lond. A.* 216 (1953).

[39] J. Bardeen, L. N. Cooper, and J. R. Schrieffer. "Theory of Superconductivity." In: *Phys. Rev.* 108 (1957).

[40] N.W. Ashcroft and N.D. Mermin. *Solid State Physics*. United States: Brooks/Cole Thomson Learning, 1976.

[41] D. C. Mattis and J. Bardeen. "Theory of the Anomalous Skin Effect in Normal and Superconducting Metals." In: *Phys. Rev.* 111 (1958).

[42] D. Bafia. *Exploring and understanding the limitations of NB srf cavity performance*. Ann Arbor, MI. United States, 2020.

[43] V.L. Ginzburg and L.D. Landau. "On the Theory of Superconductivity." In: *Eksp. Teor. Fiz.* 20 (1950).

[44] K. McGee et al. "Medium-velocity superconducting cavity for high accelerating gradient continuous-wave hadron linear accelerators." In: *Physical Review Accelerators and Beams* 24.11 (Nov. 2021). DOI: 10.1103/PhysRevAccelBeams.24.112003.

[45] N. Valles and M. Liepe. "The superheating field of niobium: theory and experiment." In: *Proc. SRF2011 JACoW* TUIOA05 (2011).

[46] P. Knudsen. "PHY862 - Cryogenics - Fall 2019." In: *Lecture, Unpublished, Michigan State University* (2019).

[47] A. Grassellino. *Pushing bulk niobium limits*. https://accelconf.web.cern.ch/srf2019/talks/frtu3_talk.pdf. Dresden, Germany, June 2019.

[48] P.N. Ostroumov et al. "Elliptical superconducting RF cavities for FRIB energy upgrade." In: *Nuclear Inst. Meth. in Phys. Research A* A.888 (2018). DOI: 10.1016/j.nima.2018.01.001.

[49] M. Drury et al. "Overview of SNS Cryomodule Performance." In: *Proceedings of 2005 Particle Accelerator Conference, JACoW* (2005).

[50] R. Ainsworth et al. "Bead-pull test bench for studying accelerating structures at RHUL." In: *Proc. of IPAC11 2011, JACoW Publishing* MOPC049 (2011).

[51] C.A. Maher et al. "Measuring electromagnetic field flatness in the 5-cell coupled resonating cavity: a superconducting cavity." In: *MSU/FRIB REU poster, unpublished* (2018).

[52] J. Delayen. "Ponderomotive instabilities and microphonics?a tutorial." In: *Physica* 441C, 1 (2006). DOI: 10.1016/j.physc.2006.03.050.

[53] S-H. Kim. "RF commissioning of the first three Beta = 0.041 quarter-wave resonator cryomodules in FRIB driver linac." In: *Second Topical Workshop on Mirophonics* (2018).

[54] S-H. Kim. "Resonance control with pneumatic slow frequency tuners for FRIB half-wave resonantors." In: *Tesla Technology Collaboration Meeting, JACoW* (2020). DOI: 10.1016/j.nima.2018.01.001.

[55] L. Lilje, S. Simrock, and D. Kostin. "Characteristics of a fast piezo-tuning mechanism for superconducting cavities." In: *Proc. of EPAC 2002, JACoW* (2002).

[56] O. Kononenko et al. "3D multiphysics modeling of superconducting cavities with a massively parallel simulation suite." In: *Phys. Rev. Accel. Beams* 20.102001 (2017). DOI: 10.1103/PhysRevAccelBeams.20.102001.

[57] B. Aune et al. "Superconducting TESLA cavities." In: *Phys. Rev. ST Accel. Beams* 3 (9 Sept. 2000), p. 092001. DOI: 10.1103/PhysRevSTAB.3.092001. URL: https://link.aps.org/doi/10.1103/PhysRevSTAB.3.092001.

[58] K. Saito et al. "Superiority of electropolishing over chemical polishing on high gradients." In: *Part. Accel.* 60 (1998).

[59] K. Saito. "Development of electropolishing technology for superconducting cavities." In: *Proc. of 2003 Particle Accel. Conf. JACoW* (2003).

[60] S. Michizono. "The International Linear Collider." In: *Nat. Rev. Phys.* 1.244 (2019). DOI: 10.1038/s42254-019-0044-4.

[61] W. Singer et al. "Production of superconducting 1.3-GHz cavities for the European X-ray Free Electron Laser." In: *Phys. Rev. Accel. Beams* 19 (9 Sept. 2016), p. 092001. DOI: 10.1103/PhysRevAccelBeams.19.092001. URL: https://link.aps.org/doi/10.1103/PhysRevAccelBeams.19.092001.

[62] Z. A. Conway et al. "Achieving high peak fields and low residual resistance in half-wave cavities." In: *Proceedings of SRF 2015, JACoW* (2015).

[63] T. Xu et al. "Progress of FRIB SRF production." In: *Proceedings of SRF2017, JACoW* (2019).

[64] W. Hartung et al. "Large-Scale Dewar Testing of FRIB Production Cavities: Results." In: *3rd North American Particle Accelerator Conference (NAPAC2019)* MOPLO17 (2019). DOI: 10.18429/JACoW-NAPAC2019-MOPLO17.

[65] A. Bosotti et al. "Tests of ESS Medium-beta Prototype Cavities at LASA." In: *Proceedings of IPAC17, JACoW* MOPVA063 (2017).

[66] M.P. Kelly and T. Reid. "Surface processing for bulk niobium SRF cavities." In: *Supercond. Sci. Technol.* 30.043001 (Feb. 2017). DOI: 10.1088/1361-6668/aa569a.

[67] H. Tian and C. Reece. "Evaluation of the diffusion coefficient of fluorine during the electropolishing of niobium." In: *Phys. Rev. ST Accel. Beams* 13 (8 Aug. 2010),

p. 083502. DOI: 10.1103/PhysRevSTAB.13.083502. URL: https://link.aps.org/doi/10.1103/PhysRevSTAB.13.083502.

[68] V. Chouhan et al. "Effect of electropolishing on nitrogen doped and undoped niobium surfaces." In: *Proc. of NAPAC 2022, JACoW Publishing* (Aug. 2022).

[69] M. Bertucci et al. "Electropolishing of PIP-II low beta cavity prototypes." In: *19th. Int. Conf. on RF Superconductivity. JACoW Publishing* SRF2019 (2019). DOI: 10.18429/JACoW-SRF2019-MOP057.

[70] C.Z. Antoine et al. "Morphological and Chemical Studies of Nb Samples After Various Surface Treatments." In: *Proceedings of SRF99, JACoW* TUP035 (1999).

[71] K. Saito et al. "Superconducting RF Development for FRIB at MSU." In: *Proceedings of LINAC2014, JACoW* THIOA02 (2014).

[72] J.P. Charrier, B. Coadou, and B. Visentin. "Improvements of superconducting cavity performance at high accelerating gradients." In: *Proc. of e98* (1998). URL: https://accelconf.web.cern.ch/e98/papers/tup07b.pdf.

[73] G. Ciovati, P. Kneisel, and G. Myneni. "Effect of low temperature baking on niobium cavities." In: *Proceedings of the 11th Workshop on RF Superconductivity* WEO14 (2006).

[74] G. Ciovati et al. "High field Q slope and the baking effect: Review of recent experimental results and new data on Nb heat treatments." In: *Phys. Rev. Accel. Beams* 13.022002 (2010). DOI: 10.1103/PhysRevSTAB.13.022002.

[75] A. Romanenko et al. "Effect of mild baking on superconducting niobium cavities investigated by sequential nanoremoval." In: *Phys. Rev. ST Accel. Beams* 16 (1 Jan. 2013), p. 012001. DOI: 10.1103/PhysRevSTAB.16.012001. URL: https://link.aps.org/doi/10.1103/PhysRevSTAB.16.012001.

[76] G. Eremeev and H. Padamsee. "Change in high field Q-slope by baking and anodizing." In: *Physica C: Superconductivity* 441 (2006). DOI: 10.1016/j.physc.2006.03.046.

[77] A. Romanenko et al. "Proximity breakdown of hydrides in superconducting niobium cavities." In: *Supercond. Sci. Technol.* 26.035003 (2013). DOI: 10.1088/0953-2048/26/3/035003.

[78] I. Malloch et al. "Design and implementation of an automated high-pressure water rinse system for FRIB SRF cavity processing." In: *Proceedings of LINAC2016, JACoW* TUPRC024 (2016). DOI: 10.18429/JACoW-LINAC2016-TUPRC024.

[79] D. Dotson et al. "Use of simple x-ray measurements in the performance analysis of cryogenic RF accelerator cavities." In: *Report No. Jlab-ACC-96-11* (1996).

[80] J. R. Delayen et al. "Determination of the magnetic field dependence of the surface resistance of superconductors from cavity tests." In: *Phys. Rev. Accel. Beams* 21.122001 (2018). DOI: 10.1103/PhysRevAccelBeams.21.122001.

[81] G. Ciovati and J. Halbritter. "Analysis of the medium field Q-slope in superconducting cavities made of bulk niobium." In: *Physica C: Superconductivity* 441 (2006). DOI: 10.1016/j.physc.2006.03.053.

[82] J. Halbritter. "Transport in superconducting niobium films for radio frequency applications." In: *Journal of Applied Physics* 97.083904 (2005). DOI: 10.1063/1.1874292.

[83] G. Ciovati. *High Q at Low, and Medium Field*. https://misportal.jlab.org/ul/publications/downloadFile.cfm?hyperlink=ACF2B2C.pdf. 2005.

[84] G. Ciovati, P. Kneisel, and A. Gurevich. "Measurement of the high-field Q drop in a high-purity large-grain niobium cavity for different oxidation processes." In: *Phys. Rev. ST Accel. Beams* 10 (6 Aug. 2007), p. 062002. DOI: 10.1103/PhysRevSTAB.10.062002. URL: https://link.aps.org/doi/10.1103/PhysRevSTAB.10.062002.

[85] P. Dhakal, G. Ciovati, and G.R. Myneni. "Role of thermal resistance on the performance of superconducting radio frequency cavities." In: *Phys. Rev. Accel. Beams* 20 (3 Mar. 2017), p. 032003. DOI: 10.1103/PhysRevAccelBeams.20.032003. URL: https://link.aps.org/doi/10.1103/PhysRevAccelBeams.20.032003.

[86] P. Yla-Oijala. "Electron multipacting in TESLA cavities and input couplers." In: *Part. Accel.* 63.105 (1999).

[87] J. Vines, Y. Xie, and H. Padamsee. *Systematic trends for the medium field Q slope*. Beijing, China, 2007.

[88] A. Grassellino et al. "Nitrogen and argon doping of niobium for superconducting radio frequency cavities: a pathway to highly efficient accelerating structures." In: *Superconductor Science and Technology* 26.10 (Aug. 2013). DOI: 10.1088/0953-2048/26/10/102001.

[89] M. Martinello et al. "Field-Enhanced Superconductivity in High-Frequency Niobium Accelerating Cavities." In: *Phys. Rev. Lett* 121.224801 (2018). DOI: 10.1103/PhysRevLett.121.224801.

[90] M. Checchin et al. "Frequency dependence of trapped flux sensitivity in SRF cavities." In: *Appl. Phys. Lett.* 112.072601 (Feb. 2018). DOI: 10.1063/1.5016525.

[91] H. Ito et al. "Influence of furnace baking on Q?E behavior of super-conducting accelerating cavities." In: *Prog Theor. Exp. Phys* 071G01 (2021). DOI: doi:10.1093/ptep/ptab056.

[92] P. Sha et al. "Quality Factor Enhancement of 650 MHz Superconducting RF cavity for CEPC." In: *Appl. Sci* (2022). DOI: 10.3390/app12020546.

[93] S. Jin et al. "Development and vertical tests of CEPC 650-MHz Single-Cell Cavities with High Gradient." In: *Materials* 14(24).7654 (). DOI: 10.3390/ma14247654.

[94] P. Dhakal. "Nitrogen doping and infusion in SRF cavities: A review." In: *Physics Open* 5.100034 (Aug. 2020). DOI: 10.1016/j.physo.2020.100034.

[95] A. Romanenko. "Breakthrough Technology for Very High Quality Factors in SRF Cavities." In: *presented at LINAC'14, Geneva, Switzerland* TuIOC02 (Sept. 2014).

[96] A. Romanenko et al. "First direct imaging and profiling of ToF-SIMS studies on cutouts from cavities prepared by state-of-the-art treatments." In: *Proc. SRF 2019 Dresden, Germany* THP014 (Nov. 2019). DOI: 10.18429/JACoW-SRF2019-THP014.

[97] A. Romanenko and A. Grassellino. "Dependence of the microwave surface resistance of superconducting niobium on the magnitude of the RF field." In: *Appl. Phys. Lett.* 102.252603 (2013).

[98] A. Romanenko. *Discussion of future directions of SRF research*. FNAL, Batavia, IL, 2022.

[99] P. J. de Visser et al. "Evidence of a Nonequilibrium Distribution of Quasiparticles in the Microwave Response of a Superconducting Aluminum Resonator." In: *Phys. Rev. Lett.* 112 (4 Jan. 2014), p. 047004. DOI: 10.1103/PhysRevLett.112.047004. URL: https://link.aps.org/doi/10.1103/PhysRevLett.112.047004.

[100] Takayuki Kubo and Alex Gurevich. "Field-dependent nonlinear surface resistance and its optimization by surface nanostructuring in superconductors." In: *Phys. Rev. B* 100 (6 Aug. 2019), p. 064522. DOI: 10.1103/PhysRevB.100.064522. URL: https://link.aps.org/doi/10.1103/PhysRevB.100.064522.

[101] D. Gonnella and M. Liepe. "Flux trapping in nitrogen-doped and 120 degrees C baked cavities." In: *Proc. of the IPAC 2014, Dresden, Germany* (JACoW, 2014) (2014). DOI: 10.18429/JACoW-IPAC2014-WEPRI063.

[102] M. Martinello and. A. Grassellino et al. "Effect of interstitial impurities on the field dependent microwave surface resistance of niobium." In: *Appl. Phys. Lett.* 109.062601 (Aug. 2016). DOI: 10.1063/1.4960801.

[103] D. Gonnella, J. Kaufman, and M. Liepe. "Impact of nitrogen doping of niobium superconducting cavities on the sensitivity of surface resistance to trapped magnetic flux." In: *J. Appl. Phys* 119.073904 (Feb. 2016). DOI: 10.1063/1.4941944.

[104] M. Martinello. "Effect of interstitial impurities on the field dependent microwave surface resistance of niobium." In: *PhD Thesis* 109.062601 (Aug. 2017). DOI: 10.1063/1.4960801.

[105] M. Checchin et al. "Electron mean free path dependence of the vortex surface impedence." In: *Supercond. Sci. Technol.* 30.034003 (Jan. 2017). DOI: 10.1063/1.5016525.

[106] J. Bardeen and M. Stephen. "Theory of motion of vortices in superconductors." In: *Phys. Rev.* 140.A1197 (Nov. 1965). DOI: 10.1103/PhysRev.140.A1197.

[107] M. Checchin and A. Grassellino. "Vortex dynamics and dissipation under high-amplitude microwave drive." In: *Phys. Rev. Applied* 14.044018 (Oct. 2020). DOI: 10.1103/PhysRevApplied.14.044018.

[108] D. Bafia et al. "New insights in the quench mechanisms in nitrogen doped cavities." In: *Proc. of 19th Int. Conf. on RF Superconductivity* TUP062 (Nov. 2019). DOI: 10.18429/JACoW-SRF2019-TUP062.

[109] D. Bafia et al. "Understanding and pushing the limits of nitrogen doping." In: *Proc. 10th Int. Particle Accelerator Conf, JACoW* (2019). DOI: 10.18429/JACoW-IPAC2019-WEPRB114.

[110] M. Martinello et al. "Q-factor optimization for high-beta 650 MHz cavities for PIP-II." In: *J. Appl. Phys.* 130.174501 (Aug. 2021). DOI: 10.1063/5.0068531.

[111] S. Posen et al. "High gradient performance and quench behavior of a verification cryomodule for a high energy continuous wave linear accelerator." In: *Phys. Rev. Accel. Beams* 25.042001 (2022).

[112] A. Romanenko et al. "Dependence of the residual surface resistance of superconducting radio frequency cavities on the cooling dynamics around Tc." In: *J. App. Phys.* 115.184903 (2014). DOI: 10.1063/1.4875655.

[113] V. Chouhan et al. "Study on electropolishing conditions for 650 MHz niobium SRF cavity." In: *Proc. of NAPAC 2022, JACoW Publishing* (Aug. 2022).

[114] A. Grassellino et al. "Unprecedented quality factors at accelerating gradients up to 45 MV per meter in niobium superconducting resonators via low temperature nitrogen infusion." In: *Supercond. Sci. Technol.* 30.094004 (2017). DOI: 10.1088/1361-6668/aa7afe.

[115] S. Posen et al. "Ultralow Surface Resistance via Vacuum Heat Treatment of Superconducting Radio-Frequency Cavities." In: *Phys. Rev. Appl.* 13 (1 Jan. 2020), p. 014024. DOI: 10.1103/PhysRevApplied.13.014024. URL: https://link.aps.org/doi/10.1103/PhysRevApplied.13.014024.

[116] E. M. Lechner et al. "RF surface resistance tuning of superconducting niobium via thermal diffusion of native oxide." In: *Appl. Phys. Lett.* 119.082601 (2021). DOI: 10.1063/5.0059464.

[117] G. Ciovati. "Improved oxygen diffusion model to explain the effect of low-temperature baking on high field losses in niobium superconducting cavities." In: *Appl. Phys. Lett.* 89.022507 (2006).

[118] M. Wenskat et al. "Vacancy dynamics in niobium and its native oxides and their potential implications for quantum computing and superconducting accelerators." In: *Phys. Rev. B* 106 (9 Sept. 2022), p. 094516. DOI: 10.1103/PhysRevB.106.094516. URL: https://link.aps.org/doi/10.1103/PhysRevB.106.094516.

[119] D. Bafia, A. Grassellino, and A. Romanenko. "The role of Oxygen in enabling high gradients and high Q." In: *Proc. of 20th Int. Conf. on RF Superconductivity, JACoW* THPTEV016 (2021). DOI: doi:10.18429/JACoW-SRF2021-THPTEV016.

[120] A. Romanenko et al. "Effect of mild baking on superconducting niobium cavities investigated by sequential nanoremoval." In: *Phys. Rev. ST Accel. Beams* 16 (1 Jan. 2013), p. 012001. DOI: 10.1103/PhysRevSTAB.16.012001. URL: https://link.aps.org/doi/10.1103/PhysRevSTAB.16.012001.

[121] S. Posen et al. "Efficient expulsion of magnetic flux in superconducting radiofrequency cavities for high Q0 applications." In: *J. Appl. Phys.* 15.213903 (Aug. 2016). DOI: 10.1063/1.4953087.

[122] A. Gurevich and G. Ciovati. "Effect of vortex hotspots on the radio-frequency surface resistance of superconductors." In: *Phys. Rev. B* 87 (5 Feb. 2013), p. 054502. DOI: 10.1103/PhysRevB.87.054502. URL: https://link.aps.org/doi/10.1103/PhysRevB.87.054502.

[123] A. Romanenko et al. "Dependence of the residual surface resistance of superconducting radio frequency cavities on the cooling dynamics around Tc." In: *J. Appl. Phys* 115.184903 (May 2014). DOI: 10.1063/1.4875655.

[124] D. Gonnella and M. Liepe. "Cool down and flux trapping studies on SRF cavities." In: *Proc. of LINAC2014, MOPP017* (2014).

[125] A. Grassellino. *Into to the flux expulsion problem for LCLS-2*. FNAL, Batavia, IL., June 2016. URL: https://indico.fnal.gov/event/12459/contributions/14263/attachments/9498/12180/AnnaG-intro-fluxexpulsion.pdf.

[126] S. Aull, O. Kugeler, and J. Knobloch. "Trapped magnetic flux in superconducting niobium samples." In: *Phys. Rev. ST Accel. Beams* 15 (6 June 2012), p. 062001. DOI: 10.1103/PhysRevSTAB.15.062001. URL: https://link.aps.org/doi/10.1103/PhysRevSTAB.15.062001.

[127] F. Lange. "Calculation of the Critical Current Density of Hard Superconductors from the Magnetization of Cylindrical Samples." In: *Journal of Low Temperature Physics* 17.112 (1974).

[128] A. Palczewski. "Analysis of Flux Pinning Variability with Niobium Stock Material for LCLS-II." In: *18th Int. Conf. on RF Superconductivity* MOPB048 (July 2017). URL: https://accelconf.web.cern.ch/srf2017/talks/tuxba06_talk.pdf.

[129] T. Xu et al. "Progress of FRIB SRF production." In: *Proc. of 18th Int. Conf. on RF Superconductivity, JACoW* TUXAA03 (July 2017). DOI: 10.18429/JACoW-SRF2017-TUXAA03.

[130] C. Contreras et al. "Dynamic tuner development for medium β superconducting elliptical cavities." In: *Proc. of 9th Int. Part. Accel. Conf., JACoW* THPAL034 (2018). DOI: 10.18429/JACoW-IPAC2018-THPAL034.